5-2019

# Nanomaterials-Based Electrodes for Lithium-Ion Batteries and Alcohol Fuel Cells

Lakshman K. Ventrapragada
*Clemson University*, lventra@g.clemson.edu

# NANOMATERIALS-BASED ELECTRODES FOR LITHIUM-ION BATTERIES AND ALCOHOL FUEL CELLS

---

A Dissertation
Presented to
the Graduate School of
Clemson University

---

In Partial Fulfillment
of the Requirements for the Degree
Doctor of Philosophy
Chemistry

---

by
Lakshman K. Ventrapragada
May 2019

---

Accepted by:
Dr. Apparao M. Rao, Committee Chair
Dr. Stephen E. Creager
Dr. Ramakrishna Podila
Dr. Shiou-Jyh Hwu

ABSTRACT

This dissertation describes my research on surfactant-free synthesis of nanomaterials with applications for alcohol fuel-cell electrodes, and design and fabrication of nanomaterials-based current collectors that improve the performance of lithium-ion batteries (LIBs) by replacing existing current collectors.

Chapter 1 provides a background on the electroanalytical tools used in this research, and an introduction to fuel cells and LIBs.

Chapter 2 describes a novel synthesis method for fabricating gold-graphene composites by laser ablation of a gold strip in water. A well-known limitation in the fabrication of a metal-graphene composite is the use of surfactants that strongly adsorb on the metal surface and consequently reduce the catalytic activity of the metal catalyst. I developed a laser ablation-based one-pot synthesis to decorate graphene with gold nanoparticles (AuNPs) in water without using any surfactants. This linker-free gold-graphene composite was successfully tested as an electrode for the electrocatalytic oxidation of alcohols.

A novel electrochemical method for depositing a porous gold-polycurcumin (Au-Polycurcumin) nanocomposite on conducting surfaces is presented in chapter 3. Au-Polycurcumin showed an excellent electrocatalytic activity for oxidation of small organic molecules such as ethanol, and methanol.

In chapter 4, I demonstrate that reducing the resistance at the current collector active material interface (CCAMI) is a key factor for enhancing the performance of LIBs. I show that carbon nanotubes (CNTs), either directly grown or spray-coated on Al foils,

are highly effective in reducing the CCAMI resistance of traditional LIB cathode materials ($LiFePO_4$ or LFP, and $LiNi_{0.33}Co_{0.33}Mn_{0.33}O_2$ or NMC). The vertically aligned CNT-coated electrodes exhibited energy densities as high as (1) ~500 W h $kg^{-1}$ at ~170 W $kg^{-1}$ for LFP and (2) ~760 W h $kg^{-1}$ at ~570 W $kg^{-1}$ for NMC, both with a Li metal anode.

In chapter 5, I demonstrate a surfactant-free spray coating process to coat commercial cellulose-based paper with CNTs. The prepared paper-CNTs are capable of replacing the conventional aluminum foil used in LIBs. Paper-CNTs were coated with $LiFePO_4$ as the active material and used as cathodes with Li as the anode, and the assembled LIBs showed a high energy density of 460 Wh $kg^{-1}$ at a power density of 250 W $kg^{-1}$.

# DEDICATION

To my beloved master and guide, Bhagawan Sri Sathya Sai Baba. I consider myself extremely fortunate to be under Sai Baba's tutelage.

# ACKNOWLEDGMENTS

I would like to express my gratitude to my Ph.D. advisors from Clemson Nanomaterials Institute, Prof. Apparao M. Rao and Dr. Ramakrishna Podila for their support and guidance throughout my stint at Clemson University. I would like to sincerely thank them for providing me with an opportunity to work in their lab and providing me with the necessary resources and funds. I would like to acknowledge the support and advice provided by my co-advisor, Prof. Stephen E. Creager from the Department of Chemistry.

I greatly benefitted from the courses taught by Prof. Rao (Energy Storage in Carbon Nanomaterials), Prof. Creager (Surface Analysis, and Electrochemical Science), Prof. Shiou-Jyh Hwu (Solid State Chemistry), and Prof. George Chumanov (Analytical Imaging). These courses greatly helped me in my research and job interviews.

I would like to sincerely thank the following people for their help during my research work, Dr. Ramesh Biswal, Prof. Mark Roberts and his team, Prof. Joseph Thrasher, Prof. Rajendra Bordia, Dr. Olt Geiculescu, and Dr. Sriparna Bhattacharya. I would like to thank the support of my colleagues, Dr. Jingyi Zhu, Dr. Anthony Childress, Dr. Jamie Shetzline, Dr. Iqbal Sharif, Dr. Achyut Jamadagni, Dr. Sai Mallineni, Dr. Yongchang Dong, Bipin Sharma, Prakash Parajuli, Wren Gregory, Herbert Behlow, Fengjiao Liu, Kyle Beard, and Saheed Bukola. I feel privileged for the opportunity to work at Lam Research with Dr. Kari Thorkelsson, and Managing Director of Electrofil business unit, Dr. Stephen Mayer.

I had a great time with Sai family from Sai Baba Center of Anderson who helped me to be a better person. I would like to express my gratitude to my parents, my brother, Aswini and his wife - Anusha, my wife's parents, and her family for their support and love. I would like to acknowledge my wife, Divya Vedullapalli for her help with Matlab code and her patience in supporting my crazy schedule and our son, Sairam. I would like to offer my sincere gratitude to all those who directly and indirectly helped me in the completion of this work.

I would like to acknowledge the financial support by the Department of Chemistry, Prof. Stephen E. Creager, Prof. Apparao M. Rao, and the Department of Physics and Astronomy at Clemson University.

TABLE OF CONTENTS

Page

Table of Contents (Continued)

Page

LIST OF TABLES

LIST OF FIGURES

Figure Page

List of Figures (Continued)

Figure Page

List of Figures (Continued)

Figure Page

List of Figures (Continued)

Figure Page

# CHAPTER ONE

# INTRODUCTION

## 1.1 ELECTROANALYTICAL TECHNIQUES

Electrochemistry deals with the links between chemical reactions and electricity. This includes the study of chemical changes caused by the passage of an electric current across a medium, as well as the production of electric energy by chemical reactions. Electrochemistry also embraces the study of electrolyte solutions and the chemical equilibria that occur in them.

### 1. 1. 1 Cyclic voltammetry

Cyclic voltammetry (CV) is one of the most extensively used electrochemical techniques among the potential sweep techniques. Linear sweep voltammetry (LSV) is the simplest of potential sweep techniques which involves sweeping the electrode potential between from $V_1$ to $V_2$ at a known sweep rate, $\nu$. In the case of CV, the waveform applied initially is same as the LSV, but on reaching the potential limit $V_2$, the sweep is reversed back to potential limit $V_1$ at the same scan rate as the forward sweep instead of terminating the scan.[2] A typical potential-time profile for CV is shown below in Figure 1.1.1.

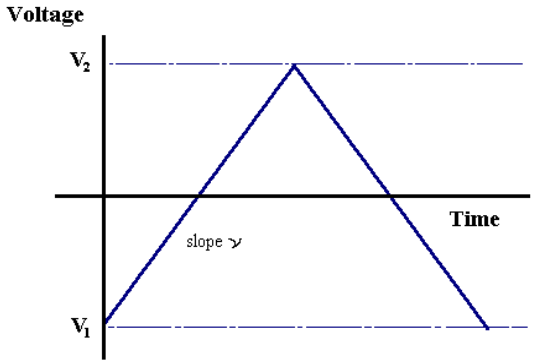


Figure 1.1.1. Potential-time profile for cyclic voltammetry

In essence, CV concerns with the scanning of working electrode potential between the limits of $V_1$ and $V_2$ at a known scan rate, ν, in both the forward and reverse direction and measuring the current response of the electrochemical cell. These cycles of linear ramps can be done any number of times. The resultant current of the system involves a combination of (a) faradaic currents due to electron transfer from oxidation/reduction reactions occurring on the electrode surface, (b) adsorption of ions (non-faradaic currents), and (c) capacitive currents due to the double layer charging at applied potentials. A plot of measured current as a function of the applied potential is known as cyclic voltammogram. Redox reactions undergoing oxidation (anodic scan) or reduction (cathodic scan) at their redox potentials can be studied with the help of CV. Kinetic parameters and the mechanism of different heterogeneous reactions occurring on the electrode surface can also be determined. The conventional experiments of recording voltammograms use a range of sweep rates varying from a few mV $s^{-1}$ to a few hundred V $s^{-1}$ and for several values of $V_1$ and $V_2$. Usually, there may be several peaks from CV

and by observing the characteristics of these peaks over the potential range and as a function of scan rates, it is possible to examine the processes represented by the peaks. In some cases, by noting the difference between the first and subsequent cycles resulting in the cyclic voltammograms, detailed mechanistic information about the electrochemical reactions can be derived. Normally the shape of the cyclic voltammogram depends on the type of redox reaction.[3]

A single electron reversible redox reaction (Eq. 1.1.1a) produces a typical voltammogram represented in Figure 1.1.2. In this case, the rate of charge transfer is always greater than the rate of mass transfer at all potentials and the redox reaction is under diffusion control. The ratio of concentrations of oxidant (O), $C_O$ and reductant species (R), $C_R$ of a reversible reaction are given by the Nernst equation (Eq. 1.1.1b) and a concentration gradient exists within the region near the electrode surface known as the Nernst diffusion layer, where the concentration gradient of the electroactive species is linear. Also, the Nernstian equilibrium is always maintained at the electrode surface and at all the potentials.

$$O + e^- \rightleftharpoons R \qquad \text{Eq. 1.1.1a}$$

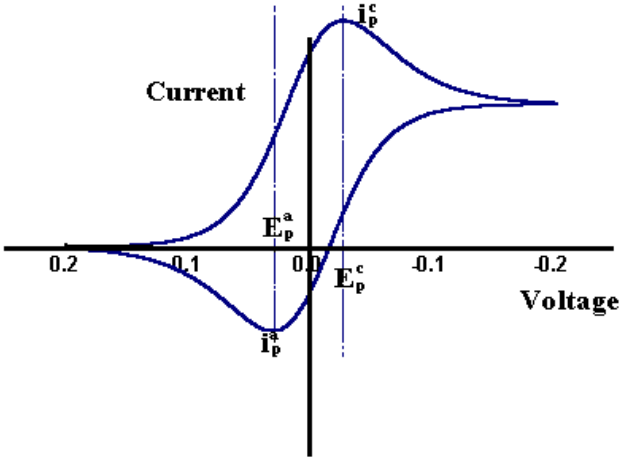


Figure 1.1.2. Cyclic voltammogram for a single electron reversible process.

$$E = E° + 2.303\ (RT/nF)\ \log\ [C_O/C_R] \qquad \text{Eq. 1.1.1b}$$

F is Faraday's constant

n is the number of electrons

$C_O$ and $C_R$ are the concentrations for the oxidized and reduced species respectively

E is the applied potential

E° is the standard reduction potential for the redox couple

R is the gas constant

T is the temperature.

The shape of voltammogram for a one-electron reversible redox reaction as shown in Figure 1.1.2 can be understood in the following way. When the potential of the electrode is made more negative (cathodic scan), the surface $C_O$ decreases progressively, thereby the concentration gradient is increased which results in an increase in the current. On reaching the electrode potential corresponding to the reduction potential of species O, the surface $C_O$ decreases from its bulk value in order to satisfy the Nernst equation and the concentration gradient is set up. As a result, a current proportional to the concentration gradient at the electrode surface flows. Due to the diffusion of ions, the concentration gradient does not remain constant and it starts to reduce. At the same time, the electrode potential is also continuously increasing leading to a further decrease of surface $C_O$ until it effectively reaches zero. Once the $C_O$ reaches zero, the gradient decreases due to the accumulation of reduced species R, in the vicinity of the electrode surface (relaxation effect) and hence the current flow also decreases. Overall, this behavior gives rise to a peak-shaped voltammogram as shown in Figure 1.1.2. Using a similar reasoning for the reverse sweep, it can be shown that the current during the reverse sweep also exhibits a peak-shaped response due to the oxidation of species, R. On increasing the sweep rate, the concentration gradient as well as the current increases due to the shorter timescale of the experiment leading to less relaxation effect.

It can be seen from Figure 1.1.2 that the cyclic voltammogram for a reversible process shows a minimum charge associated with the anodic process of oxidation compared to that of the cathodic reduction process. Throughout the experiment, there is a

concentration difference driving R away from the electrode surface resulting in diffusion of most of the product R to the bulk solution and therefore cannot be reoxidized on the time scale of the experiment. The peak current density $I_p$ of the cyclic voltammogram is related to various parameters by the following relationship (Eq. 1.1.1c).

$$I_p = -0.4463\ nF\ [nF/RT]^{1/2}\ C_O^{\infty}\ D^{1/2}\ \nu^{1/2} \qquad \text{Eq. 1.1.1c}$$

where,

$I_p$ peak current density in A $cm^{-2}$

n number of electrons involved in the redox reaction

F Faraday constant

R gas constant

T absolute temperature

$C_O^{\infty}$ Bulk concentration of reactant O in mol $cm^{-3}$

D diffusion coefficient in $cm^2\ s^{-1}$

$\nu$ sweep rate in V $s^{-1}$

This equation is known as the Randles-Sevcik equation and at a temperature of 25 °C, this equation reduces to the following (Eq. 1.1.1d):

$$I_p = -(2.69 \times 10^5)\ n^{3/2}\ C_O^{\infty}\ D^{1/2}\ \nu^{1/2} \qquad \text{Eq. 1.1.1d}$$

From the above equation (Eq. 1.1.1d), it can be noted that the peak current density of the reversible reaction is directly proportional to the concentration of the electroactive species, square root of the diffusion coefficient and also to the square root of the sweep

rate. The sign of the current is negative because it is the current representing cathodic reaction (by the convention). A test of reversibility of the electrochemical system is to check whether a plot of $I_p$ as a function of $\nu^{1/2}$ is both linear and passes through the origin or alternatively ($I_p$ / $\nu^{1/2}$) is constant. For a slow scan rate experiment, the diffusion layer has enough time to grow further into electrolyte resulting in a lower flux rate. Since current is directly proportional to flux, a lower flux rate results in a lower current in slow scan rate. Also, the ratio of faradaic current to the background charging currents decreases with the increase in scan rate, placing an upper limit on usable scan rate. If $I_p$ is proportional to $\nu^{1/2}$, then further diagnostic tests that are given below can be applied to verify the reversible nature of the given electrochemical system.[4]

1. $\Delta E_p = | E_p^A - E_p^C | = 59/n$ mV;
2. $| I_p^A / I_p^C | = 1$
3. $E_p$ is independent of ν

The potential difference between the anodic and the cathodic peak potentials should be 59 mV for a one-electron transfer reaction. Absolute anodic and cathodic peak current values the same and with increase in scan rate, there shouldn't be any change in the peak potential values as shown in Figure 1.1.3.[5,6] If these criterion are satisfied by a cyclic voltammogram, then the reaction can be considered as a reversible reaction.

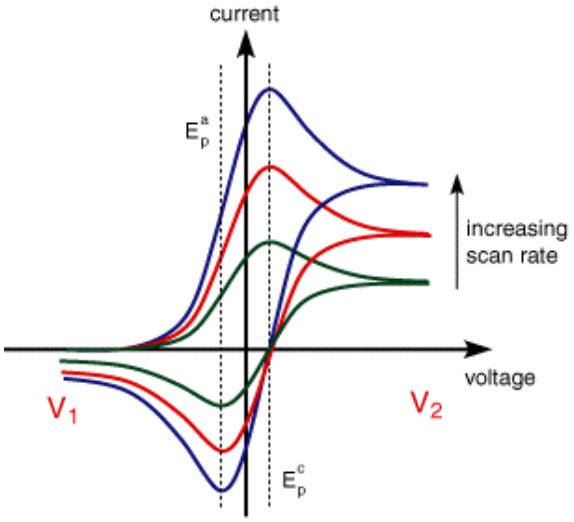


Figure 1.1.3. Cyclic voltammograms for a single electron reversible process with increase in scan rate.

A system is said to have reversible behavior, if the electron kinetics are fast enough to maintain $C_O$ and $C_R$ required by Nernst equation. If the ratio of electron transfer rate constants to the scan rate is low, then it cannot maintain concentrations required by Nernst equation and the system is said to be in quasi-reversible.

CV has been extensively used in this work to study the electron transfer reactions and to measure the surface area of the electrodes.[7]

1.1.2 Chronopotentiometry

Chronopotentiometry (CP) is a constant current experiment (galvanostatic) where the current flowing through the cell is stepped-up from zero to some finite value to perform/study a reaction that has a constant rate.[8] The potential of the working electrode which is characteristic of the redox couple is monitored and plotted as a function of time, known as a chronopotentiogram. There is an initial decrease in potential due to the charging of double layer capacitance and then the reaction takes place at the redox potential of the reactant species. During this process, there is a slow decrease in the potential determined by the Nernst equation, until the surface concentration of reactant reaches zero. The flux of reactants to the surface is then no longer sufficient to maintain the applied current and the electrode potential falls rapidly until a further electrode process occurs.[9]

In my work described in chapter 3, I used CP to deposit Au-Polycurcumin nanocomposite on the cathode. In this deposition technique, for the reaction to take place for longer durations, I circumvent the diffusion limitation by mechanically stirring the solution.

### 1.1.3 Galvanostatic Charge-Discharge

Galvanostatic charge-discharge (GCD) is a technique primarily used to test energy storage devices, like electrochemical capacitors, and batteries. Charge-discharge of a battery can be done by constant current or constant voltage. In my work, all of the charge-discharge cycles were done in constant current mode until as set voltage point is reached, hence called galvanostatic charge-discharge. Current values are based on C-rates and can be deduced from the following equation (Eq. 1.1.3).

$$\text{C-rate} = \text{Capacity (mAh)}/\text{Time (h)} \qquad \text{Eq. 1.1.3}$$

Ideally, at a 1C rate, we should be able to charge/discharge the whole capacity of the battery in one hour; at a 2C rate in 30 min. LIBs can be charged/discharged faster at high C-rate, but the performance and the lifetime of the battery declines. Increasing C-rate also increases *iR* drop and thereby negatively impacts capacity and energy density of the battery.[10] GCD curves are voltage vs. capacity plots, in reality, charge is used as capacity in battery terminology (current multiplied by time). Energy can be calculated by integrating the area under GCD curves. Power is energy over time. Capacity can be expressed as gravimetric capacity (mAh/g) or in terms of areal capacity ($mAh/cm^2$). A sample GCD curve is presented in Figure 1.1.4, where the LIB is charged and discharged between 2.0 – 4.2 V at C/3.[1]

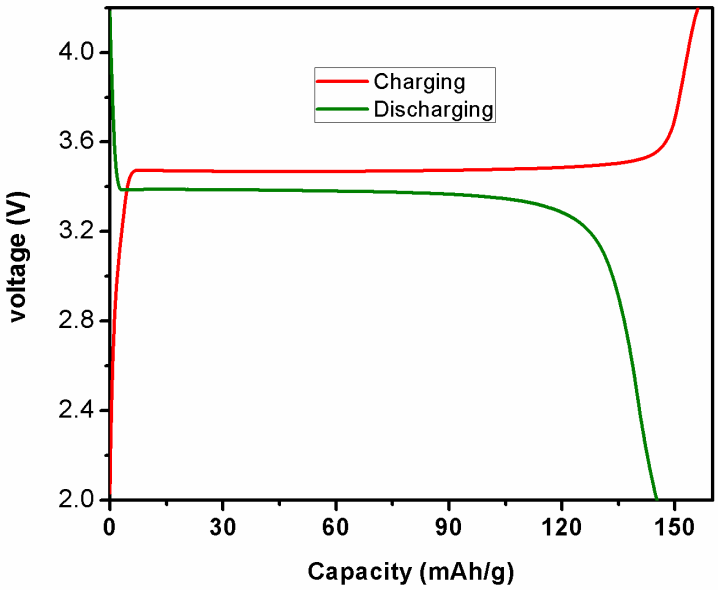


Figure 1.1.4. Galvanostatic charge-discharge curves of an LIB coin-cell with lithium iron phosphate as the cathode and Li metal as the anode. Electrolyte: 1 M $LiPF_6$ in 1:1 ethylene carbonate and diethyl carbonate organic solvent.[1] GCD at a rate of C/3 (50 mAh $g^{-1}$; Mass loading of cathode active material was 3.3 mg $cm^{-2}$)

Cycling of the battery is done by repeating GCD profile multiple times to test the stability and longevity of the assembled battery. Columbic efficiency is calculated based on discharge capacity over charge capacity.

### 1.1.4 Electrochemical Impedance Spectroscopy

Electrochemical Impedance Spectroscopy (EIS) is measured by applying an AC potential (sinusoidal) to an electrochemical cell and measuring the AC current response which depends on the impedance of the cell. An ideal resistor follows Ohm's law (linear current response with voltage) at all cell voltages and currents, resistance values are independent of frequency, AC voltage; and current signals are in phase. In a real electrochemical cell, all elements are not purely ohmic, the system is complex with a non-linear current response to voltage and is frequency dependent. EIS can be used to resolve the complex response of an electrochemical cell and elucidate the behavior of individual components. EIS measurement is done in a wide range of frequencies to study processes that have different time constants. The three most important processes wherein cell voltage drops are due to (a) ohmic loss which happens very quickly, (b) charge transfer loss, and (c) diffusion related loss. The faradaic impedance in an electrochemical cell is the combination of the electrical resistance and capacitance at the interface of electrode and electrolyte. Hence for a redox process, an equivalent circuit consists of a double layer capacitance in parallel with charge transfer resistance. EIS is a more general technique with additional elements such as Warburg impedance, inductance, non-ideal elements like constant phase elements etc.

Usually, a small AC perturbation signal with a fixed DC voltage is applied to the electrochemical cell of interest. To maintain pseudo-linearity the amplitude of AC

perturbation is kept small and the frequency of the perturbation is changed. EIS data are represented either as a Bode plot or a Nyquist plot. Bode plot consists of the magnitude of the impedance (y1 axis) and phase angle (y2 axis) vs. log frequency (x-axis). In a Nyquist plot, the real part of impedance is plotted on the x-axis and the imaginary part is plotted on the y-axis. A theoretical plot for a lithium-ion battery is given in Figure 1.1.5.[11] Key points to note, y-axis is negative and each point on Nyquist plot corresponds to impedance value at a frequency. Generally, high-frequency data is on the left-hand side of the plot and low-frequency data is on the right-hand side. Each semi-circle represents a single time-constant behavior. Section 1 in Figure 1.1.5 corresponds to inductive behavior caused by the metallic elements in the cell and wires. Sum of resistances of the current collector, active material, electrolyte, and separator is given by the series resistance ($R_s$), represented in section 2. Solid electrolyte interface (SEI) formed on the anode is associated with section 3. Section 4 represents double layer capacitance and charge transfer resistance of electrodes. Section 5 is associated with the diffusion process.[11]

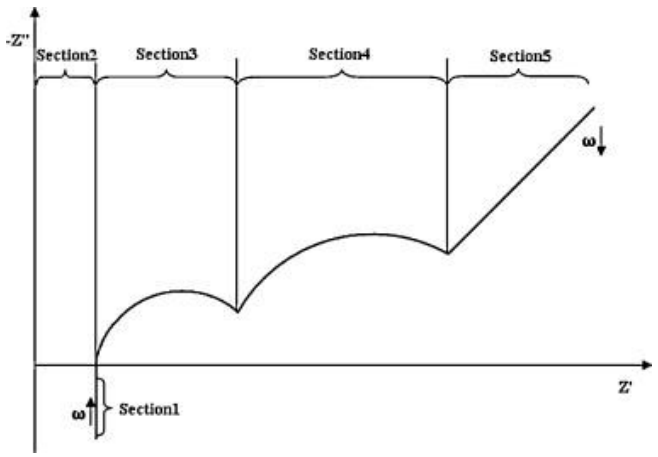

Figure 1.1.5. A schematic of the impedance spectrum as a Nyquist plot for the lithium-ion battery.

My interests in this dissertation (chapters 4 and 5 - LIBs) include the high-frequency (series resistance, $R_s$) and the mid-frequency (charge transfer resistance, $R_{ct}$) regions of the Nyquist plots, which I use to characterize the influence of CNTs on the current collector of the cathode. Normally in an aged cell, a very small semi-circle (additional time constant – section 3) is observed in the high-frequency region, in addition to the big semi-circle.[11–17] In our study, we used lithium metal as the anode and tested fresh coin cells to eliminate the effect of SEI formation on the anode, and hence the smaller semi-circle (section 3) in the high-frequency region is not expected. Consequently, we were able to use the standard Randles equivalent circuit shown in Figure 1.1.6 to fit our EIS data and obtain information for sections 2 and 4.

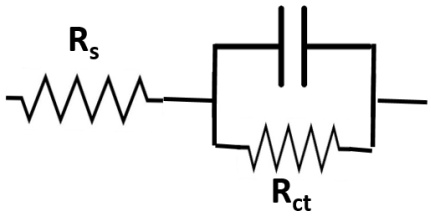


Figure 1.1.6. Randles equivalent circuit.

## 1.2 Fuel Cells

A fuel cell is an electrochemical device that produces energy by converting chemical energy from fuels such as hydrogen, alcohol, etc. into electricity with efficiencies up to 60% which is higher than combustion engines. If hydrogen is used as a fuel, the end products are water, heat along with electricity, and minimal air pollutants. Also, fuel cells with fewer moving parts are quieter than combustion engines. Fuel cells have a wide variety of applications ranging from portable electronics to power stations. Fuel cells continue to produce electricity as long as there is a fuel supply and doesn't have to be charged like batteries.[18]

There a number of types of fuel cells based on the electrolyte such as the proton exchange membrane fuel cells (PEMFC), direct ethanol fuel cells (DEFC), phosphoric acid fuel cells, alkaline fuel cells, molten carbonate fuel cells, solid oxide fuel cells, etc.[19] A typical hydrogen fuel cell is shown in Figure 1.2.1; it consists of an anode (oxidation) and a cathode (reduction) sandwiched between an electrolyte. PEMFCs due to their fast start-up time are favorable for automotive applications. In a typical PEMFCs, hydrogen is fed into the anodic chamber and oxidized by the catalyst present in the anode generating protons and electrons. Electrons flow in the external circuit to the cathode creating an external electrical current and the protons move across the polymer electrolyte membrane to the cathode. Another catalyst at the cathode combines protons with oxygen molecules and electrons to create water. Hydrogen fuel cells are the cleanest source of energy but a

number of challenges such as production, storage, transportation, and safety with hydrogen as a fuel have to be addressed before it can be widely embraced.

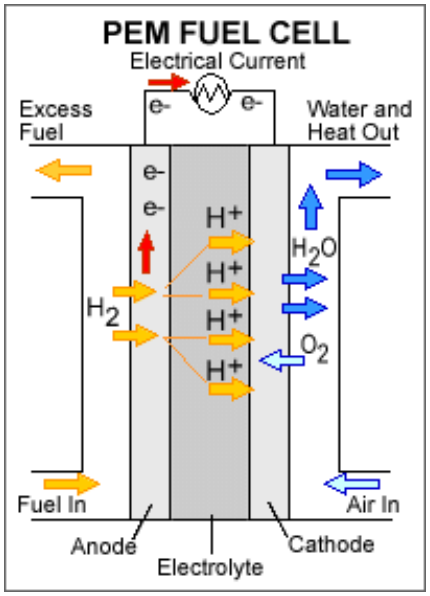


Figure 1.2.1. Schematic of a PEM fuel cell.

On the other hand, alternate fuels such as ethanol and methanol are liquids and easy to handle during transport and storage. Ethanol is also a non-toxic and a high-energy density fuel.[20] Also, ethanol with its higher molecular weight is considered to be better than methanol for fuel cells due to low cross-over through the membrane and thereby not affecting the performance of the cathode.[21] DEFCs can be classified into two types, (a) proton exchange membrane direct ethanol fuel cell (PEM-DEFC) and anion exchange membrane direct ethanol fuel cell (AEM-DEFC). PEM-DEFC operates in acidic medium (Figure 1.2.2) and the catalyst becomes inefficient due to the poisoning of its active sites.[22]

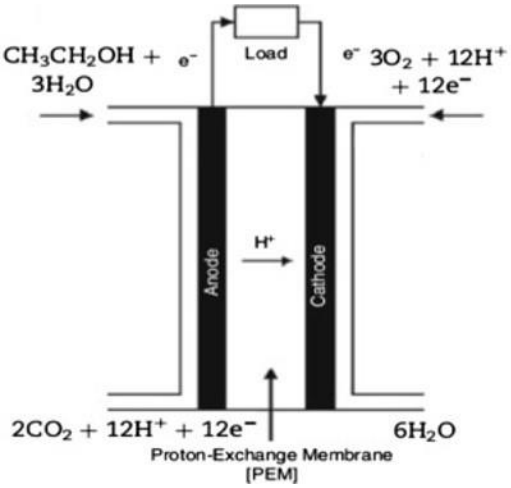


Figure 1.2.2. Schematic of a proton exchange membrane direct ethanol fuel cell.

AEM-DEFC is used in alkaline medium with an –OH conducting membrane as shown in Figure 1.2.3. Quaternary ammonium based membranes are used as the anion exchange membranes and companies such as Tokuyama Corp. commercially supply them.[23] Kinetics of oxygen reduction reaction (ORR) and ethanol oxidation reaction (EOR) shown below are much faster in the alkaline medium compared to the acidic medium.

Anode: $CH_3CH_2OH + 12OH^- \rightarrow 2CO_2 + 9H_2O + 12e^-$ $E^0 = -0.74$ V

Cathode: $3O_2 + 6H_2O + 12e^- \rightarrow 12OH^-$ $E^0 = 0.40$ V

Global equation: $CH_3CH_2OH + 3O_2 \rightarrow 2CO_2 + 3H_2O$ $E^0 = 1.24$ V

Challenges with AEM-DEFC include (a) the lower ionic conductivity (one order magnitude) compared to proton exchange membranes, (b) stability of the membrane, (c)

poor product ($CO_2$ – due to twelve electron transfer reaction) selectivity due to formation of acetic acid (four electron transfer reaction), acetaledhyde (two electron transfer reaction), etc.,[24] and (d) $CO_2$ produced at the anode can react with $OH^-$ present in the electrolyte and form $CO_3^{2-}$, which can precipitate carbonate salts on the membrane and deactivate it with time. This problem can be overcome by using alkaline anode and acid cathode.[25] Hence it is important to find catalysts that can oxidize ethanol in alkaline medium.

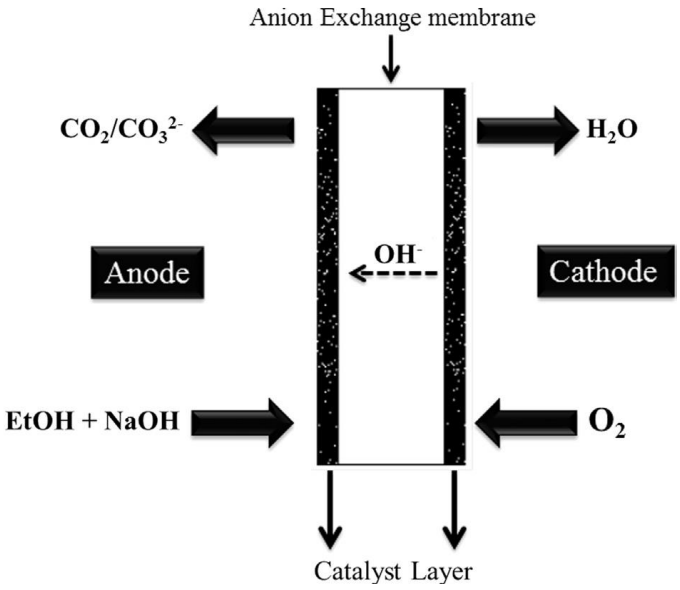


Figure 1.2.3. Schematic of an anion exchange membrane direct ethannol fuel cell.

## 1.3 Lithium-ion Batteries

Rechargeable batteries (e.g., Li-ion) are widely used to power a number of portable electronic devices such as mobile phones and laptops.[26] Although some battery systems are presently being used in electric and hybrid electric vehicles (EV/HEVs), they suffer from poor energy and power densities, which ultimately limit the driving range and increase the cost. To enable cost-effective and long-lasting EVs, DoE estimates that the performance of present battery systems must be improved by at least four times without increasing the cost.[27] Lithium-ion batteries (LIBs) can also support power grids by storing energy from renewable energy sources such as wind, solar, etc.

LIBs are electrochemical devices that store energy in the form of a chemical potential difference.[28] Typical LIBs shown in Figure 1.3.1 have anodic materials such as lithium, graphite or lithium titanate as negative electrodes coated on a copper current collector.[29] Most common cathode materials are lithium transition metal oxides coated on an aluminum current collector. A typical electrolyte is 1:1 by volume mixture of ethylene-carbonate (EC) and dimethyl carbonate (DMC) with 1M $LiPF_6$ salt. Cathodes of LIBs work on the insertion mechanism. When a load is connected to a charged LIB, current is generated due to the potential difference between the electrodes through the following mechanism. During the discharge cycle, a lithium atom leaves an electron at the anode and travels to positive electrode, cathode, through the electrolyte. At cathode, it gains an electron and gets inserted into the electrode. An electron from the anode travels

in the external circuit across the load generating current. During charging a load will be replaced by a power source and the movement of lithium ions and electrons happens in the opposite direction.

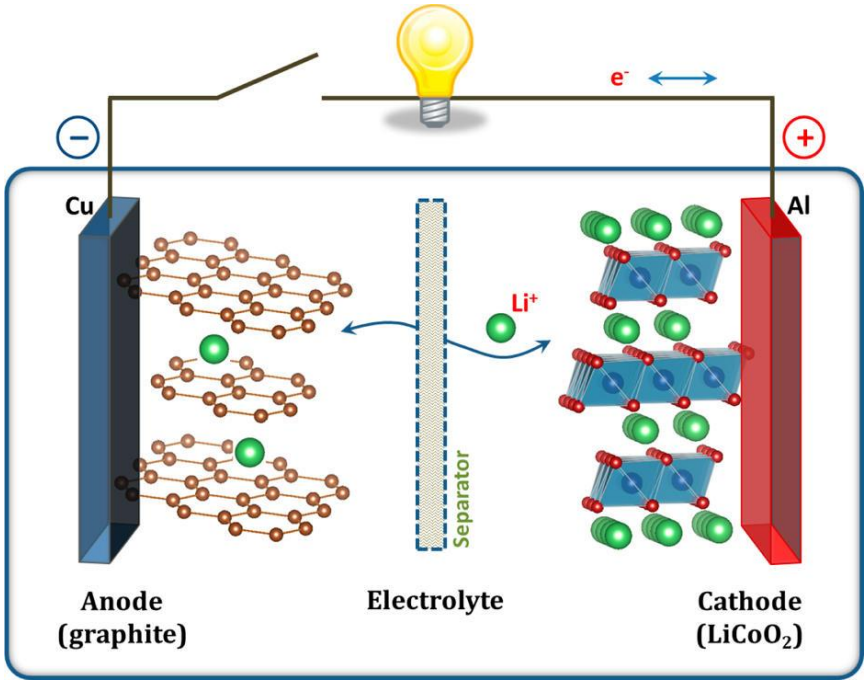


Figure 1.3.1. Schematic of a lithium-ion battery model.

Recently, the replacement of conventional lithium cobalt oxide ($LiCoO_2$, LCO) in commercial Li-ion batteries with olivine-type cathodes, such as lithium iron phosphate ($LiFePO_4$, LFP), has received significant attention in both academia and industry due to the increased safety and cycle life.[30,31] Although the use of the environmentally friendly, low-cost LFP as an alternative to LCO has several drawbacks, such as lower energy density and discharge potential, its high power capabilities and stability have encouraged its use for large-format energy storage.[32,33] Along with power and energy, safety, cost and lifetime of a battery are equally important. Therefore, two major areas of interest in the

use of LFP in commercial batteries are: (a) to increase the capacity of LFP electrodes to a value close to its theoretical limit (to compete with the high energy densities of LCO); combined simultaneously with (b) reducing Li-ion charge transfer and diffusional resistances to achieve low impedance, high-power density. While many strategies have been implemented to address these issues, including supervalent metal cation doping,[34] particle size reduction,[35] and electrode structure control,[36] the introduction of conductive carbon materials has shown the greatest promise for enhancing the performance of LFP batteries.[37,38] Carbon materials have played a major role in boosting the performance of low conductivity cathode materials. The carbon coating process has been a major focus in the commercialization of LFP batteries as the conductive layer creates intimate contact between the current collector and the LFP to increase electronic conductivity while facilitating Li-ion charge transfer and a high charge/discharge rate.

Most of the literature for fabrication of LFP electrodes uses toxic and high boiling chemicals like NMP (N-Methyl-2-pyrrolidone). All of my LIB work is based on developing LFP electrodes with water as the solvent.[39–42] If embraced commercially, this approach will (i) be cost-effective ($1.5-3.0/L NMP vs $0.015/L water), (ii) eliminate the cost of solvent recovery system, and (iii) facilitate an environmentally friendly manufacturing process without the need to modify current battery manufacturing lines. On the other hand, achieving good performance with these cells even at high current density is important. Additional challenges include poor wettability of aqueous

suspensions on aluminum foils, electrode cracking due to residual stress during drying, etc.

In my work, I used vertically aligned carbon nanotubes (VACNTs) directly grown on aluminum foils as current collectors to replace aluminum and carbon coated aluminum foils as current collectors. I also developed a surfactant-free spray coating process to coat commercial cellulose-based paper with CNTs and prepared paper-CNTs current collectors for LIBs. These modified current collectors reduce the interfacial resistance and improve the overall performance of the LIB.

# CHAPTER TWO

## LASER ABLATION MEDIATED SYNTHESIS

This chapter describes my work on the design of a laser ablation mediated synthesis method for gold-graphene composites and their application for electrocatalytic oxidation of methanol and ethanol, which was published in the following article: "Gold decorated graphene by laser ablation for efficient electrocatalytic oxidation of methanol and ethanol" Lakshman Kumar, V. *et al. Electroanalysis* 26**,** 1850–1857 (2014).

### 2.1 Introduction

Of particular interest to the scientific community are materials that have high surface areas than conventional materials. Carbon based materials have been extensively used as electrode materials due to their advantageous properties such as inert electrochemistry and a wide potential window. Some of the most important features of carbon nanomaterials include their surface modification with metal nanoparticles (MNPs),[43] and a wide range of applications in batteries, supercapacitors, fuel cells, sensor technologies, etc.[44] Among carbonaceous materials, CNTs, both single and multiwalled carbon nanotubes have drawn significant interest from scientists in the field of fuel cells for metal nanoparticle decoration.[45,46] There are many areas in current academic and industrial research that study the use of high surface area materials due to their a significant impact in technology, e.g., micro-porous materials for energy storage and separation technologies, and high capacity low volume gas storage of $H_2$ and $CH_4$ for fuel

cell applications. In this context, the high surface area (> 2000 $m^2$ $g^{-1}$) of graphene makes it attractive as a carbonaceous support for MNPs.[47] Recent advances in graphene research received special attention from researchers due to its similarity in physical properties with CNTs, that are considered as rolled sheets of graphene.[48] Unlike CNTs, graphene is devoid of metallic impurities.[47] Hence graphene with a large surface area and enhanced conductivity can be an alternative to CNT as a carbonaceous support for impregnation of metal nanoparticles, resulting in novel composites for future energy and nanotechnological applications[44,46,47,49] Many scientists have used different derivatives of graphene such as graphene oxide and reduced graphene oxide that have well established synthetic routes. But unfortunately they are not a good choice as substrate materials for depositing metal nanoparticles. To chemically synthesize graphene and to deposit metal nanoparticles on is laborious, and the purity of MNP-decorated graphene is essential for high catalytic activity. In our simple one pot synthesis of laser converted graphene (LCG) we were able to also synthesize and deposit MNPs on graphene. Earlier studies related to in-situ chemical reduction of metal salts for synthesizing MNPs[50] could not always generate pristine surfactant free catalysts, and therefore they continue to suffer from this inherent limitation for practical applications. Here we describe our one-step laser ablation mediated synthesis (LAMS) method for preparing MNPs decorated graphene composites. Specifically, we prepared gold nanoparticles (AuNPs) decorated on laser converted graphene (LCG) by LAMS. In this study, we report the electrochemical behavior of Au-LCG for electrocatalytic oxidation of methanol and ethanol that have an application in direct alcohol fuel cell (DAFC).[51,52] Although platinum (Pt) has been used extensively as

an electrocatalyst, its high cost and CO poisoning constrains its utility for DAFCs.[53] On account of this, Au is viewed as a viable alternative to Pt. For this purpose, we coated a glassy carbon electrode (GCE) with Au-LCG by a simple drop cast method without the requirement of Nafion or other matrix binders.[49,54,55] Cyclic voltammetry was used to evaluate the electrocatalytic oxidation reactions of methanol and ethanol in alkaline medium with the modified GCE. AuNPs play a pivotal role in the electrochemical oxidation reactions,[56,57] as evidenced from their electrochemical response involving cyclic voltammograms, Arrhenius plots and activation energy values.

2.2 Laser Ablation for generation of nanomaterials

2.2.1 Chemicals. Methanol, ethanol, sodium hydroxide, and perchloric acid used in this study were of analytical grade (AR). Millipore water having a resistivity of 18.2 MW cm was used to prepare the aqueous solutions. All other chemicals were purchased from Sigma Aldrich with purity higher than 99%.

2.2.2 Synthesis of Au-LCG. Hydrogen induced simultaneous exfoliation-reduction technique was used to synthesize few layered graphene sheets of f-HEG based on our previously published work.[58] The f-HEG sample was hydrophilic in nature on account of the presence of -COOH and -OH functional groups on its surface. Therefore, 1 mg of f-HEG was ultrasonically dispersed in 25 mL of millipore water to form an aqueous solution of functionalized graphene. A gold foil of dimension (2 cm x 1 cm) was ultrasonically cleaned in 5 mL piranha solution and then placed in a glass beaker

containing 3 mL of aqueous dispersion of f-HEG. Laser assisted synthesis in solution was used to synthesize LCG and Au-LCG in a single step.[59] Nd:YAG laser (Surelite III), a high power nanosecond laser with its fundamental harmonic 1064 nm was used as the irradiation source. A convex lens of 10 cm focal length was used to steer and focus the intense laser pulse onto the gold foil. Throughout the ablation period, the laser pulse energy of 50 mJ and the 10 Hz repetition rate were kept constant. As a result, f-HEG got converted to LCG, and further to Au-LCG; this observation is amply supported by XRD analysis discussed in Section 2.3.1.

2.2.2 General Characterization. The surface morphology of the Au-LCG was evaluated using a transmission electron microscope – TECNAI F 20 (S-TWIN) operated at 200 kV. The Au-LCG suspension was drop-casted on carbon coated Cu grids (SPI supplies, 200 mesh), and dark field imaging and select area electron diffraction (SAED) measurements were also performed. Field emission scanning electron microscope (FESEM, Zeiss) was used to obtain FESEM images and energy dispersive x-ray analysis (EDX) for elemental analysis. A Dilor XY triple grating monochromator equipped with a microscope (100x objective) was used to collect room temperature Raman data of the samples used in this chapter. The 514.5 nm excitation wavelength of an $Ar^+$ ion laser at low power (<3 mW) was used to excite the samples. Furthermore, we performed zeta potential studies of Au and Au-LCG using a Malvern Zetasizer instrument. X-ray diffraction (XRD) measurements were done using PANalytical XPERT PRO MPD X-ray diffractometer with nickel filtered Cu Kα radiation as the x-ray source, at a voltage of 45

kV, current of 30 mA and a scan rate of 2°/minute. UV-Visible absorption spectra were recorded on Shimadzu 2450 PC UV-Visible spectrophotometer.

2.2.3 Measurement of Electrochemical Properties. Cyclic voltammetry (CV) was carried out using an IVIUM Compactstat electrochemical workstation. A conventional three-electrode electrochemical cell was used for electrocatalytic oxidation studies. A platinum wire of large surface area was used as the counter electrode and a saturated Ag/AgCl electrode was maintained as the reference electrode. The electrolyte temperature was varied using a temperature controller. A small amount of Au-LCG solution was added and allowed to dry on a glassy carbon electrode (GCE of 3 mm diameter). This modified GCE was used to investigate electrocatalytic oxidation of methanol and ethanol in alkaline medium (0.5 M aq. NaOH) at a scan rate of 100 mV $s^{-1}$. The Au-LCG modified GCE was also tested for about 200 voltammetric cycles of operation to confirm its stability.

## 2.3 Results and discussion

2.3.1 Electron Microscopy, Raman, XRD, UV-Visible Spectroscopy, and Zeta Potential Studies. Figures 2.1a–d show the transmission electron microscope (TEM) images of Au-LCG. Figure 2.1a depicts the TEM image of AuNPs at a scale of 2 nm and the inset figure displays the SAED pattern of Au-LCG. Gauging from the lattice fringes, the d-spacing was calculated to be 0.245 nm which corresponds well to that of AuNPs. Most of the AuNPs were found to be spherical in shape with a dominant size of around

20 nm. In Figure 2.1b and c, at a scale of 50 and 100 nm respectively, the presence of LCG decorated with AuNPs is evident. Furthermore Figure 2.1d, a high contrast dark field TEM image of Au-LCG clearly shows bright diffraction spots corresponding to AuNPs on LCG. Figure 2.1e shows the FESEM image whereas EDX of Au-LCG (Figure 21.f) shows the presence of Au, carbon and oxygen; and the amount of AuNPs was calculated to be 52.65%.

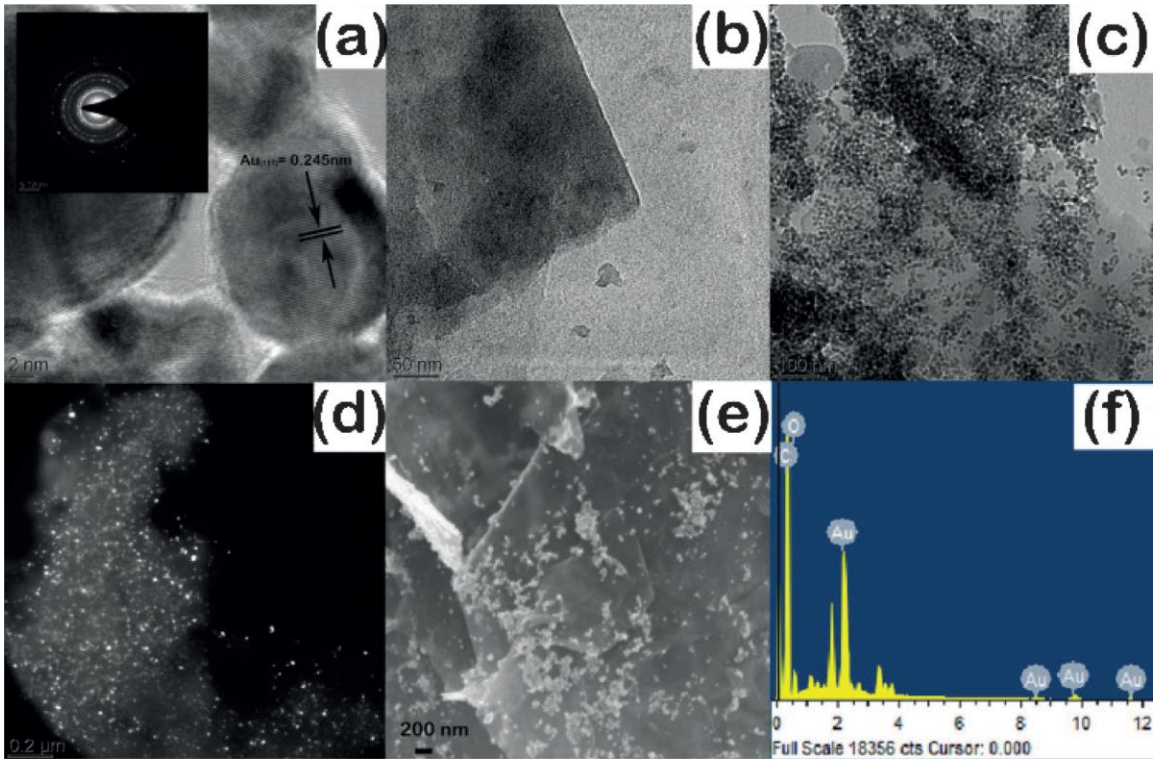


Figure 2.1. TEM images of Au-LCG under different magnifications (a), (b), and (c). Inset: (d) SAED image; dark field image, (e) FESEM image, and (f) EDX of Au-LCG.

The Raman spectra of synthesized f-HEG and Au-LCG are shown in Figures 2.2a and b. A Raman blue shift was observed for both the G (around 1580 $cm^{-1}$) and the 2D (around 2680 $cm^{-1}$) bands of Au-LCG by 4 and 6 $cm^{-1}$ respectively, compared to corresponding band positions in f-HEG; this shift was attributed to the weak charge transfer from LCG to AuNPs in the Au-LCG composite. Deconvolution of the 2D band present at 2680 $cm^{-1}$ indicates the presence of multiple defect activated bands in Au-LCG. Recently, a similar 2D band profile was reported for graphene upon $Ar^{+}$ ion bombardment.[60] Hence, defects in the sample presumably facilitate AuNPs to attach to LCG and lead to an increased catalytic activity of Au-LCG. The XRD data, from Figure 2.2c, clearly indicates the difference between f-HEG, LCG and Au-LCG. A broad peak around 14 to 30° in f-HEG with a d-spacing of 0.37 nm is observed. The absence of the well-known single crystalline peak at 26.7°, which corresponds to the (002) plane in graphite with a d-spacing of 0.34 nm, is due to hydrogen exfoliation. Also oxygenation in f-HEG sheets resulted in a 2θ shift towards the graphite oxide (GO) peak at 10.98° corresponding to the intercalated graphitic sheets with a d spacing of 0.84 nm. During laser ablation, simultaneous loading of AuNPs as well as deoxygenation of f-HEG occurred, leading to the formation of LCG. Neither LCG nor Au-LCG exhibited the 10.98° GO peak or the broad f-HEG peak discussed earlier. The 10 to 30° region in the XRD scans for LCG and Au-LCG was flat without the presence of graphitic peaks (Figure 2.2c), with a lot of similarity to graphene obtained by laser irradiation.[61,62] Unlike f-HEG and LCG, the Au-LCG showed many peaks in the 2θ regions of 30 to 90°. Peaks

at 38.1°, 44.3°, 64.7°, and 77.7° correspond to (111), (200), (220) and (311) planes of AuNPs, respectively.

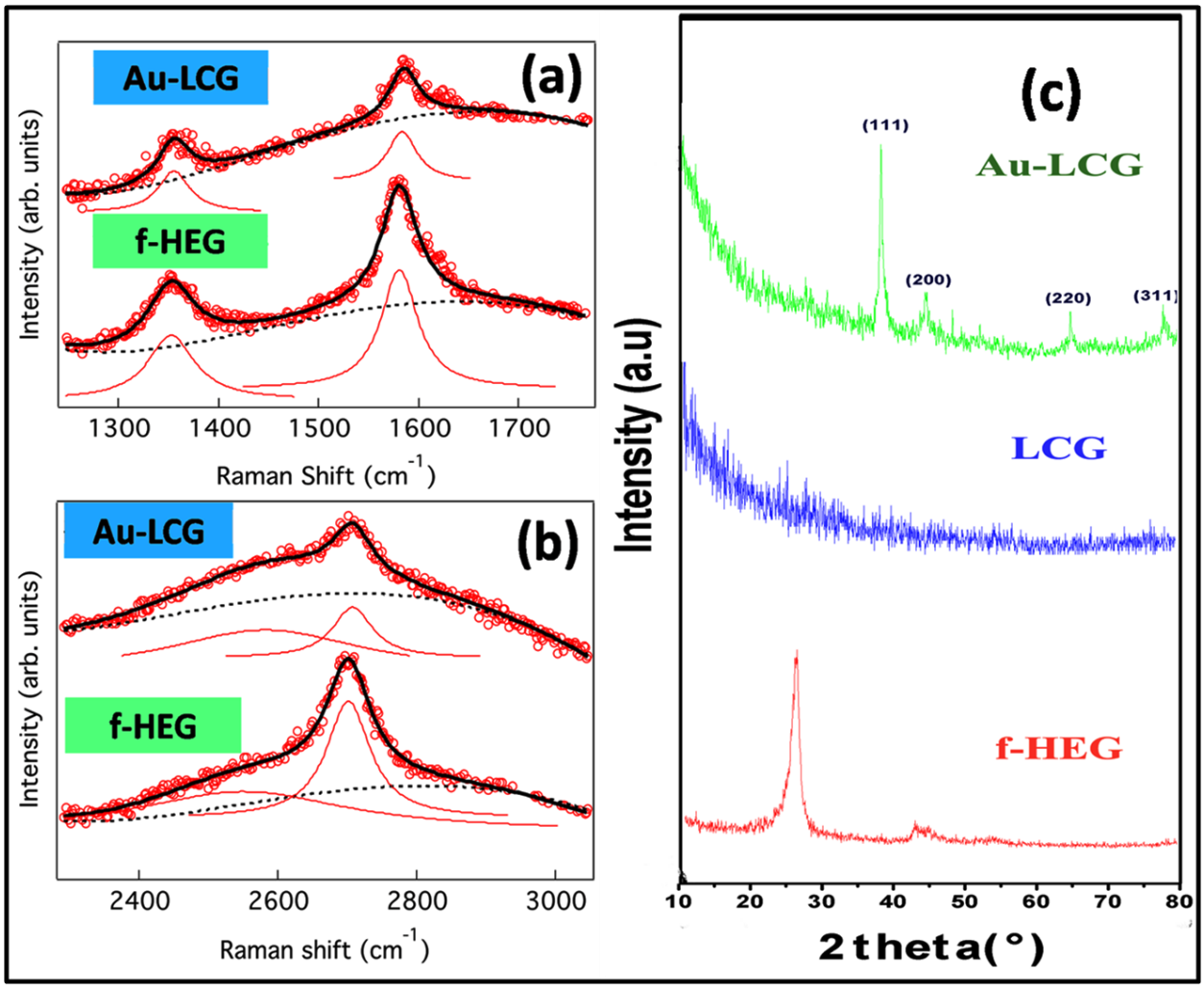


Figure 2.2. Raman spectra of f-HEG (a) and Au-LCG (b). The solid black lines show the fit. The deconvoluted peaks are shown below the obtained spectra along with the background (dotted lines). (c) XRD overlay of f-HEG, LCG and Au-LCG at different 2θ scales.

UV-Vis. absorption spectra of f-HEG and LCG are shown in Figure 2.3a. Laser irradiation of f-HEG caused deoxygenation which was evident since the intensity of the UV peak at 233 nm decreased and the peak at 265 nm became more prominent in case of LCG. In addition, the appearance of a shoulder peak at 355 nm is a clear indication of long range conjugation, possibly due to the formation of double bonds and deoxygenation of f-HEG. The UV-Vis. absorption spectra of Au-LCG at different ablation times are presented in Figure 2.3b. Clearly, the 520 nm plasmonic peak of AuNPs increased in intensity with ablation time (from 20 min to 50 min) as shown in Figure 2.3b, confirming the presence of AuNPs. The zeta potential studies of pristine AuNPs indicated that the particles are negatively charged with a value of 40.0 mV, and this decreased to 48.1 mV for Au-LCG. It was evident that the AuNPs obtained through LAMS at *pH* 7 were negatively charged, consistent with the fact that AuNPs at *pH*>5.8 are known to be negatively charged due to the presence of Au-O– as reported earlier.[63] After the composite was thoroughly characterized and confirmed to be Au-LCG we then evaluated its electrocatalytic oxidation properties.

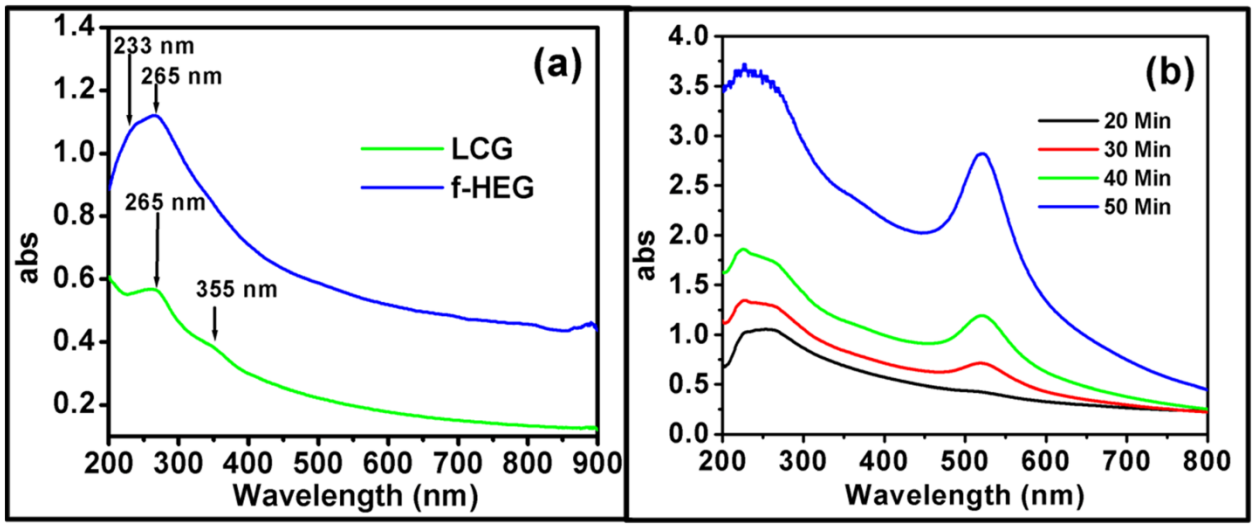


Figure 2.3. UV-Vis spectra overlay of (a) f-HEG and LCG (b) Au-LCG at different ablation times.

2.3.2 Electrocatalytic Activity of Au-LCG. A modified cyclic voltammetric approach (based on adsorption/stripping from solution) was used to determine the absolute surface area of the modified electrodes. The electrochemically active surface area (ECSA) of gold in the Au-LCG on GCE was calculated from the charge measured under the gold oxide reduction peak in 0.1 M $HClO_4$. In Figure 2.4a, a clear peak around 1.2 V corresponds to the oxidation of gold surface; and this gold oxide stripping peak was seen around 0.85 V during the reverse scan and used for ECSA calculations as discussed above. Using the charge associated with desorption of oxide in case of gold oxide as 390 $\mu C\ cm^{-2}$,[64] ECSA for gold in the nanocomposite modified GCE (7.07 $mm^2$) was calculated to be 0.225 $cm^2$ with a roughness factor of 3.2. As stated earlier, we used a simple drop cast method to coat Au-LCG on GCE without employing expensive binders such as Nafion or other polymer matrices. The stability of our coated GCE for methanol

oxidation reaction was excellent as evident from the voltammograms of the 1st and 200th cycles shown in Figure 2.4b. The ~0.1 mA $cm^2$ reduction in the current density for 200 cycles of operation was attributed to poisoning of the electrode surface by accumulated reaction intermediates.[56]

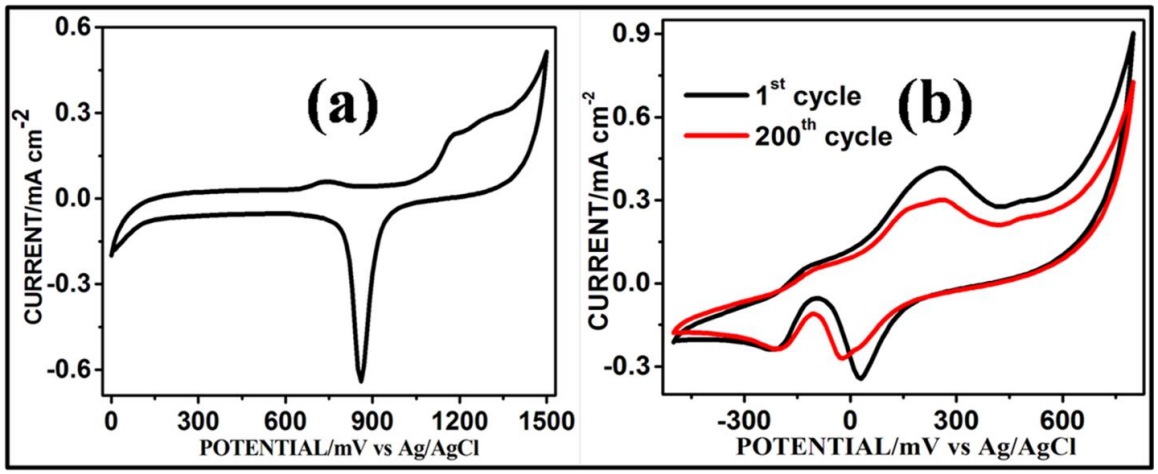


Figure 2.4. Cyclic voltammograms normalized to ECSA of Au-LCG (a) in 0.1 M $HClO_4$, and (b) 0.5 M methanol in 0.5 M NaOH for the 1st and 200th cycles. Scan rate: 100 mV $s^{-1}$.

2.3.3 Electrocatalytic Oxidation of Methanol and Ethanol. Electrocatalytic oxidation of alcohols in alkaline medium was taken as a model system to study the electrocatalytic activity of Au-LCG modified GCE electrodes. Despite extensive use of Pt as an electroactive catalyst for methanol oxidation reactions in acidic medium, Au is considered to be superior in alkaline medium due to its inertness to CO poisoning.[65] With the development of membrane free fuel cells using laminar flow, alkaline fuel cells with

Au as electroactive catalyst provides a low-cost alternative to Pt counterparts.[66] The cyclic voltammograms for the composite in 0.5 M aq. NaOH, with and without methanol addition are represented in Figure 2.5a. The shoulder at around 0.13 V for methanol oxidation reaction during anodic scan is due to the formation of formate ions along with 4 electrons according to the following reaction:[56]

$CH_3OH + 5OH^- \rightarrow HCOO^- + 4H_2O + 4e^-$

A peak at 0.24 V with a current density of 0.27 mA $cm^{-2}$ for 3 M methanol, resulted from the oxidation of formate ion involving the production of 2 electrons in the following manner:[56,63]

$HCOO^- + 3OH^- \rightarrow CO_3^{2-} + 2H_2O + 2e^-$

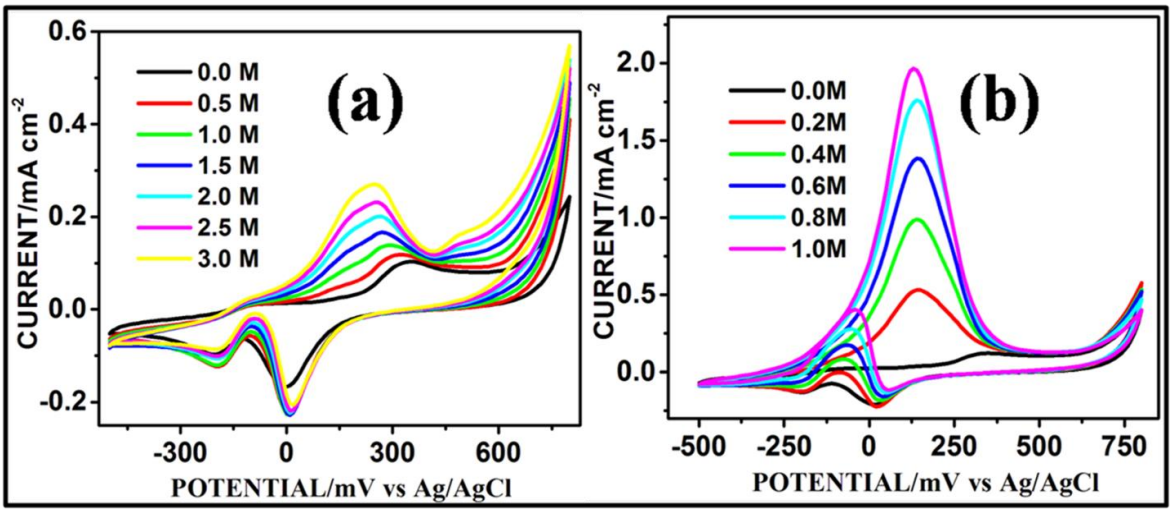


Figure 2.5. Cyclic voltammograms at various (a) methanol concentrations, and (b) ethanol concentrations. Scan rate: 100 mV $s^{-1}$.

Potentials beyond 0.3 V resulted in currents due to gold oxide formation. These oxides were reduced during the cathodic scan at around 0 V, reactivating the gold surface for fresh catalysis. For ethanol electro-oxidation reaction, voltammograms are shown in Figure 2.5b. Ethanol is a greener alternative to methanol on account of its economic viability and availability from biomass for direct ethanol fuel cell (DEFC) applications. In our experiments, we found that the onset potential (potential at current density value corresponding to 10% of peak current density) for ethanol electro-oxidation reaction was -0.35 V, which was 100 mV more negative than that was previously reported.[56] A maximum current density of 1.97 mA $cm^{-2}$ was observed at 0.13 V.

Another anodic reverse oxidation peak that appeared during cathodic scan around 0.1 V, corresponds to the removal of incompletely oxidized carbonaceous species formed during the forward scan. The ratio of the anodic peak currents during forward and reverse scans ($I_f/I_b$) served as a measure of electrodes efficiency in oxidation of ethanol molecules.[67] Higher the ratio, lower is the formation of partially oxidized intermediates and better is the oxidation of ethanol. In our case $I_f/I_b$ was 5, which is relatively high compared to the previously reported value of 4.5,[67,68] highlighting the facile nature of the electrocatalytic oxidation of ethanol by Au-LCG.

2.3.4 Temperature Studies and Activation Energy ($E_a$) Determination. The electrocatalytic oxidation of methanol and ethanol was also performed at elevated

temperatures (288 - 328 K) as shown in Figures 2.6a and b, and the activation energies ($E_a$) were determined from the Arrhenius plots (Figures 2.6c and d). In a conventional Arrhenius plot, $k(T) = Ae^{-Ea/RT}$, $k(T)$ is the rate constant, $A$ is the pre-exponential factor, $T$ is the temperature and $R$ is the gas constant. The activation energy $E_a$ was obtained from the currents *(I)* measured at different temperatures *(T)* using the formula,

$$E_a = R\frac{d(lnI)}{d(1/T)}$$

The Arrhenius plots (log *I* vs. *1000/T*) for methanol and ethanol oxidation reactions at different potentials, near the foot of the cyclic voltammograms, are embodied in Figures 2.6c and d respectively.[54,55] The linear relationship observed from these plots indicated that the fundamental mechanism of electrocatalytic oxidation remained the same at all temperatures in Figures 2.6c and d. The average activation energy values for methanol and ethanol oxidation reactions were calculated as 37.13 and 22.82 KJ $mol^{-1}$, respectively from the data shown in Figures 2.6c and d. These results suggest that ethanol, besides being easily available from biomass, has relatively lower activation energy, and thus serves as an ideal replacement for methanol as fuel. Moreover, the peak current density of 12 mA $cm^{-2}$ for ethanol was higher than that for methanol (1.8 mA $cm^{-2}$) at 50° C.

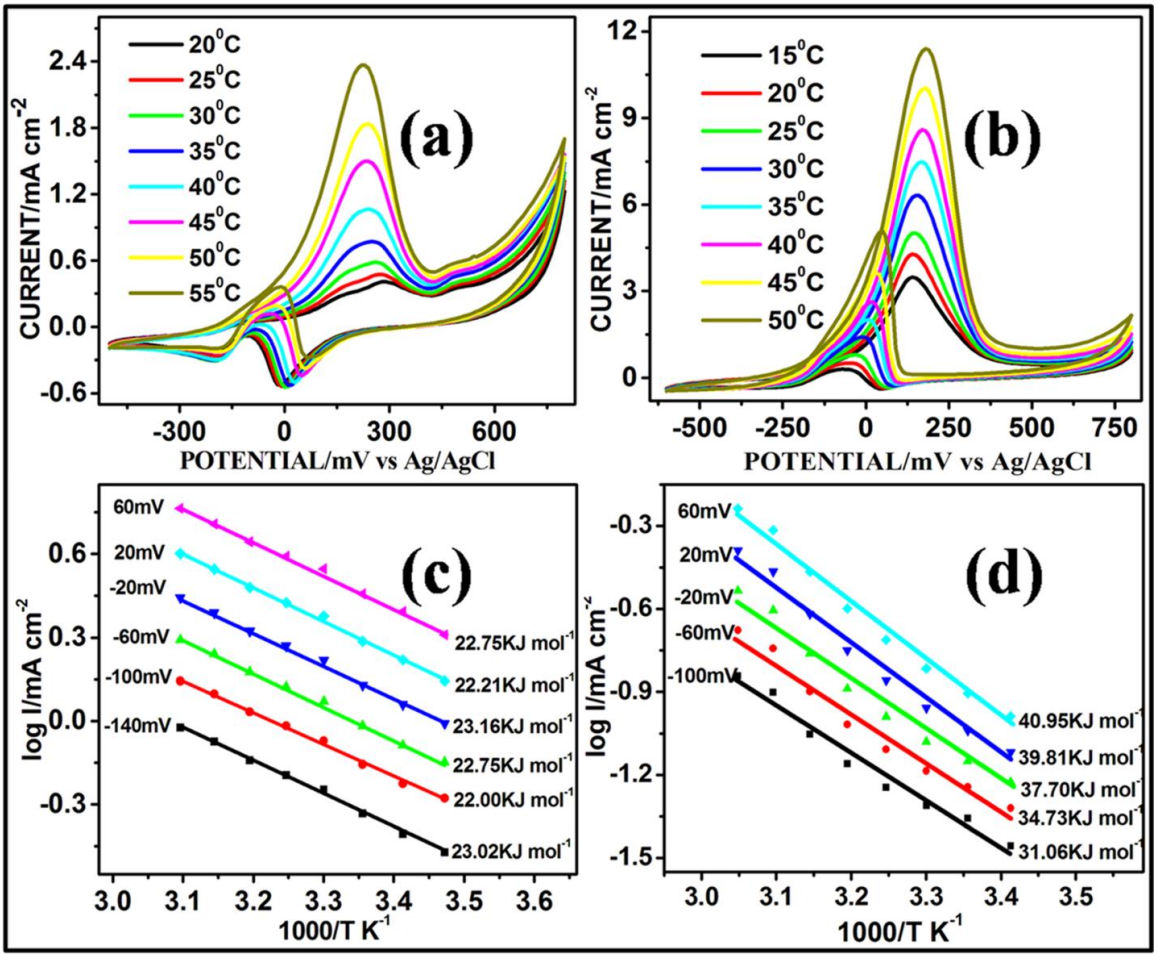


Figure 2.6. Cyclic voltammograms at various temperatures in (a) 3 M methanol and (b) 1.0 M ethanol. Arrhenius plots (log *I* vs *1/T*) for (c) methanol oxidation reaction and (d) ethanol oxidation reaction. The potentials and corresponding activation energy values associated with each potential are labeled in the figure.

## 2.4 Conclusions

We successfully designed a simple and straight forward LAMS based method for synthesizing Au-LCG composite. In our method, AuNPs decorate graphene and give rise to a unique catalyst for alkaline fuel cells. The low onset potential for electrocatalytic

oxidation of ethanol coupled with high current densities proved Au-LCG modified electrode as an active and promising catalyst for direct ethanol fuel cells. In addition the activation energies discussed above prove that the composite is an excellent material for electrocatalytic oxidations reactions. Hence, our one pot synthesis of Au-LCG, free of surfactants or molecular linkers, presents a novel composite with applications that are of environmental and industrial significance.

# CHAPTER THREE

# CONDUCTING POLYMER – METAL NANOCOMPOSITES

## 3.1 Introduction

Gold nanoparticles (AuNPs) due to their unique size and shape dependent properties lend themselves in a number of applications such as optoelectronic devices, catalysts, sensors, etc.[69–71] Incorporation of metal nanoparticles (MNPs) in conducting polymers like polyaniline (PANI), polythiophene (PTP), poly(3,4-ethylenedioxythiophene) (PEDOT), polypyrrole (PPy), etc., can give rise to novel composites that combine the merits of inorganic and organic properties.[72,73] Conducting polymers can be highly porous and offer a number of advantages due to their π- π conjugated backbone.[74] They increase the surface area of MNPs by dispersing them within their porous structure, which enhances the overall electrocatalytic activity of MNPs. Conducting polymers containing MNPs have been widely studied as electrocatalysts for oxidation of small organic molecules such as methanol, ethanol, and formic acid with potential applications in direct alcohol fuel cells, formic acid fuel cells, etc.[75] Alcohols and formic acid are safer as a fuel compared to hydrogen, and provide simpler storage and transportation options. Ethanol due to its bioavailability has well-established supply chain and is less toxic than methanol and formic acid.[76] Hence, it is important to find efficient catalysts that can be used in direct ethanol fuel cells. Platinum has been widely used as an electrocatalyst for fuel cell applications, but its major disadvantage is poisoning with reaction intermediates such as carbon monoxide, CO.[77]

AuNPs are known to exhibit superior electrocatalytic activity for alcohol oxidation at higher pH, wherein even CO plays a supportive role along with hydroxyl ions which act as a source of oxygen during the oxidation process.[78] Some of the important parameters that define a successful electrocatalyst are accessibility of $OH^-$ ions to MNPs, stability of conducting polymer in the electrolyte and adhesion to the electrode surface. Several methods for developing MNPs-polymer composites exists, which include the (i) synthesis of MNPs and addition of polymers,[79] (ii) synthesis of MNPs and chemical polymerization of monomers around them,[80] (iii) monomers acting as a reductant for generation and incorporation of MNPs,[81] (iv) use of chloroauric acid ($HAuCl_4$) as an oxidizing agent for oxidation of monomer units.[82] In redox process (iv), metal ions can oxidize monomers and, the ease of the process depends on the standard reduction potentials of metals, e.g., $Au^{3+}$ (1.498 V), $Cu^{2+}$ (0.34 V), $Ag^+$ (0.8 V), etc.[82] Most of the synthetic designs are multi-step and some of them involve organic solvents such as toluene or surfactants to stabilize MNPs in aqueous solutions. In literature, electrochemical synthesis of MNPs performed by galvanostatic deposition involves dissolution of sacrificial metal anode into metal ions that are further stabilized with alkyl ammonium salts.[83,84] These metal ions then electro-migrate and deposit on the surface of cathode.[56]

Curcumin (Figure 3.6a) is a polyphenolic flavonoid derived from the root of the plant turmeric, *curcuma longa*. Turmeric is extensively used as a spice, food preservative

and coloring agent in many parts of the world. Curcumin derived lot of attention due its medicinal value in treating diseases such as cancer, Alzheimer's disease, etc.[85] Compared to other organic monomers, such as aniline, pyrrole, etc. curcumin is a naturally occurring and safer monomer and hence, researchers have been developing various methods to polymerize curcumin. Previously, Ni-Polycurcumin[86,87] and Cu-Polycurcumin[73,88] syntheses using cyclic voltammetry have been reported; however, to the best of our knowledge, this chapter is the first report for synthesizing Au-Polycurcumin composite. Although previous reports of depositing MNPs-polymer composites on noble metal electrodes using acidic electrolytes exist,[54,55] curcumin is insoluble in acidic electrolytes. Herein we propose a simple one-step electrochemical process for the generation of AuNPs and polymerization of curcumin monomer onto graphite electrode in ethanol-acid mixture. In our work, multiple steps such as the synthesis of MNPs, polymerization of monomer, generation of the composite and coating on the electrode are combined into a single step, and the final electrode can be directly used for studying its electrocatalytic properties. Synthesis of Au-Polyaniline, Au-Polypyrrole, etc.[74,80] have been previously reported with many applications. We expect that Au-Polycurcumin, obtained from a bio-available monomer as described in this chapter, will find several applications.

## 3.2 Electrochemical synthesis of gold-polycurcumin nanocomposite

3.2.1 Chemicals. All chemicals used in the experiments were analytical-grade reagents. Curcumin (Sigma-Aldrich); methanol, ethanol and sodium hydroxide were

purchased from Merck chemicals. Millipore water with a resistivity of 18.2 MΩ cm was used to prepare the aqueous solutions.

3.2.2 Instrumentation. Electrocatalytic oxidation of methanol and ethanol was carried out using a conventional three-electrode electrochemical cell at a scan rate of 100 mV $s^{-1}$. A platinum wire of high surface area was used as the counter electrode along with an Ag/AgCl reference electrode. Gamry and IVIUM Compactstat electrochemical workstations were used to carry out the electrochemical experiments. A Zeiss Sigma FESEM was used to perform FESEM imaging and EDAX measurements of the composite deposited on the electrode surface.

3.2.3 Electrode preparation. Chronopotentiometric deposition in which a gold wire of 0.5 mm thickness and 5mm length was used as a sacrificial anode (working electrode) along with a graphite electrode with exposed end and sides covered (19.63 $mm^2$ area) as the cathode (counter electrode) where the Au-Polycurcumin composite was deposited as shown in the schematic (Figure 3.1). Electrolyte was prepared by dissolving 10 mg of curcumin in 5 mL of ethanol followed by bath sonication for 5 min and subsequent addition of 15 mL of 0.1 N HCl, and the mixture was sonicated for an additional 5 min. The electrolyte was stirred continuously with the help of a magnetic stirrer during the deposition process. Chronopotentiometric deposition was carried out at 0.5 mA for 30 min. The electrochemical deposition was accompanied by bubble

formation at the electrodes due to hydrolysis of water and a vent was provided on the electrochemical cell for the gases to escape.

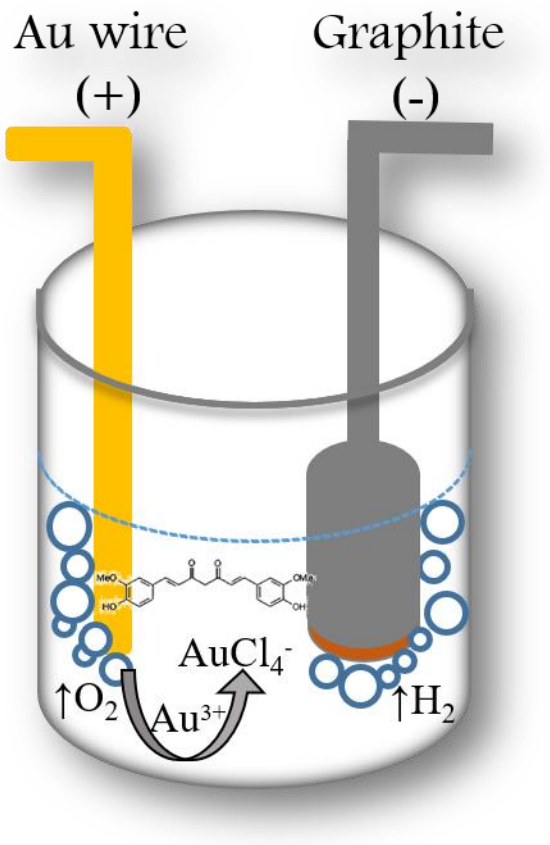


Figure 3.1. Schematic representation for electro-deposition of Au-Polycurcumin composite on graphite cathode.

## 3.3 Results and discussion

3.3.1 Effective catalytic surface area (ECSA). The true surface area of the gold surface on the graphite electrode was determined by a modified cyclic voltammetry approach in 0.1 M $HClO_4$ by measuring the charge associated within the cathodic gold oxide-stripping peak.[86] Figure 3.2 shows the cyclic voltammogram, CV of Au-

Polycurcumin nanocomposite on graphite electrode in 0.1 M $HClO_4$, which exhibits the characteristic behavior of AuNPs in the composite.[56] The voltammogram shows a clear gold oxide-stripping peak during the reverse cycle. The total ECSA of AuNPs coated on the electrode can be estimated from the amount of charge consumed during the reduction of gold oxide monolayer formed during the forward scan. The reported conversion factor for Au is 390 μC $cm^{-2}$ for this process.[56,89–92] From figure 3.2 ECSA of the gold was calculated to be 6.7 X $10^{-3}$ $cm^2$ and hence the roughness factor is less than 1 (0.34) indicating incomplete coverage of the graphite electrode with the composite.

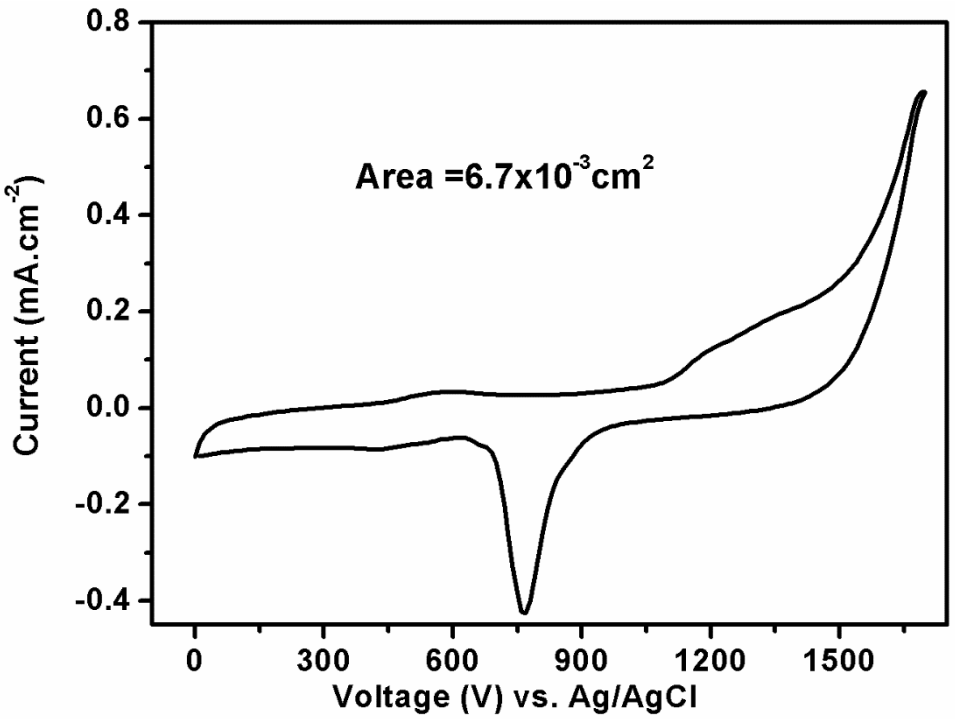


Figure 3.2. CV data for Au-Polycurcumin nanocomposite deposited on graphite electrode in 0.1 M $HClO_4$.

3.3.2 FESEM & EDAX. FESEM images of the electrode surface are presented in Figure 3.3 and the Au-Polycurcumin nanocomposite exhibits cauliflower-like fractal structures.[74] From the FESEM images, the composite appears to be highly porous. On the flower head, the grain sized particles are most likely AuNPs due to their relatively higher contrast, which will subsequently be verified using TEM.

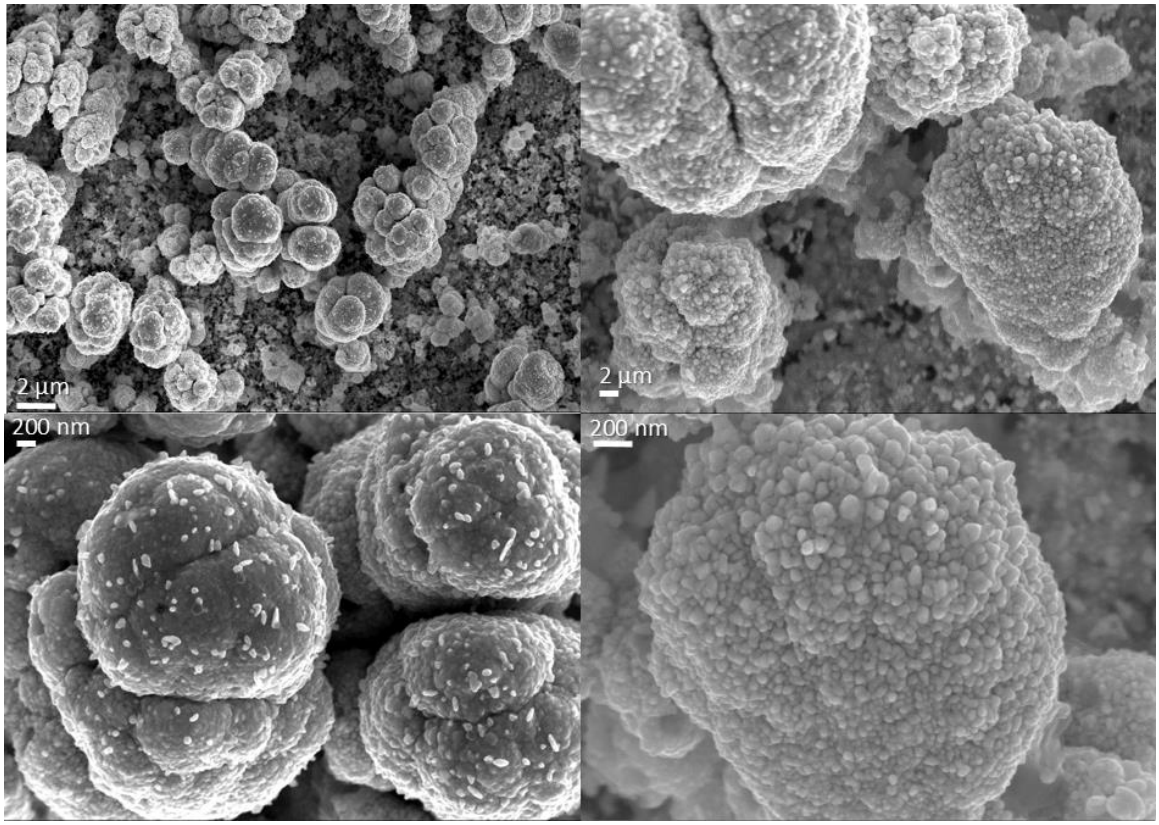


Figure 3.3. FESEM image of Au-Polycurcumin nanocomposite film.

The EDAX spectrum depicted in Figure 3.4b show the predominant presence of Au and carbon with >50 at.% of carbon, and >34 at.% of Au in the Au-Polycurcumin nanocomposite (Figure 3.4a) deposited on the electrode surface. EDAX spectrum (figure

3.4d) of regions where the composite is absent (figure 3.4d) shows insignificant gold (~2 at.%).

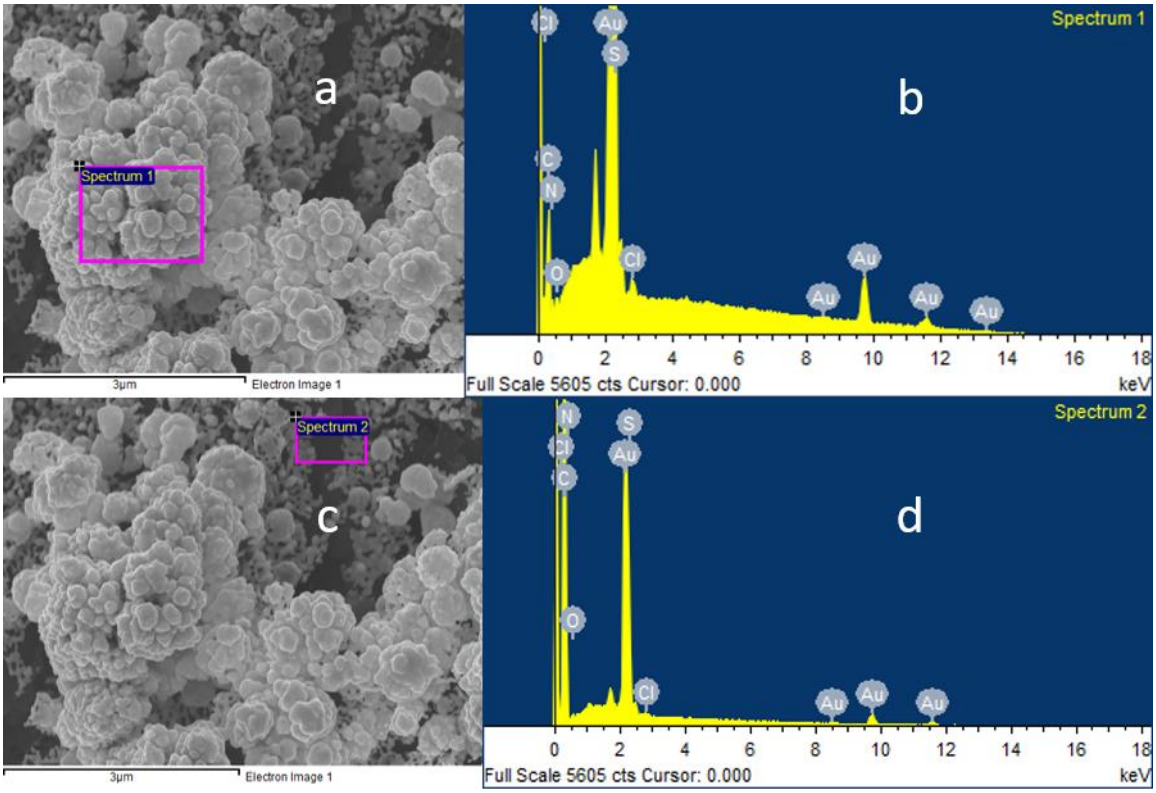


Figure 3.4. SEM image and accompanying EDAX spectrum in the presence (a and b) and absence (c and d) of Au-Polycurcumin nanocomposite.

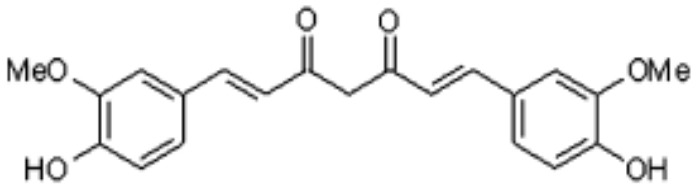


Figure 3.5. The structure of curcumin.

3.3.3 Electrocatalytic oxidation of ethanol. Oxidation of ethanol was carried out in 0.5 M NaOH. Figure 3.6 shows the CVs for oxidation reactions at different concentration of ethanol. The onset potential (potential at current density value corresponding to 10% of peak current density) for the ethanol oxidation was at -0.25 V and the peak potential was around 0.2 V with ~2 mA $cm^{-2}$ comparable to the performance of other Au-polymer composites.[74] In each case, the area of the Au-Polycurcumin composite was calculated from ECSA to normalize the current profiles. To the best of my knowledge, intermediates such as -$CH_3CHO_{ads}$, $CH_3COO^-$, etc. are formed during electro-oxidation of ethanol at the anode.[74]

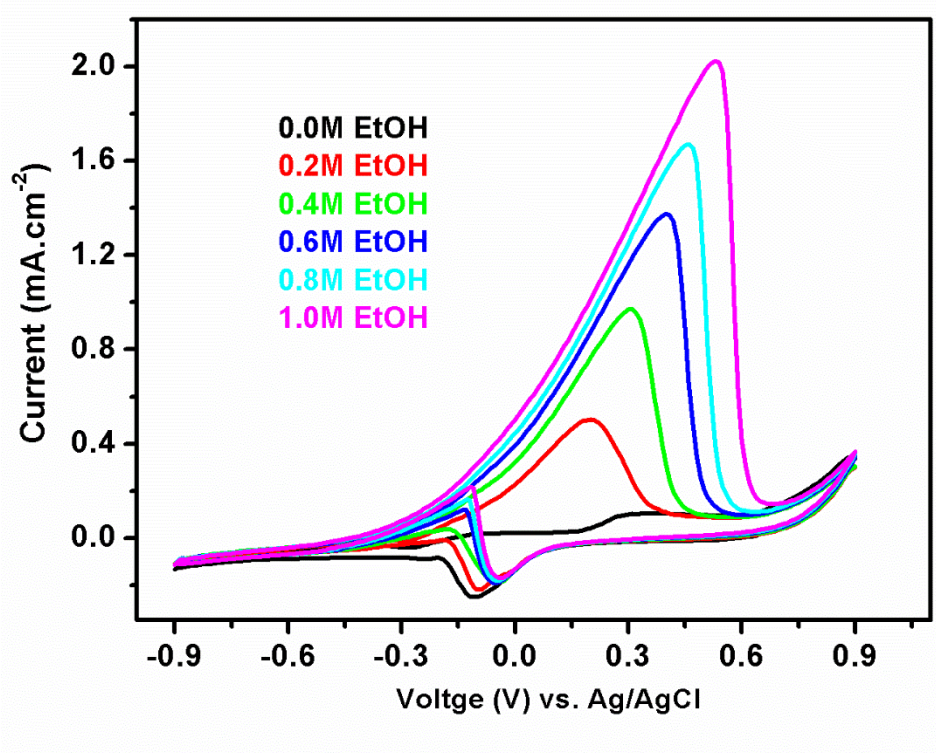

Figure 3.6. CVs for the electrocatalytic oxidation of ethanol with Au-Polycurcumin nanocomposite coated graphite electrode in 0.5 M NaOH.

The stability of the coated electrode for ethanol oxidation reaction was tested by running the reaction for more than 200 cycles in 0.5 M ethanol. Representative CV data for the 1st and 200th cycles are given in Figure 3.7. CVs show that over the duration of 200 cycles, there was an increase in current values indicating further activation of the catalyst during cycling.[93,94]

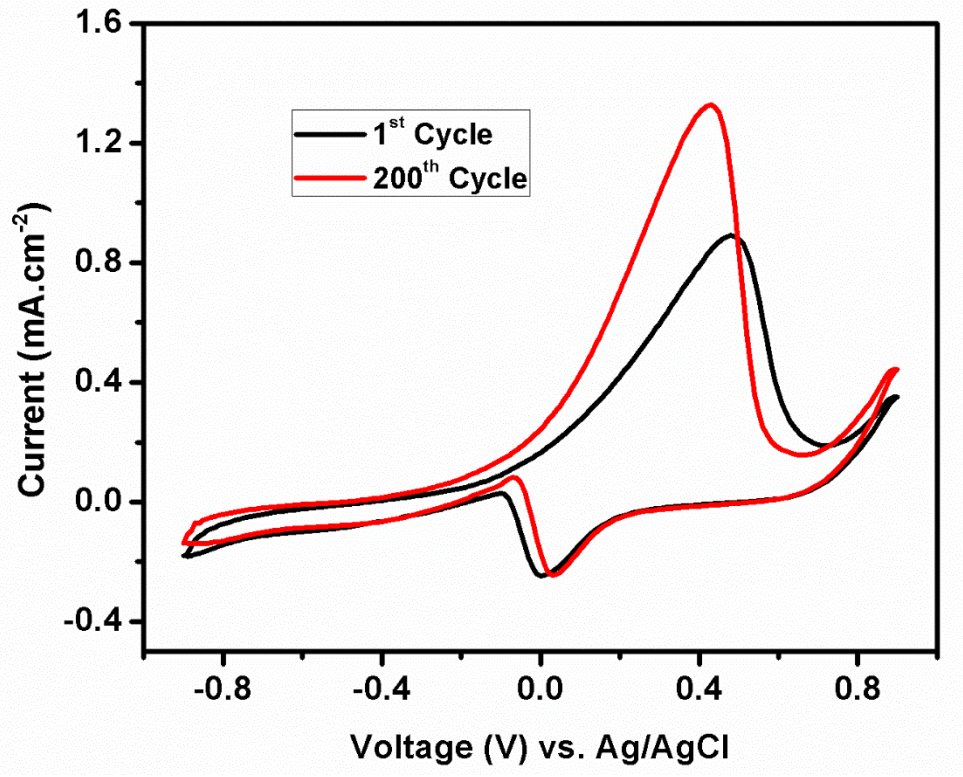


Figure 3.7. CVs for 1st and 200th cycles of electro-oxidation 0.5 M ethanol in 0.5 M NaOH.

3.3.4 Arrhenius plots. Electrocatalytic oxidation of ethanol with the coated electrode was carried out at various temperatures in 0.5 M NaOH and the CVs are presented in Figure 3.8. Current values at various temperatures for a given potential near the foot of a CVs were used to plot the Arrhenius profiles (log $I$ vs. $T^{-1}$) shown in Figure 3.9.[95,96] Activation energy values were calculated from the slope of the plots as ($-E_a/2.303R$). The linear relationship observed in Arrhenius plots indicate that the fundamental mechanism of electro-oxidation remains the same in the temperature range 10 – 55 °C.[74,95] The average activation energy values were calculated to be 38.4 KJ mol$^{-1}$, which are comparable to the performance of the best gold-polymer composite listed in Table 3.1.[74]

| Au-polymer | $E_a$ (KJ mol$^{-1}$) |
|---|---|
| Au-Polycurcumin | 38.4 |
| Au-PANI | 37.0 |
| Au-PPy | 56.7 |
| Au-PTP | 57.0 |
| Au-PEDOT | 56.7 |

Table 3.1. Average activation energy values for electrocatalytic oxidation of ethanol with various Au-polymer composite coated electrodes.

It is clear from the above plots that the rate of electrocatalysis of ethanol increases as the temperature rises and the onset potential becomes more negative. During reverse scan an additional peak is present, which is due to the catalytic activity of activated Au atoms that are not in equilibrium with gold lattice after the reduction of gold oxide in the reverse scan.

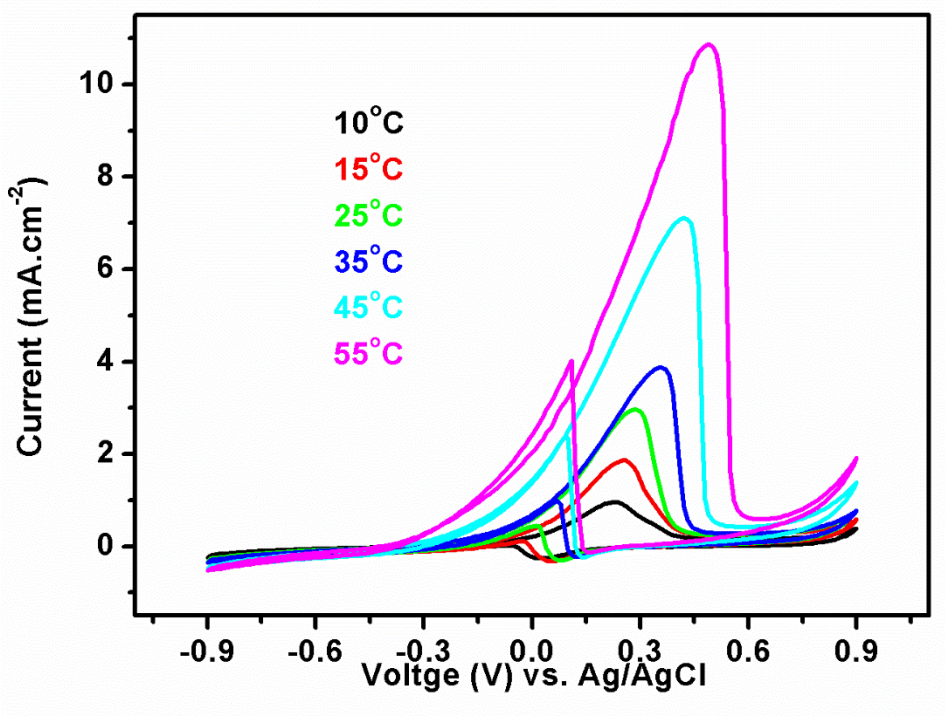


Figure 3.8. CVs for electrocatalytic oxidation of ethanol (1 M) with Au-Polycurcumin coated electrode at various temperatures.

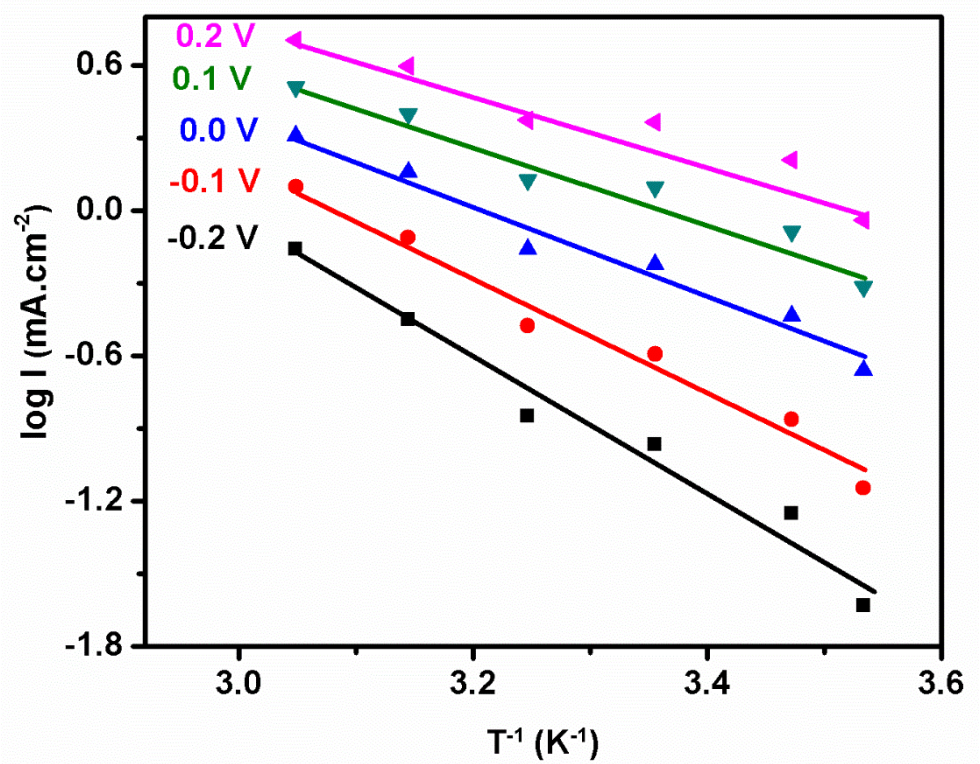


Figure 3.9. Arrhenius plots for ethanol oxidation with Au-Polycurcumin nanocomposite coated electrode at various potentials.

3.3.5 Electrocatalytic oxidation of methanol. The electrocatalytic oxidation of methanol was also carried out in 0.5 M NaOH. Figure 3.10 shows the CVs for oxidation reactions at different concentrations of methanol. The onset potential for methanol oxidation was at -0.2 V vs. Ag/AgCl and the peak potential was around 0.2 V. The plot shows the normalized current values with respect to ECSA.

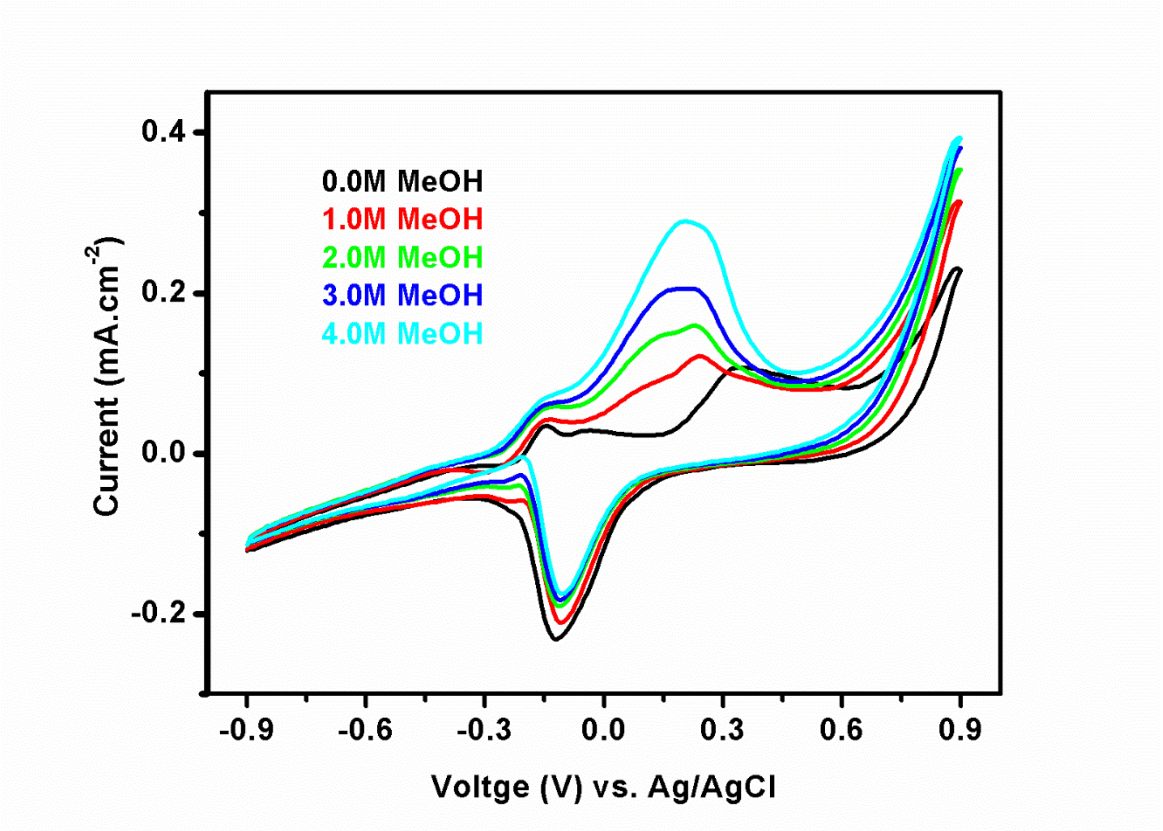


Figure 3.10. CVs for electrocatalytic oxidation of methanol with Au-Polycurcumin nanocomposite coated graphite electrode in 0.5 M NaOH.

3.3.6 Arrhenius plots. Electrocatalytic oxidation of methanol with the coated electrode was carried out at various temperatures in 0.5 M NaOH and the CVs are shown in Figure 3.11. The average activation energy values were calculated to be 27.8 KJ $mol^{-1}$. With increase in temperature, the onset potential becomes more negative indicating lower requirement of activation energy for the reaction due to the higher performance of the catalyst at elevated temperatures.

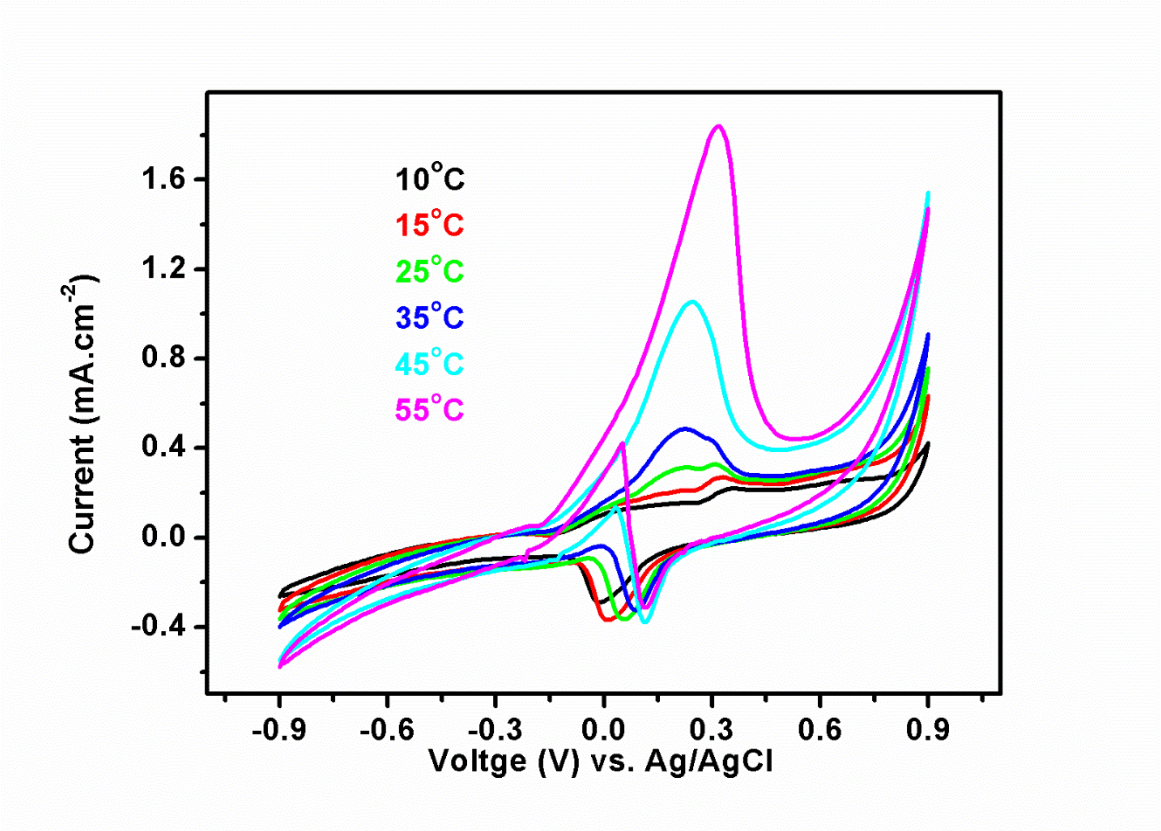


Figure 3.11. CVs for electrocatalytic oxidation of methanol (2 M) with Au-Polycurcumin coated electrode at various temperature.

## 3.4 Conclusions

A one-pot electrochemical synthesis was successfully designed for depositing a novel Au-Polycurcumin composite on graphite electrode from gold wire and a naturally occurring curcumin monomer in ethanol-HCl electrolyte. Electrochemical characterization of the composite showed the presence of AuNPs in the composite. FESEM images showed presence of highly porous composite with cauliflower-like structures. EDAX showed the presence of Au and carbon in these cauliflower-like

structures, which were derived from the polycurcumin polymer. Au-Polycurcumin composite was used as a catalyst for electrocatalytic oxidation of small organic molecules like ethanol and methanol, which has direct application for alkaline fuel cells. Activation energy values for ethanol (~39 $KJ.mol^{-1}$) and methanol (~28 $KJ.mol^{-1}$) oxidation reactions were calculated and the composite showed good cyclability and stability for over 200 cycles.

# CHAPTER FOUR

# CURRENT COLLECTOR ACTIVE MATERIAL INTERFACE

This chapter describes my work on use of vertically aligned carbon nanotubes directly grown on aluminum current collectors to reduce the resistance at the current collector active material interface in lithium-ion batteries, which was published in the following article: "A Versatile Carbon Nanotube-Based Scalable Approach for Improving Interfaces in Li-Ion Battery Electrodes" Ventrapragada, L. K., Zhu, J., Creager, S. E., Rao, A. M. & Podila, R. *ACS Omega* 3**,** (2018).

## 4.1 Introduction

Li-ion batteries (LIBs) are widely used in a variety of devices ranging from portable electronics to power tools and are projected to become the dominant energy storage systems for electric vehicles (EVs)[97] and renewable energy generation technologies (e.g., solar and wind). To this end, the energy and power densities of LIBs must be significantly enhanced with a concomitant improvement in their cycle stability. Prior battery research has focused on identifying new active materials or engineering the micro-structure of known active materials[98] for enhancing LIB's energy and power densities. As a result, many methods to synthesize and process cathode and anode active materials with high capacities are now known.[99] Notwithstanding this progress, LIBs still trail due to fundamental limitations arising from the inherent resistive interfaces within the electrode. Most active materials used in LIB electrodes (both anodes and cathodes)

are poor electrical conductors and must be mixed with conductive additives for coating on a current collector.[100,101] In a typical LIB cathode (/anode) manufacturing line, an Al (/Cu) current collector is coated (at rates 20 m $min^{-1}$) with a slurry containing the active material (e.g., $LiFePO_4$ or LFP and $LiNi_{0.33}Co_{0.33}Mn_{0.33}O_2$ or NMC for the cathode; and graphite and lithium titanate for the anode), ~5 wt. % conductive carbon (e.g., acetylene black, glucose, sucrose), and a binder (e.g., polyvinylidene fluoride or PVDF) in N-Methyl-2-pyrrolidone (NMP), delivered at rates as high as 150 kg $hr^{-1}$.[102] Thus, different types of interfaces between the grains of the active material, conductive additive, and the current collector are inevitably formed which constitute the total internal resistance ($R$) of LIBs (Figure 4.1). Consequently, $R$ results in an undesired voltage drop (or $IR$ drop, where $I$ is the current) and limits the LIB performance at high power. The $IR$ drop increases with the increasing current drawn from the LIB (i.e., higher powers or higher discharge rates) and alters the electrode potential from the equilibrium value leading to a rapid decrease in energy density at higher rates.[103,104]

The present LIB literature is replete with different procedures for improving the interfaces within the active materials by micro-structuring or adding conductive additives such as nanocarbons.[105–113] Notwithstanding this incremental progress, higher areal capacities, faster charge/discharge rates, or mitigating heating losses (arising from $I^2R$) and associated hazards in present LIBs remain challenging. While conventional conductive carbon additives decrease the resistance of interfaces within the cathode/anode active material, they are ineffective in decreasing the current collector

active material interface (CCAMI) resistance - *a key driving factor for increasing energy and power densities* that has largely been ignored in LIBs (Figure 4.1).

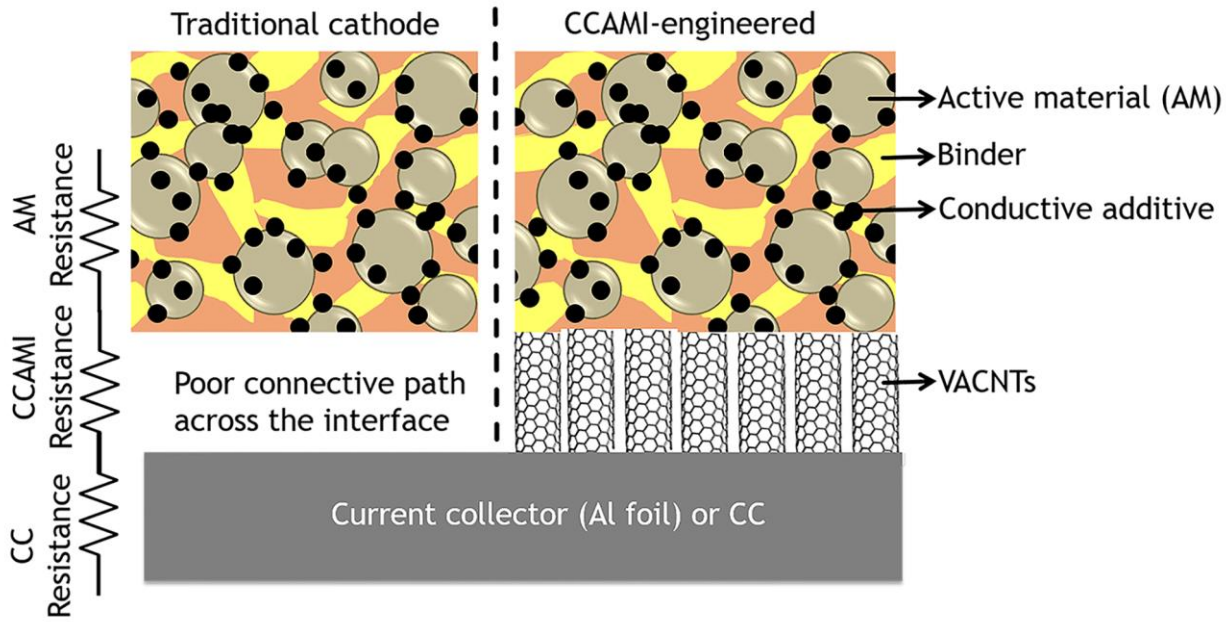


Figure 4.1. A schematic showing various resistances in Li-ion battery cathodes. The overall cathode resistance is the sum of the resistances arising from the: 1) active material, binder, and conductive additive coatings, 2) current collector active material interface (CCAMI), and 3) current collector. As shown on the left, in a traditional cathode, conductive additives decrease the electrical resistance within the active material but do not affect the high CCAMI resistance. On the other hand, as shown on the right, vertically aligned carbon nanotubes (VACNTs) directly grown on Al foil enable better electrical conduction across CCAMI, which dramatically improves the LIB performance.

Previously, super aligned carbon nanotubes (CNTs) grown on Si wafer were drawn into sheets (where the vertical alignment is lost) or coated on cellulose paper to serve as current collectors for fabricating $LiCoO_2$ cathodes.[114,115] While such studies replace the traditional Al foil with CNT-based current collectors, they do not address CCAMI resistance within LIB cathodes. Going beyond existing studies on the use of CNTs in LIBs, we conceptualize and demonstrate a scalable approach for improved CCAMI using vertically aligned CNTs (VACNTs) grown directly on Al foils to enhance LIB electrochemical performance with different cathode active materials in terms of high rate capability, energy and power densities. We hypothesize that a thin layer of CNTs, either grown directly or coated on bare Al foils, decreases CCAMI resistance, improves energy densities, and enables stable performance at significantly high powers. CNTs are electrochemically stable[95,116] and their high electrical conductivity allows for better electron transfer across CCAMI while their high surface-to-volume ratio provides greater ion access. Previously, we demonstrated two roll-to-roll (R2R) processes: (i) a chemical vapor deposition or CVD-based process for growing VACNTs directly on bare kitchen-grade Al foils,[117] and (ii) a spray-coating process for coating industrial-grade Al foils with randomly oriented CNTs.[118] Notably, in both these processes, binders to adhere CNTs to the Al foil are not required. Unlike many methods reported in the literature, our approaches to engineer CCAMI can be readily integrated into LIB manufacturing lines by replacing the traditional current collectors (i.e., Al foils) with CNT-coated Al foils. As delineated below, scalably produced CNT-coated Al foils enhance the performance of different commercially available cathode materials such as LFP and NMC without the

need for further modification by reducing the CCAMI resistance by a factor of three. It should be mentioned that the commercially available bulk LFP (manufacturer specified capacity: 145 mAh $g^{-1}$ at C/10) and NMC (manufacturer specified capacity: 145 mAh $g^{-1}$ at C/5) active materials used in this were not textured or coated with carbon. The engineered CCAMI cathodes resulted in as high as >91 % enhancements (relative to bare Al foil) in energy density at a power density of 1300 W $kg^{-1}$. More importantly, CNT-coated cathodes enable LIB performance at very high discharge rates (~600 mA $g^{-1}$) for up to 500 cycles in case of LFP, where commercial electrodes were observed to fail. Although textured active materials[119–121] show higher intrinsic capacities relative to commercially available counterparts, they are also limited by CCAMI issues resulting from poor interfacial contact with the current collector. In this regard, the CNT-based CCAMI engineering approach can further improve the performance of even textured LFP and NMC powders with higher intrinsic capacities. In addition to improving the LIB performance, we show that CNT-coated Al foils facilitate active materials to be coated using environmentally benign aqueous slurries instead of expensive and toxic NMP slurries used in present LIB manufacturing lines. Lastly, CNT-based CCAMI engineering approach is versatile and compatible with different types of active materials relevant for both LIB cathodes and anodes (e.g., LTO).

## 4.2 Electrode fabrication, cell assembly and testing protocols

4.2.1 Growth of vertically aligned carbon nanotubes (VACNTs) on aluminum (Al) foils (Al/VACNTs). VACNTs were grown on bare Al foils (MTI Corp.) in a two

stage furnace (Thermcraft Inc.) in which the first stage (maintained at 200 °C) served as a preheating zone and the second stage (maintained at 600 °C) served as the reaction zone. A constant flow of ultra-high purity argon gas (500 SCCM) was maintained throughout the synthesis. Acetylene (30 SCCM), and a ferrocene-xylene mixture (injection rate ~1.5 mL $hr^{-1}$) were introduced into the two-stage furnace in which ~2" long Al foils were placed at the center of the reaction zone. About 30 μm tall VACNTs arrays were obtained on the Al foil in a 30-minute-long CVD run. Further details on R2R production using this CVD process can be found in Ref.[117]

4.2.2 Spray coated CNTs on Al foil (Al/CNT-S). Multi-walled CNTs (Cheap Tubes Inc.) were dispersed in isopropanol (4 mg $mL^{-1}$) using a tip sonicator and sprayed coated onto bare Al foils (MTI Corp.) using a paint gun (Iwata 5095 WS400) with 1.3 mm nozzle and 29 psi ambient air pressure. Further details on R2R spray coating process can be found in Ref.[118] The Al foils coated with randomly oriented multi-walled CNTs were used as current collectors for preparing the cathodes which contained LFP, conducting carbon and the binder.

4.2.3 Electrode slurry preparation. The LFP/NMC cathodes were prepared by dispersing $LiFePO_4$ (80 wt. %, MTI Corp.) or $LiNi_{0.33}Mn_{0.33}Co_{0.33}O_2$ (87 wt. %, Electrodes and more), timcal graphite & carbon super P (5 wt. %, MTI Corp.), carboxymethylcellulose (CMC) (1 wt. %, MTI Corp.) and styrene-butadiene rubber (SBR) (7 wt. %, MTI Corp.) in DI water (18 MΩ). CMC was first dissolved completely

in water at 90 ℃, and subsequently, SBR was added to this solution at room temperature. LFP/NMC and carbon super P were dried, mixed and added to the above solution with continuous stirring. The resulting slurry was stirred overnight, and an adjustable doctor blade set at 100 μm was used to coat bare Al foils and commercial carbon-coated (amorphous carbon with modified acrylate adhesive) Al foils procured from MTI Corp. (Al/C), Al/VACNTs and Al/CNT-S foils. Next, the coated Al foils were allowed to dry for 12 h at room temperature, and subsequently, dried at 100 °C for 12 h in precision compact oven. The LFP and NMC mass loadings in these coatings were ~3.3 (porosity of the electrode 0.48) and 2.5 mg $cm^{-2}$, respectively. Thermogravimetric analysis was done using TA instruments TGA Q500 at 20 °C/min. under nitrogen atmosphere.

4.2.4 Coin cell preparation. Cathodes (dia. ~10 mm) were punched, weighed and soaked in an electrolyte of 1M lithium hexafluorophosphate ($LiPF_6$) in ethylene carbonate and dimethyl carbonate (w/w = 1:1, Sigma-Aldrich) before assembling them into 2032 type coin cells with a lithium chip (15.6 dia. x 0.45 mm thick, MTI Corp.) as the counter electrode. These electrodes were separated by a Celgard 2325 separator (Celgard, LLC) that was presoaked in the electrolyte. The coin cells were assembled inside a glove box where oxygen and moisture content was below 0.1 ppm.

4.2.5 Galvanostatic charge-discharge (GCD). Electrochemical characterization was carried out using a Solatron 1470E multi-channel potentiostat. LFP cells were initially conditioned by charging and discharging over a potential range of 2.0 to 4.2 V at

a current density of 35 mA $g^{-1}$. Subsequently, GCD studies were performed at varying current densities (50-600 mA $g^{-1}$) to compare their electrochemical performance. NMC electrodes were tested from 2.5 to 4.3 V at 30 and 150 mA $g^{-1}$. At the material level, gravimetric energy and power densities were calculated based on the weights of the active materials (LFP or NMC). The energy and power density values at the battery level were estimated as 33% of the values obtained at the material level, following Refs.[119,121]

4.2.6 Electrochemical Impedance Spectroscopy (EIS). After conditioning, EIS was conducted on the cells from 1 MHz to 0.1 Hz, at 0 V vs. OCV with an AC amplitude of 20 mV.

## 4.3 Results and discussion

Figure 4.2 shows the cross-sectional morphology of Al/VACNTs (panel a) along with those for LFP coated Al/VACNTs, Al/C, and bare Al electrodes (panels (b-d)) as deduced from scanning electron microscopy (SEM, Hitachi S4800). It is evident from Figure 4.2a that the Al foil is uniformly coated with ~30 μm tall VACNTs. Thermo gravimetric analysis confirmed an equal amount of conductive carbon additives (~4-5 wt. %) in all electrodes[120] (Figure 4.3).

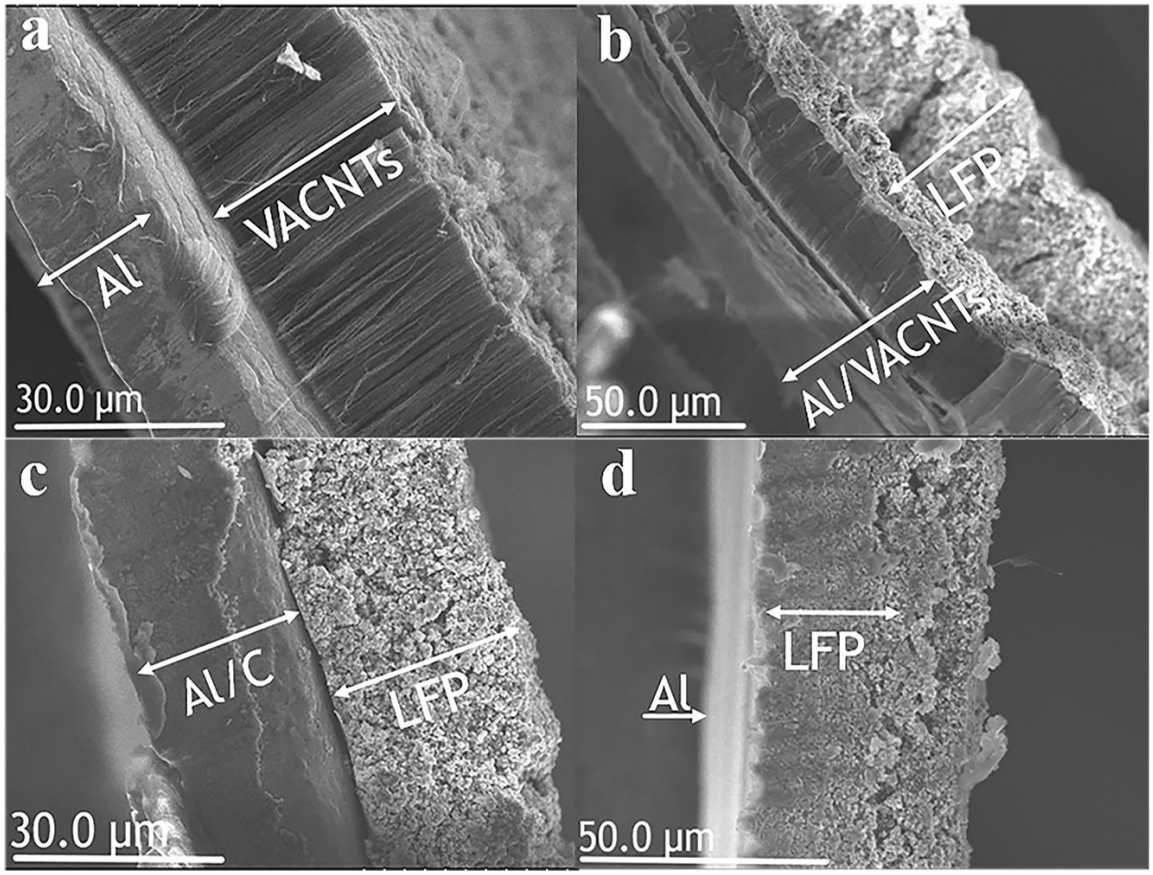


Figure 4.2. (a) Cross sectional SEM image of a VACNTs-coated Al foil, or Al/VACNTs foil. Similar images for LFP coatings on Al/VACNTs foil, commercial carbon-coated Al foil, and bare Al foil are shown in panels (b) – (d).

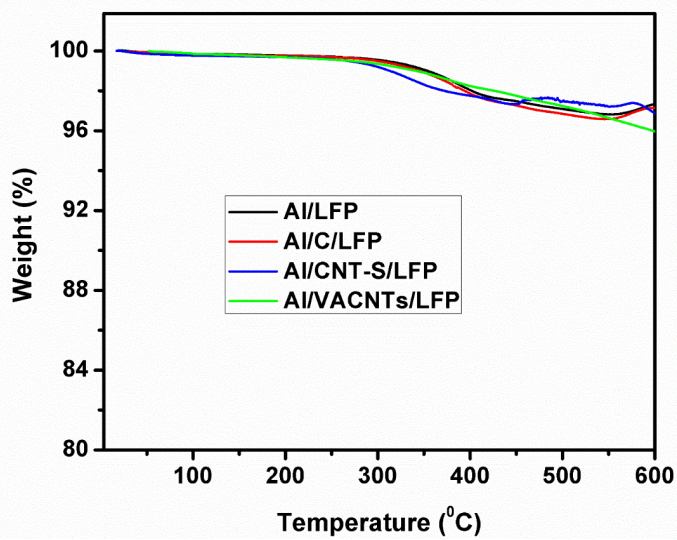


Figure 4.3. TGA of LFP electrodes described in Figure 4.2.

As mentioned in the introduction, NMP is currently used in commercial LIB manufacturing for dispersing active materials as its surface tension (41.0 mN $m^{-1}$ at 25 °C) allows good wetting of the Al foil (surface energy: 47.9 mJ $m^{-2}$). On the other hand, the high surface tension of water (72.8 mN $m^{-1}$ at 25 °C) precludes its use in preparing and coating active materials slurries.[39,42,122] NMP is disadvantageous due to its high cost and toxicity, which warrants the use of expensive solvent recovery systems and stringent protocols for materials handling and disposal.[122] The presence of VACNTs on Al provides capillary channels that improve wetting of aqueous dispersions, as evidenced from contact angle measurements shown in Figure 4.4. The aqueous dispersions exhibited a relatively smaller contact angle (~60°) on the Al/VACNTs coated foil compared to bare Al foils (~110°).

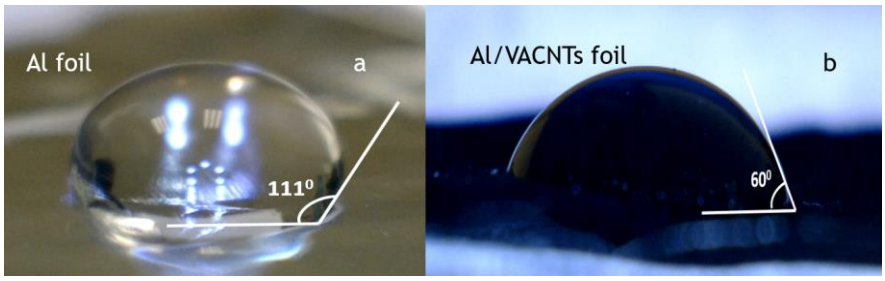


Figure 4.4. Contact angle measurements of water on (a) bare Al and (b) Al/VACNT current collectors.

Based on this observation of improved wetting, we replaced NMP with DI water and prepared aqueous slurries to coat both LFP and NMC onto the Al, Al/C, and Al/VACNTs foils depicted in Figure 4.2. We used CMC as the surfactant[123] to increase the suspension stability of LFP or NMC in water while SBR was used as an adhesive to bind the slurries with all the current collectors.

The GCD responses at two current densities (C/3 and 8C/3 rates; 1C=150 mA $g^{-1}$) for LFP electrodes (viz., Al/VACNTs/LFP, Al/C/LFP, and bare Al/LFP shown in Figure 4.2b-d) are shown in Figure 4.5. The gravimetric capacities for the bare Al/LFP and the Al/C/LFP were 90 and 109 mAh $g^{-1}$ at a low current density (50 mA $g^{-1}$, C/3 rate), respectively (Figure 4.5a). Consistent with our hypothesis, the Al/VACNTs/LFP exhibited a relatively higher gravimetric capacity of ~145 mAh $g^{-1}$ at the same current density. This implies that >60% enhancement in gravimetric capacity is possible with CCAMI engineering through VACNTs. Remarkably, as seen in Figure 4.5b, the Al/VACNTs/LFP collector showed a high areal capacity of 0.55 mAh $cm^{-2}$ at C/3, which

is twice the areal capacity of the bare Al current collector (0.26 mAh $cm^{-2}$). This enhancement in the areal capacity ~100% of Al/VACNTs/LFP electrodes (i) brings them closer to the required areal capacity of 1 mAh $cm^{-2}$ for the use of LIBs in EVs,[124] and (ii) can be readily accomplished by using Al/VACNTs current collectors instead of Al current collectors in the present day LIB manufacturing lines. At 8C/3 rate, the gravimetric (Figure 4.5c) and areal (Figure 4.5d) capacities of the Al/VACNTs/LFP exhibited a ~100% and ~150% enhancement over the corresponding capacities of the bare Al electrode, respectively. Besides investigating the dependence of the gravimetric and areal capacities at low and high current densities, we also examined their dependence on intermediate current densities and summarized them in Figure 4.6a and b, respectively.

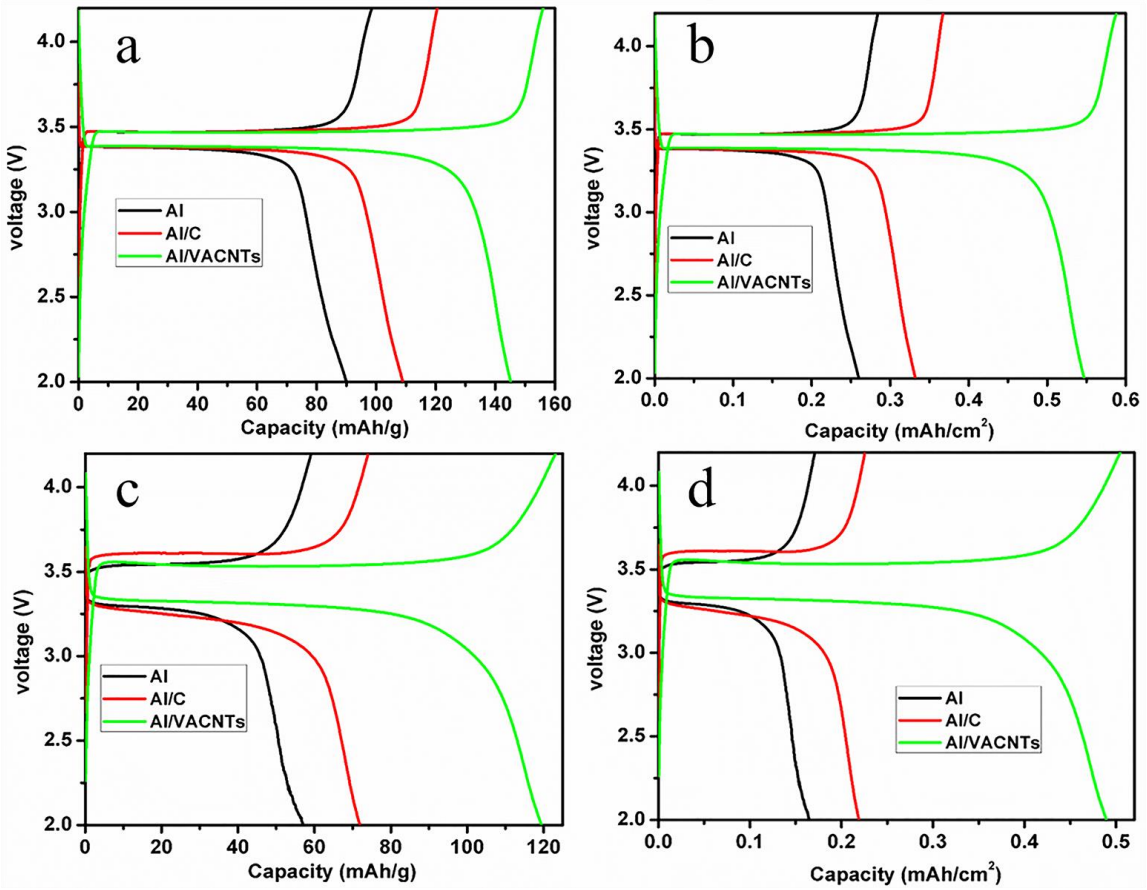


Figure 4.5. Galvanostatic charge/discharge profiles for various current collectors coated with LFP (see text for details). The gravimetric (panels a and c) and areal (panels b and d) capacities at 50 mA $g^{-1}$ (C/3 rate) and 400 mA $g^{-1}$ (8C/3 rate) current densities are shown.

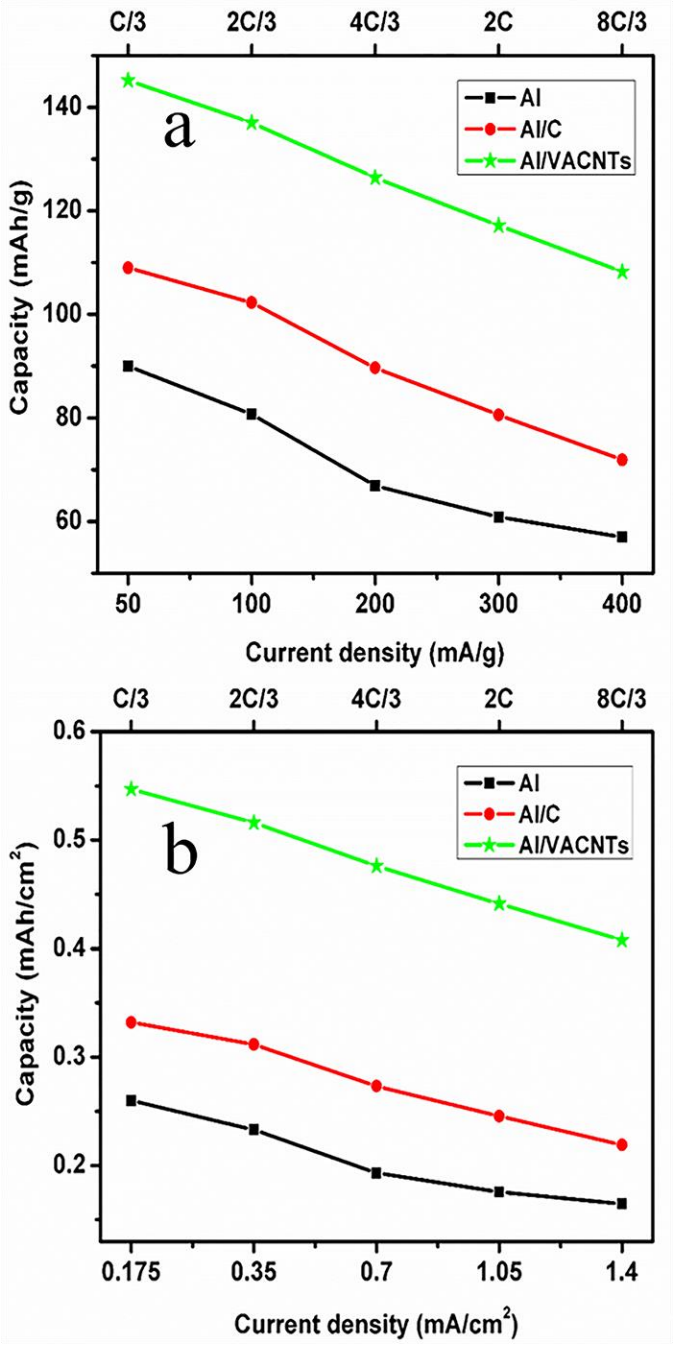


Figure 4.6. Gravimetric (a) and areal (b) capacities of various LFP electrodes described in Figure 4.2 at varying current densities (from 50–400 mA $g^{-1}$).

The electrical resistances of the active material (e.g., LFP), current collector (Al) and the CCAMI act in series (*cf.* Figure 4.1) and appear as the total internal resistance *R*. While the addition of conductive carbon (super P in our case) provides percolating networks within the active material, it does not improve the CCAMI resistance. Previously, it was demonstrated that texturing Al foil with Al nanoneedles/pillars increased the rate capability and battery performance.[125,126] The underlying mechanism in such methods is to increase the total surface area of the current collector for achieving better contact with the active material. However, such nanostructuring of the Al foil increases its oxidation rate and accelerates the formation of alumina, which could eventually result in the increase of CCAMI resistance leading to battery failure. Here, we present a new scalable process for growing VACNTs directly on Al foils to decrease CCAMI resistance and consequently achieve high rate capability (as shown later in Figure 4.8a). Traditionally, carbon coatings have also been used on Al foils to reduce the CCAMI resistance and improve the battery performance.[109] Indeed, as shown in Figure 4.2 and 4.5, commercial Al/C/LFP electrodes exhibit a moderate improvement over bare Al/LFP. Many commercially available carbon additives such as super P (added to the active material) contain a mixture of $sp^2/sp^3$ hybridized carbon.[127] Such carbon additives (super P in this case) within the active material are known to form highly resistive $sp^3$ bonds with the carbon coating on the current collector, leading to the failure of LIB cells at high rates.[127] On the other hand, VACNTs provide not only higher surface area but also enable interactions (as opposed to $sp^3$ bonds) between $sp^2$ content of the carbon additives in the active material and CNTs on the current collector to decrease the CCAMI

resistance. The changes in equivalent series and charge transfer resistances ($R_s$ and $R_{ct}$) resulting from the presence of VACNTs in Al/VACNTs/LFP electrodes were deduced from EIS measurements (Figure 4.7a). It is well known that $R_s$ is a series combination of electrolyte and CCAMI resistances.[128] The Nyquist plot for both Al/C/LFP and Al/VACNTs/LFP exhibited a classical single time-constant behavior, which was modeled using Randles circuit analysis (see the inset in Figure 4.7a).[16,129] The $R_s$ value, which is related to the real impedance value in the high-frequency region of the Nyquist plot at $Z_{imag}$ = 0 Ω, was found to be 9.3 and 29.8 Ω for Al/VACNTs/LFP and Al/C/LFP electrodes, respectively. Given that the same electrolyte (1M $LiPF_6$ in ethylene carbonate and dimethyl carbonate (w/w = 1:1)) was used for all the cells, the three-fold reduction in $R_s$ for Al/VACNTs/LFP is attributed to the presence of VACNTs that significantly reduced the CCAMI. In addition, the characteristic semicircle in the mid- to high-frequency regions, which corresponds to $R_{ct}$, is relatively lower (~30 Ω) in the case of Al/VACNTs/LFP electrodes compared to that in Al/C/LFP electrodes (~50 Ω).[16]

To further characterize our electrodes, we employed cyclic voltammetry to monitor the intercalation/de-intercalation of $Li^+$ at a scan rate of 10 mV $s^{-1}$. A reduction in the peak potentials during charge-discharge cycles was evident for the Al/VACNTs/LFP electrode, viz., its oxidation peak (~3.9 V in Figure 4.7b) is ~200 mV lower compared to that of the commercial Al/C/LFP electrode (>4.1 V). Thus, the difference between the anodic and cathodic peak voltages is lower for Al/VACNTs/LFP electrodes, which is advantageous in improving the total energy density of the cell within

the 2.0-4.2 V window.[120,130] The advantage of VACNTs is also evidenced in the variation of the mid-point voltages ($V_M$) for both charge and discharge cycles, which is the voltage of the cell when it has discharged 50% of its total energy (Figure 4.7c).

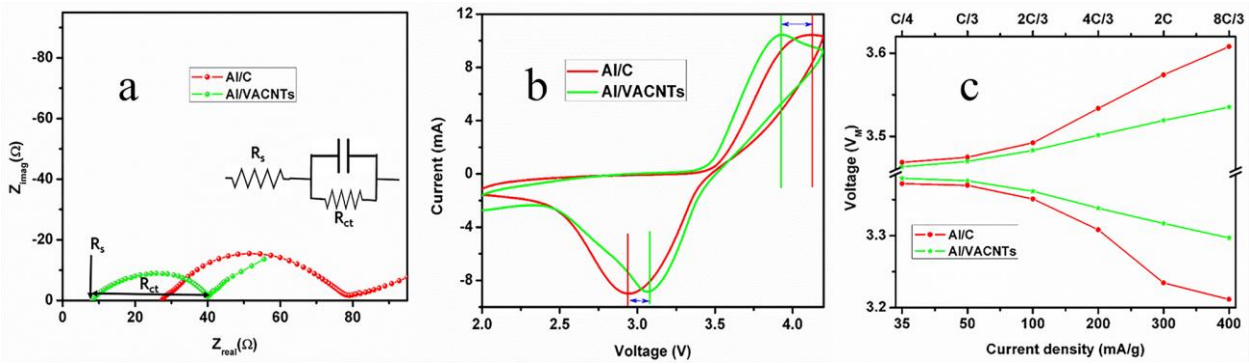


Figure 4.7. Nyquist plots (a), cyclic voltammograms (10 mV $s^{-1}$) (b), and mid-point voltages of charge/discharge (c) for LFP electrodes.

The Al/VACNTs/LFP electrodes showed the least difference (Table 4.1) in $V_M$ between charge and discharge cycles, which is attributed to lower $R$ due to VACNTs at the CCAMI (Figure 4.7c). Not surprisingly, Al/C/LFP electrodes exhibited a higher voltage drop, which is attributed to the formation of resistive $sp^3$ bonds at the interface.[127]

| Current collector | $\Delta V_M$ (mV) C/3 | $\Delta V_M$ (mV) 2C/3 | $\Delta V_M$ (mV) 4C/3 | $\Delta V_M$ (mV) 2C | $\Delta V_M$ (mV) 8C/3 |
|---|---|---|---|---|---|
| Al | 106 | 140 | 194 | 244 | 292 |
| Al/C | 105 | 141 | 226 | 340 | 396 |
| Al/VACNTs | 94 | 122 | 163 | 202 | 238 |

Table 4.1. Difference between mid-point voltage ($\Delta V_M$) of charge-discharge cycles for the LFP electrodes used in this study at varying current densities (from 50 – 400 mA $g^{-1}$).

Through our engineered CCAMI with VACNTs, we not only successfully reduced the interfacial resistance but also demonstrated the superior stability of our electrodes at higher current densities up to 4C or 600 mA $g^{-1}$ (Figure 4.8a). At this high current density (~600 mA $g^{-1}$), the cell can be charged within ~15 minutes. The gravimetric capacity of Al/VACNTs/LFP electrodes dropped from 103 to 79 mAh $g^{-1}$ after 500 cycles, which is only a 23% reduction in capacity. On the other hand, the Al/C/LFP electrodes failed to withstand this high current density, which resulted in highly scattered capacity values with an overall deterioration from 67 to ~ 0 mAh $g^{-1}$. Hence, VACNTs on Al improve the stability of the overall electrode by providing a stable contact with the active material during the GCD cycles. While some groups reported a similar high-rate performance of LFP electrodes on bare Al through hierarchical composites or LFP texturing,[119,120] it is worth noting that our process does not require any modifications to commercially used active material powders. Furthermore, the scalable manufacturing processes[131] for VACNTs-coated Al foils can be readily integrated into LIB manufacturing lines. Notably, by using Al/VACNTs/LFP electrodes, ~ 34% and 54% enhancement in energy densities were realized at power densities of ~150 W $kg^{-1}$ and 1300 W $kg^{-1}$ respectively as shown in the Ragone plot (Figure 4.8b and c). The Al/VACNTs/LFP electrode exhibited a drop of 27% in energy

density at the highest power ~1300 W $kg^{-1}$ whereas Al/C/LFP showed a 37% decrease (Figure 4.8b). Notwithstanding the 27% decrease, the energy density of Al/VACNTs/LFP electrodes at the material level is ~380 Wh $kg^{-1}$, much higher compared to the ~230 Wh $kg^{-1}$ exhibited by Al/C/LFP, at the highest power density 1300 W $kg^{-1}$.

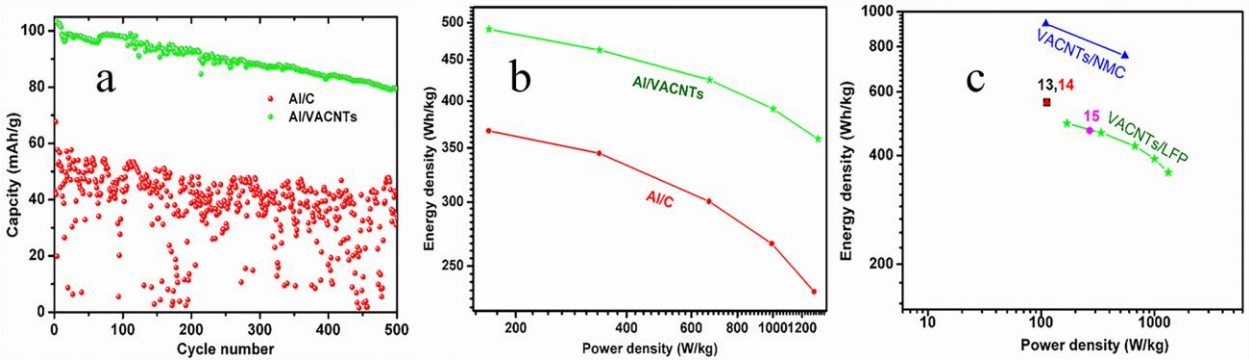


Figure 4.8. Cyclability (600 mA $g^{-1}$ – 500 cycles) (a), energy vs. power densities (b), and Ragone plots (c) of current collectors coated with LFP.

The advantages provided by CNTs were also be realized by spray coating randomly oriented CNTs on Al foils (Al/CNT-S) using a scalable approach that we had previously developed.[118] We found that Al/CNT-S/LFP electrodes also exhibited a significant enhancement (>58% gravimetric and >78% areal capacities at 400 mA $g^{-1}$) in the energy and power densities compared to the Al/LFP electrodes (Figure 4.9).

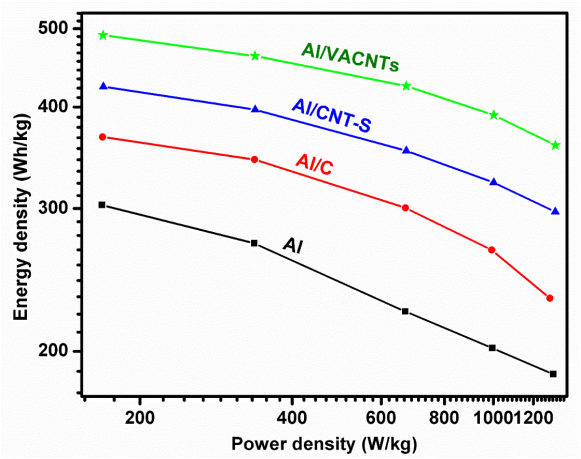


Figure 4.9. Energy vs. power density values for various current collectors coated with LFP.

The R2R spray coating method[118] has a high throughput for coating Al foils (~ 4 $cm^2$ $s^{-1}$) allowing for easy integration into LIB manufacturing lines. Lastly, to demonstrate the universal nature of CCAMI, we repeated the above measurements using NMC (with equal Ni, Mn, Co content) as the active material. The GCD profiles at 30 mA $g^{-1}$ (C/5) and 150 mA $g^{-1}$ (1C) for different NMC electrodes with and without VACNTs are shown in Figure 4.10.

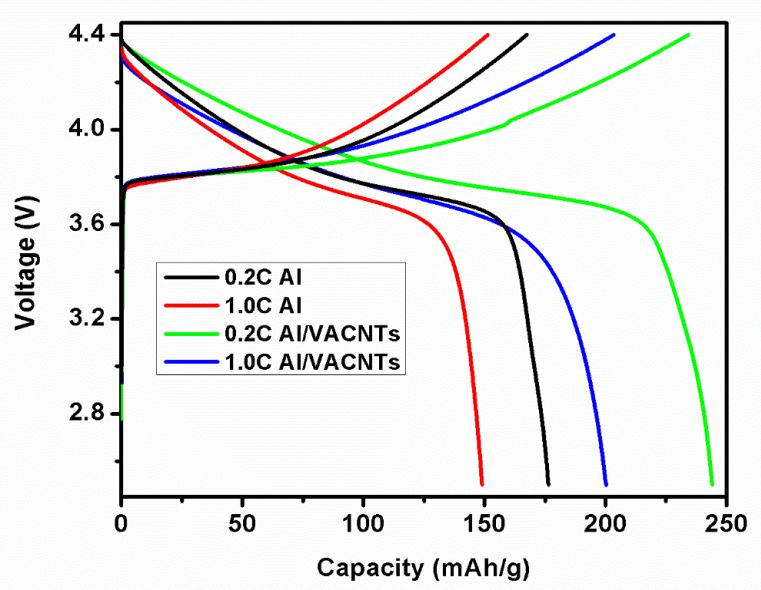


Figure 4.10. Galvanostatic charge/discharge for Al and Al/VACNTs coated with NMC.

At the material level, the Al/VACNTs current collectors coated with NMC showed a very high energy density of 760 Wh $kg^{-1}$ at a power density of 570 W $kg^{-1}$, which corresponds to a 40% increase due to the improved CCAMI in the Al/VACNTs/NMC electrode (Figure 4.8c).

## 4.4 Conclusions

We successfully engineered the CCAMI with CNTs on Al current collectors and coated them with aqueous dispersions containing active materials such as LFP and NMC for fabricating LIBs with improved performance, stability, cycle life, high capacity, and energy density. In case of LFP, a dramatic improvement in the areal (/gravimetric) capacity was observed: >100% (/>60%) at low C-rates (<2 C; 1C=150 mA $g^{-1}$), and by >150% (/>85%) at high C-rates (>2 C). The CNT engineered CCAMI resulted in

gravimetric energy densities ~500 and 360 Wh $kg^{-1}$ at power densities up to ~170 and ~1300 W $kg^{-1}$ at the material level (corresponding to ~180 and 120 Wh $kg^{-1}$ at 70 and 400 Wh $kg^{-1}$ at the battery level) with much higher power capability (increased charge capacity at high discharge rates). Notably, the CNT-modified current collectors with LFP (Al/VACNTs/LFP) withstood rates as high as 4C for 500 cycles, whereas commercial carbon coated current collectors coated with LFP (Al/C/LFP) were observed to fail at this rate. For NMC electrodes, the engineered CCAMI with VACNTs exhibited >20% (>35%) improvement in areal (/gravimetric) capacity at 0.2 C and 1C rates (1C=145 mA $g^{-1}$) leading to energy densities as high as ~760 Wh $kg^{-1}$ at ~570 W $kg^{-1}$ at the electrode level (~250 Wh $kg^{-1}$ at ~190 W $kg^{-1}$ at the battery level).

# CHAPTER FIVE

# CELLULOSE PAPER BASED CURRENT COLLECTORS

This chapter describes my work on the development of surfactant free spray coating of paper with carbon nanotubes and its use as a current collector replacing conventional aluminum foil in lithium-ion batteries, which is accepted for publication in the following article: "Carbon Nanotubes Coated Paper as Current Collectors for Secondary Li-ion Batteries" Ventrapragada, L. K., Creager, S. E., Rao, A. M. & Podila, R. *NTREV*. accepted.

## 5.1 Introduction

There has been a growing interest in displacing relatively-heavy metallic current collectors in LIBs with lightweight paper/cellulose based substrates for efficient energy storage. In addition to lightweight and flexibility, the use of paper-based cathodes for LIBs has many advantages such as the low cost of raw materials, ease of availability, biodegradability, and convenient integration into the existing manufacturing lines and safety[41,132–142] A critical roadblock, however, is that paper is electrically insulating unlike traditional metallic current collectors such as Al and Cu used in LIBs. In this regard, many researchers have endeavored to make cellulose fiber-based conducting composites, or coat papers with different conducting materials (e.g., activated carbon) using binders.[115,143–145] These processes invariably involve the use of additives, such as insulating binders (e.g., butyl rubber) and surfactants,[33,115,143–148] which result in a lower

gravimetric capacity due to the compromised electrical conductivity and increased amount of inactive material present in the electrode. Herein, we developed an additive-free roll-to-roll spray coating technique to prepare highly-conducting multi-walled carbon nanotubes (CNTs) coated paper which can be used as current collectors. Our method doesn't involve heat for drying since we used ethanol for spray coating which can be easily evaporated at room temperature, thus making paper-CNTs based current collectors more economically viable. Given that the average diameter of cellulose fibers is on the order of few tens of microns, CNTs are ideal for achieving a conformal conductive coating on these fibers. Specifically, we demonstrate that roll-to-roll spray coated paper-CNTs substrates can be used as current collectors for $LiFePO_4$ (LFP)-based LIBs. The as-prepared paper-CNTs current collectors exhibited a low sheet resistance (~240 ohm $m^{-2}$) even at a low CNT mass loading ~0.3 mg $cm^{-2}$. A full cell containing a graphite anode and a 90 wt.% LFP coated paper-CNTs cathode showed a gravimetric capacity of ~150 mAh $g^{-1}$ at 0.5C rate (75 mA $g^{-1}$) as shown in Figure 5.1. At the material level, the paper-CNTs based LIBs prepared in this study exhibited an energy density of 460 Wh $kg^{-1}$ at a power density of 250 W $kg^{-1}$. Furthermore, the LFP coated paper-CNTs cathodes exhibited a ~17% improvement in areal capacity compared to the Al-based LFP cathodes with excellent stability for ~450 cycles at 150 mA $g^{-1}$, and robust performance at high rates up to ~600 mA $g^{-1}$.

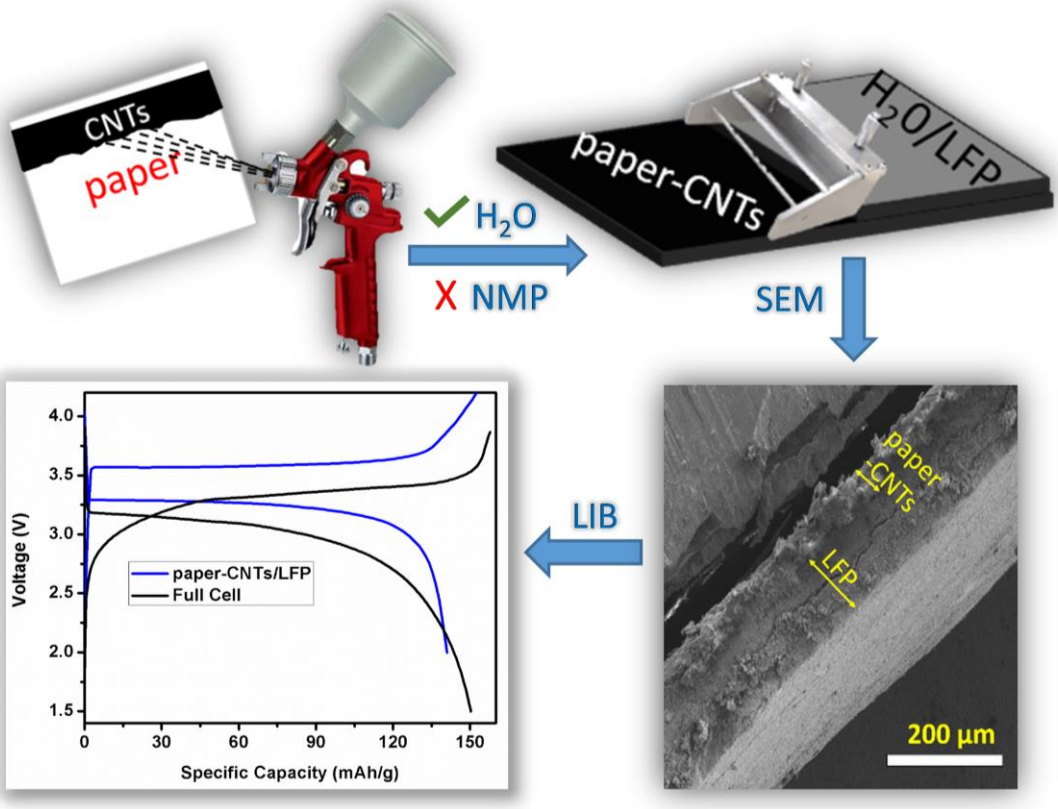


Figure 5.1. Graphical abstract depicting spray coating of CNTs on paper, LFP slurry coating on paper-CNTs, SEM image of cross-section of paper-CNTs/LFP, and a sample GCD curves at 0.5 C rate.

## 5.2 Fabrication of paper based current collectors for LIBs

5.2.1 Spray coating paper with CNTs. CNTs: The MWCNTs (diameter <8 nm, 10 - 30 µm long, >95 wt.% purity, and >500 $m^2 g^{-1}$ specific surface area) used in this study were purchased from Cheap Tubes Inc. (Catalog Number: 030101). A Branson Sonifier 250 (200 Watt, operated at 40% duty cycle) was used to sonicate the CNTs for two cycles, wherein each cycle lasted for 15 minutes with a 10-minute break between

consecutive cycles. Paper: Regular copy paper (8 ½" x 11"; 8.4 mg $cm^{-2}$) purchased from Staples was used as the substrate. Spray coating process: An entire (8 ½" x 11") sheet of paper was spray coated twice (each lasting for 5 s) using a mobile spray gun (Iwata 5095 WS400 with 1.3 mm nozzle and 29 psi ambient air pressure) that was placed at a distance of 40 cm from the paper. The spray coated paper was allowed to dry at room temperature after each coating cycle. Foils: The activated carbon coated aluminum foils were purchased from MTI Inc. (Catalog Number: EQ-CC-Al-18u-260).

5.2.2 Electrode slurry preparation. The LFP cathodes were prepared by dispersing carboxymethylcellulose (CMC) (1 wt. %, MTI Corp.), styrene-butadiene rubber (SBR) (4 wt. %, MTI Corp.), timcal graphite & carbon super P (5 wt. %, MTI Corp.), and $LiFePO_4$ (90 wt. %, MTI Corp.) in DI water (18 MΩ). CMC was first dissolved completely in water at 85 °C, and subsequently, SBR was added to this solution at room temperature. Carbon super P and LFP powders were dried, mixed and added to the above solution with continuous stirring. The resulting slurry was stirred overnight, and a doctor blade set to 100 μm was used to coat bare paper and paper-CNTs current collectors. Next, the coated papers were dried at room temperature, and subsequently, oven dried at 100 °C for 6 h in a precision compact oven. The LFP mass loadings in these coatings was ~3.4 mg $cm^{-2}$ and the porosity of the electrode was calculated to be 0.48.

5.2.3 Coin cell preparation. Cathodes (dia. ~10 mm) were stamped, weighed and soaked in an electrolyte of 1M lithium hexafluorophosphate ($LiPF_6$) in ethylene

carbonate and dimethyl carbonate (w/w = 1:1, Sigma-Aldrich) before assembling them into 2032 type coin cells with a lithium chip (15.6 dia. x 0.45 mm thick, MTI Corp.) as the counter electrode. Here we used a lithium chip which is bigger than the cathode in size and capacity, hence the anode is not the limiting electrode. These electrodes were separated by a Celgard 2325 separator (Celgard, LLC) that was presoaked in the electrolyte. The coin cells were assembled inside a glove box where oxygen and moisture contents were below 0.1 ppm. Full cells were assembled with commercial graphite coated on copper foils (MTI Corp.) as the counter electrodes.

5.2.4 Galvanostatic charge-discharge (GCD) measurements. The electrochemical characterization was carried out using an MTI multi-channel battery analyzer. LFP cells were initially conditioned by charging and discharging over a potential range of 2.0 to 4.2 V at a C/4 rate (1C = 150 mA $g^{-1}$). Subsequently, GCD studies were performed at varying current rates (0.5C to 4C) to compare their electrochemical performance. At the material level, gravimetric energy and power densities were calculated based on the weight of the active material, i.e., LFP.

5.2.5 Electrochemical Impedance Spectroscopy (EIS). After conditioning, EIS was conducted on the cells from 1 MHz to 0.1 Hz, at 0 V vs. OCV with an AC amplitude of 20 mV.

## 5.3 Results and discussion

As shown in Figure 5.2a, scanning electron microscopy (SEM, Hitachi S4800) revealed a network of micron-sized fibers with high porosity in uncoated paper. Figure 5.2b shows that the paper retained its fibrous structure and porosity even after it was spray coated with CNTs. Thermogravimetric analysis revealed a very low mass loading of CNTs (~0.3 mg $cm^{-2}$) on the paper; and at this mass loading, the paper-CNTs exhibited a sheet resistance ~240 ohm per square. As described in the methods section, LFP was deposited on paper-CNTs and uncoated paper, and assembled into a half-cell using Li metal anodes to evaluate their electrochemical performance. Representative SEM images of LFP coating on paper-CNTs (top and cross-sectional view) are shown in Figures 5.2c and d.

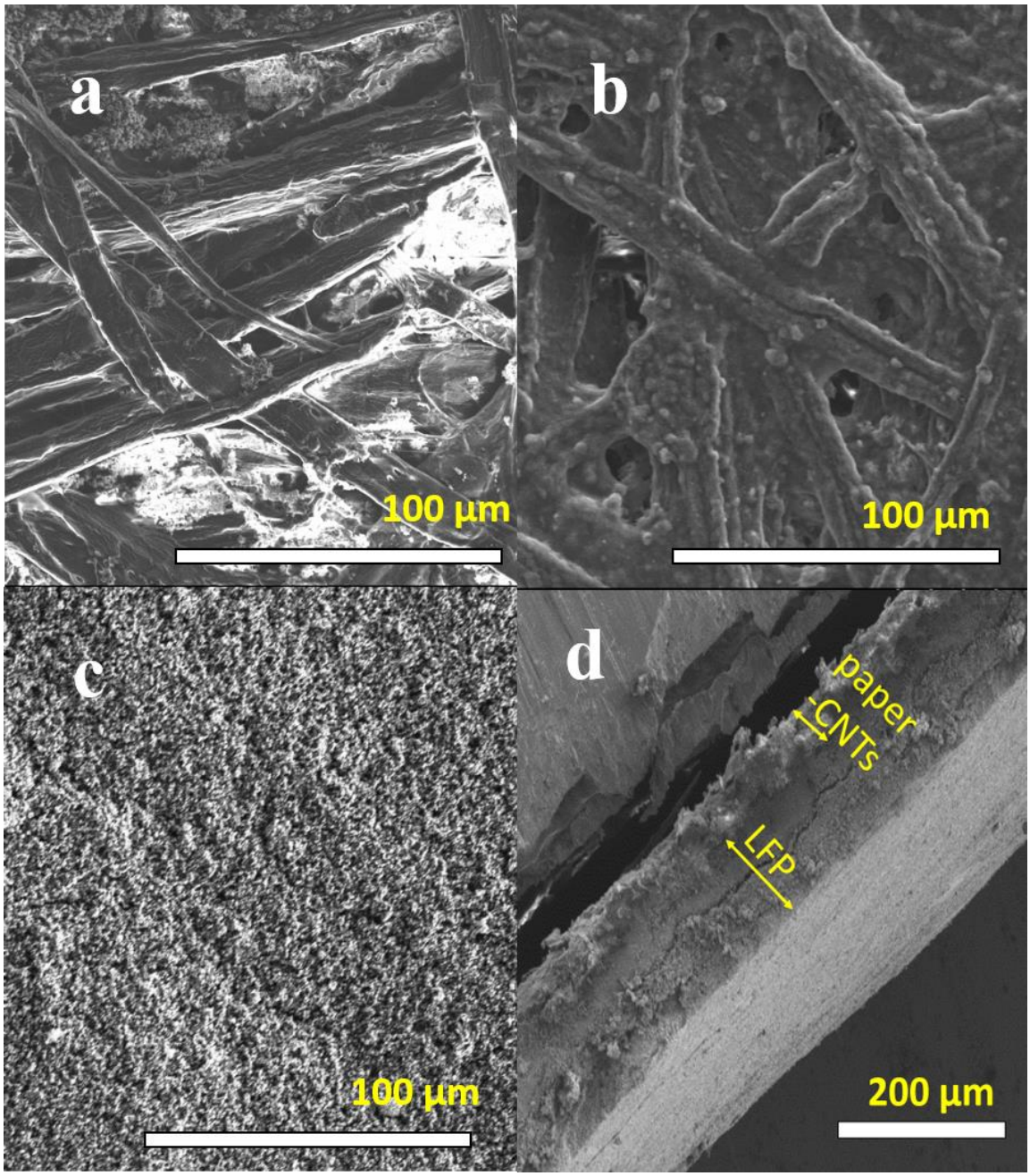


Figure 5.2. Representative scanning electron micrographs of (a) uncoated paper, (b) paper coated with carbon nanotubes (CNTs), (c) top view and (d) cross-sectional view of $LiFePO_4$ coated on paper-CNTs.

We employed cyclic voltammetry to monitor the intercalation/de-intercalation of $Li^+$ in cells assembled using uncoated paper/LFP (paper/LFP) and paper-CNTs/LFP cathodes at a scan rate of 0.1 mV $s^{-1}$ as presented in Figure 5.3a.[1] Paper-CNTs/LFP electrodes showed an oxidation peak current density of 0.179 A $g^{-1}$ at ~3.8 V and a reduction peak current density of -0.136 A $g^{-1}$ at ~3 V. On the other hand, uncoated paper/LFP has negligible peaks as evident in the inset of Figure 5.3a due to poor electrical conductivity of paper.

These cells were further characterized to elucidate the changes in charge transfer resistance values ($R_{ct}$) using electrochemical impedance spectroscopy (EIS)[16] (Figure 5.3b). The Nyquist plots for paper-CNTs/LFP, and paper/LFP exhibited a classical single time-constant behavior, which was modeled using Randles circuit analysis[129] (inset in Figure 5.3b). The characteristic semicircle in the mid- to high-frequency regions, which corresponds to $R_{ct}$, is relatively lower (~69.3 Ω) in the case of paper-CNTs/LFP electrodes compared to that in paper/LFP electrodes (~239 Ω). Given that all the cells have the same electrolyte, the three-fold reduction in $R_{ct}$ for the paper-CNTs/LFP is attributed to the presence of CNTs.

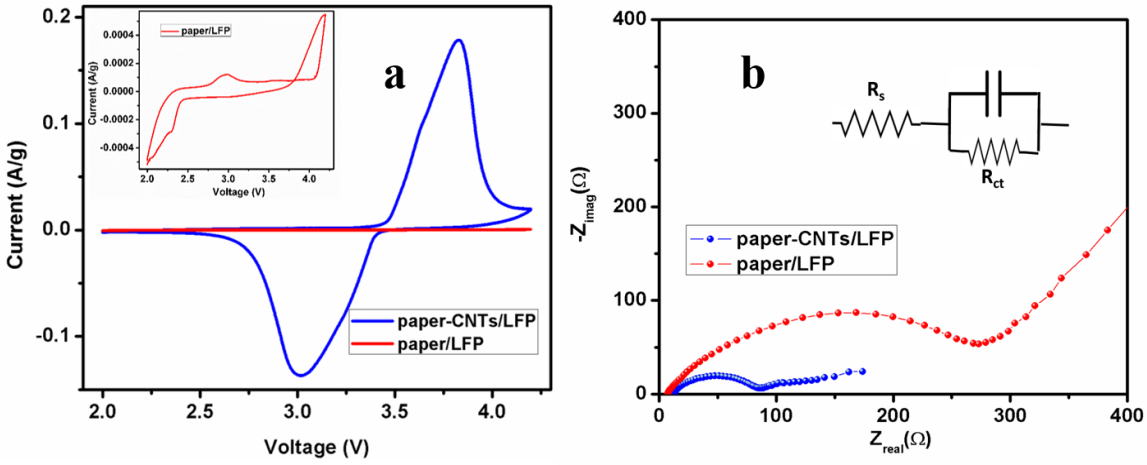


Figure 5.3. (a) Cyclic voltammograms (0.1 mV $s^{-1}$) and (b) Nyquist plots (b) for $LiFePO_4$ electrodes (with paper and paper-CNTs current collectors). The inset in Figure 5.3b shows the Randles circuit for single time-constant behavior observed in the Nyquist plot.

The GCD responses of the paper-CNTs/LFP half and full cells at 0.5C rate (75 mA $g^{-1}$) are shown in Figure 5.4a. All gravimetric capacities were determined at the material level by dividing the total capacity with the active material (i.e., LFP) weight. Gravimetric capacities (~ 140 mAh/g) reported for commercial LFP powders coated on Al foils (MTI Corp.)[127,149] have been achieved with our paper based current collectors due to the coating of CNTs. As discussed in the methods section, we assembled full cells using a graphite anode and a paper-CNTs/LFP cathode. These cells showed a gravimetric capacity value of ~150 mAh $g^{-1}$. However, a slight reduction in the discharge voltage was observed in the response of the full cell due to the presence of the graphite anode instead of the Li metal anode. The performance of paper-CNTs/LFP electrodes was further evaluated at different C-rates of 0.5 – 4C (75 – 600 mA $g^{-1}$) between 2.0 – 4.2 V and the

results are presented in Figure 5.4b. These cells showed high capacity values of ~74 mAh $g^{-1}$ even at a very high current density of 600 mA $g^{-1}$ (4C rate). The decrease in the capacity values at higher C-rate is expected as the gravimetric capacity of LIBs decreases at higher power/current densities. Nevertheless, after the 4C cycling, the paper-CNTs/LFP electrodes were cycled again at 0.5C rate and the initial capacity values were recovered showing that the loss of capacities at high C-rates are reversible (Figure 5.4b). We also fabricated cells using activated carbon coated Al (Al/C) current collectors (MTI Corp.) coated with LFP (active material mass loading ~3.4 mg $cm^{-2}$ ) to compare the performance of paper-CNTs/LFP with conventional cells.[1]

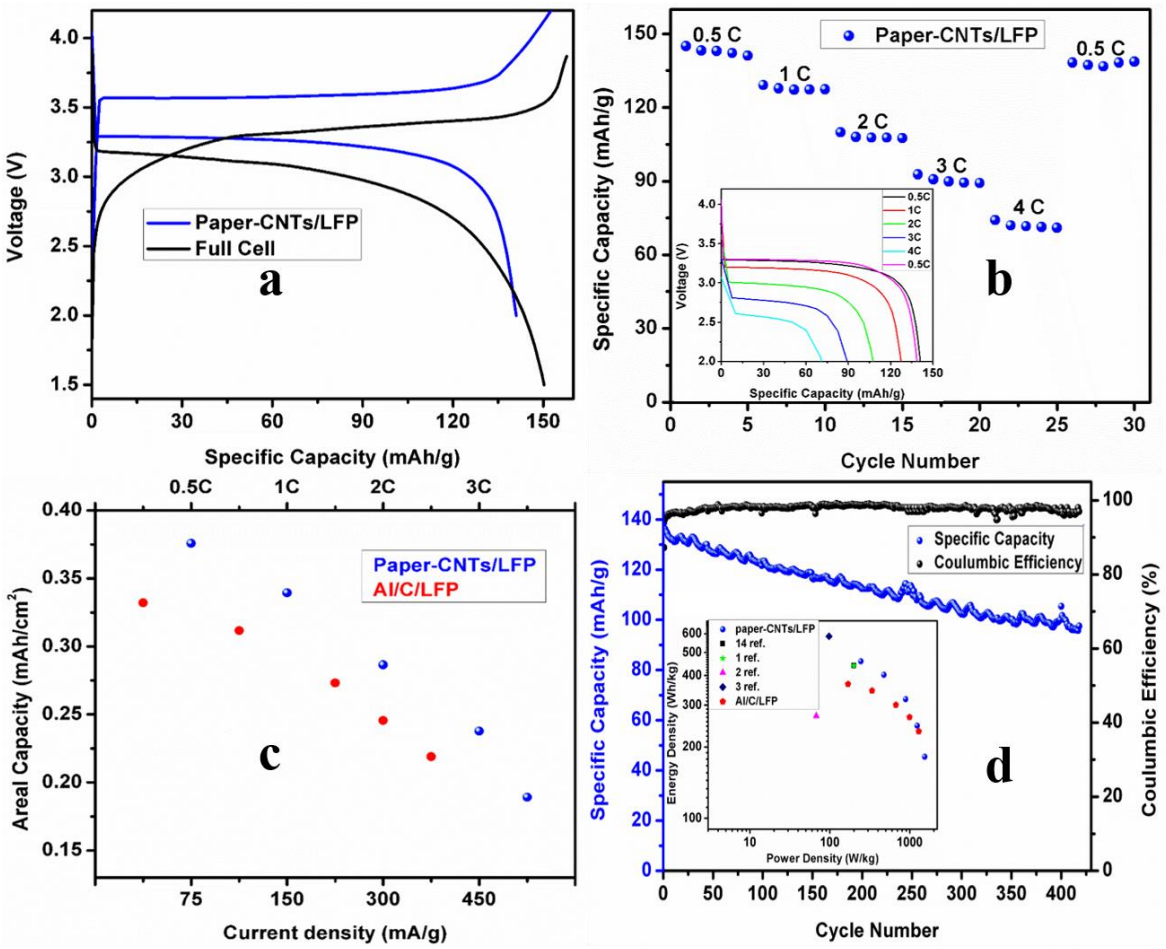


Figure 5.4. (a) Gravimetric charge-discharge curves, (b) C-rate cycling, (c) Areal capacities, and (d) Cycling performance of paper-CNTs/$LiFePO_4$ electrode. Inset in panel (c) depicts the representative galvanostatic discharge curves for the 5$^{th}$ cycle of each C-rate series. Inset in panel (d) is the Ragone plot and the numbers (at material level) in the legend in the inset of Figure 5.4d denote references for other works that used paper-based electrodes.

The areal capacity values of paper-CNTs/LFP and Al/C/LFP electrodes are comparable as seen in Figure 5.4c with the former exhibiting slightly improved values.

At the 2C rate, paper-CNTs/LFP exhibited ~17% improvement in areal capacity values compared to commercial Al/C/LFP electrodes.

Besides the development of paper-based current collectors described above, this study also focused on displacing N-Methyl-2-pyrrolidone (NMP) which is traditionally used in commercial battery manufacturing lines for dispersing and coating active materials on current collectors.[122] NMP is a toxic solvent with a high boiling point, and requires an expensive solvent recovery system in addition to posing safety and disposal challenges.[39,42] Hence, displacing NMP during the preparation of LIB cathodes is desirable. In this study, we used water-based slurry to coat active materials on paper-CNTs current collectors, which is greener, economical, and sustainable. Using a water-based slurry, it is difficult to achieve uniform coating of the active material on Al/C current collectors - cracks often develop which results in a poor overall resistance of the electrode. Unlike Al, paper has a high affinity for water, which allows it to easily wick the slurry resulting in a homogenous coating even with 90% active materials. This ability led to the improved performance presented in Figures 5.3 and 5.4. Although previous reports demonstrated the possibility of using paper-based electrodes, they achieved an active material loading of only 70 – 80% in their electrodes.[115,132,136,143,145] In our case, the paper-CNTs allowed for ~90% active material loading. As discussed in our previous work (ACS Omega 2018, 3, 4502-4508), the presence of CNTs reduces the resistance at the cathode current collector and active material interface (CCAMI) and thus provides access to the capacity of most of the active material, resulting in high energy density

values. The robustness of our paper-CNTs/LFP electrodes was tested by cycling them at 1C rate for 450 cycles (Figure 5.4d). As evident from Figure 5.4d, the paper-CNTs/LFP electrodes exhibited excellent coulombic efficiency and cycling stability. Paper-CNTs/LFP electrodes were found to have an energy density of 460 Wh $kg^{-1}$ at a power density of 250 W $kg^{-1}$, which is superior to previously reported paper-based electrodes (inset of Figure 5.4d).[115,132,135,136]

## 5.4 Conclusions

We successfully coated LIB cathode material on a CNT modified paper based current collector. We used a surfactant-free conformal coating of CNTs on the fibers of the commercially available paper as evidenced by the SEM images. We also adopted a water based slurry for coating of electroactive materials of our modified current collectors. This simple method of electrode fabrication didn't compromise on the performance of the LIBs assembled from these electrodes. Full cells made from these LFP based electrodes showed high capacity values of ~150 mAh $g^{-1}$. Paper-CNTs/LFP electrodes had excellent stability and cyclability for over 500 cycles. They exhibited a high energy density of 460 Wh $kg^{-1}$ at a power density of 250 W $kg^{-1}$ (150 Wh $kg^{-1}$ at a power density of 80 W $kg^{-1}$ at the battery level).

# CHAPTER SIX

## PERSPECTIVE

The research and development (R&D) of novel nanomaterials are expected to lead to improved electrodes for energy storage applications. While such applications may be commendable, the ensuing impact on the environment must also be carefully considered during design on novel nanomaterials.

Generation of metal nanoparticles (MNPs) with the laser ablation-based technique without the use of surfactants can be very useful in applications where the pristine nature of the composite is important. In my work, I primarily generated gold nanoparticles (AuNPs) and decorated on modified graphene. It would be interesting to explore the generation of bimetallic or composite metal nanoparticles and study the synergy between multiple metal nanoparticles, if present. For example, gold-palladium is a very good catalyst for alcohol oxidation reactions. I also developed a one-pot electrochemical synthesis of Au-Polycurcumin composite on graphite electrodes. AuNPs have excellent bio-sensing applications and polycurcumin, derived from a naturally occurring monomer can be an excellent substrate to disperse AuNPs. I strongly believe Au-Polycurcumin composite can be an excellent choice for sensing some of the biomolecules like dopamine, glucose, etc.

My work on improving the performance of a Li-ion battery through the use of carbon nanotubes (CNTs) coated current collectors has shown promise, and much room for further improvement exists. For example, I showed enhanced battery performance

using aluminum foil coated with 30 μm tall vertically aligned CNTs (VACNTs), but it will be interesting to determine whether the length of the CNTs can be tuned, or VACNTs can be doped with nitrogen/born to further improve the performance of the battery. It will be beneficial if one can achieve similar or better performance with shorter VACNTs. Also, I found that the performance of paper-CNTs/LFP electrodes is not good at high C-rate charge/discharge cycles and longer cycling, which may be due to the relatively large thickness of the paper used in my work. A thinner paper may improve the overall performance of the electrode and reduce the overall weight of the electrode.

# APPENDIX A

## Glossary of acronyms used in the dissertation

1. AEM-DEFC : anion exchange membrane direct ethanol fuel cell
2. Al/C: commercial carbon-coated Al foil
3. Al/CNT-S: spray coated CNTs on Al foil
4. Al/VACNTs: vertically aligned carbon nanotubes on Al foil
5. AM: active material
6. AR: analytical grade
7. Au-LCG: gold-laser converted graphene
8. AuNPs: gold nanoparticles
9. Au-Polycurcumin: gold-polycurcumin
10. CCAMI: current collector active material interface
11. CMC: carboxymethylcellulose
12. CNTs: carbon nanotubes
13. $C_O$: concentration of oxidant species (O)
14. CP : chronopotentiometry
15. $C_R$: concentration reductant species (R)
16. CV: cyclic voltammetry
17. DAFC: direct alcohol fuel cell
18. DEFC: direct ethanol fuel Cell
19. DMC: dimethyl carbonate

20. $E_a$: Activation Energy
21. EC: ethylene-carbonate
22. ECSA: effective catalytic surface area
23. EDX/EDAX: energy dispersive x-ray analysis
24. EIS: electrochemical impedance spectroscopy
25. EOR: ethanol oxidation reaction
26. EV/HEVs: electric and hybrid electric vehicles
27. FESEM: field emission scanning electron microscope
28. f-HEG: functionalized hydrogen exfoliated graphene
29. GCD: galvanostatic charge-discharge
30. GCE: glassy carbon electrode
31. GO: graphite oxide
32. $I$: current
33. $I_b$: anodic peak current during reverse scan
34. $I_f$: anodic peak current during forward scan
35. $I_p$: peak current density
36. LAMS: laser ablation mediated synthesis
37. LCG: laser converted graphene
38. LCO: lithium cobalt oxide ($LiCoO_2$)
39. LFP: lithium iron phosphate ($LiFePO_4$)
40. LIBs: lithium-ion batteries
41. LSV: linear sweep voltammetry

42. MNPs: metal nanoparticles
43. MWCNTs: multi-walled carbon nanotubes
44. NMC: $LiNi_{0.33}Co_{0.33}Mn_{0.33}O_2$
45. NMP: N-Methyl-2-pyrrolidone
46. ORR: oxygen reduction reaction
47. PANI: polyaniline
48. PEDOT: poly(3,4-ethylenedioxythiophene)
49. PEM-DEFC: proton exchange membrane direct ethanol fuel cell
50. PEMFC: proton exchange membrane fuel cell
51. PPy: polypyrrole
52. Pt: Platinum
53. PTP: polythiophene
54. PVDF: polyvinylidene fluoride
55. R2R: roll-to-roll
56. $R_{ct}$: charge transfer resistance,
57. $R_s$: series resistance
58. SAED: select area electron diffraction
59. SBR: styrene-butadiene rubber
60. SEI: solid-electrolyte interface
61. SEM: scanning electron microscopy
62. $T$: temperature
63. TEM: transmission electron microscope

64. VACNTs: vertically aligned carbon nanotubes

65. XRD: x-ray diffraction

References


1. Ventrapragada, L. K., Zhu, J., Creager, S. E., Rao, A. M. & Podila, R. A Versatile Carbon Nanotube-Based Scalable Approach for Improving Interfaces in Li-Ion Battery Electrodes. *ACS Omega* **3,** 4502–4508 (2018).
2. Valero Vidal, C. & Igual Muñoz, A. in *Bio-Tribocorrosion in Biomaterials and Medical Implants* 187–219 (Woodhead Publishing, 2013). doi:10.1533/9780857098603.2.187
3. Cyclic Voltammetry: The Investigation Of Electrolysis Mechanisms. Available at: https://www.ceb.cam.ac.uk/research/groups/rg-eme/teaching-notes/cyclic-voltammetry-the-investigation-of.
4. Bard, A. J. & Faulkner, L. R. *Electrochemical Methods Fundamentals and Applications*. *Beam-Solid Interactions* (Wiley; 2 edition, 2000).
5. Linear Sweep and Cyclic Voltametry: The Principles. doi:https://www.ceb.cam.ac.uk/research/groups/rg-eme/teaching-notes/linear-sweep-and-cyclic-voltametry-the-principles
6. Hoque, M. The Oxygen Reduction Reaction in Non- aqueous Electrolytes: Li-Air Battery Applications. (2013). doi:10.13140/2.1.5089.7602
7. Zhang, J. *et al.* in *Pem Fuel Cell Testing and Diagnosis* 283–335 (Elsevier, 2013). doi:10.1016/B978-0-444-53688-4.00011-5
8. Mortimer, R. J. in *Encyclopedia of Spectroscopy and Spectrometry* 2174–2181 (Elsevier, 1999). doi:10.1006/RWSP.2000.0291

9. Baur, J. E. in *Handbook of Electrochemistry* 829–848 (Elsevier, 2007). doi:10.1016/B978-044451958-0.50036-7

10. Testing Lithium Ion Batteries. Available at: https://www.gamry.com/application-notes/battery-research/testing-lithium-ion-batteries/.

11. Andre, D. *et al.* Characterization of high-power lithium-ion batteries by electrochemical impedance spectroscopy. II: Modelling. *J. Power Sources* **196,** 5356–5363 (2011).

12. Jossen, A. Fundamentals of battery dynamics. *J. Power Sources* **154,** 530–538 (2006).

13. Love, C. T., Virji, M. B. V., Rocheleau, R. E. & Swider-Lyons, K. E. State-of-health monitoring of 18650 4S packs with a single-point impedance diagnostic. *J. Power Sources* **266,** 512–519 (2014).

14. Rodrigues, S., Munichandraiah, N. & Shukla, A. K. AC impedance and state-of-charge analysis of a sealed lithium-ion rechargeable battery. *J. Solid State Electrochem.* **3,** 397–405 (1999).

15. Liao, L. *et al.* Effects of temperature on charge/discharge behaviors of LiFePO 4 cathode for Li-ion batteries. *Electrochim. Acta* **60,** 269–273 (2012).

16. Waag, W., Käbitz, S. & Sauer, D. U. Experimental investigation of the lithium-ion battery impedance characteristic at various conditions and aging states and its influence on the application. *Appl. Energy* **102,** 885–897 (2013).

17. Takeno, K., Ichimura, M., Takano, K., Yamaki, J. & Okada, S. Quick testing of batteries in lithium-ion battery packs with impedance-measuring technology. *J.*

*Power Sources* **128,** 67–75 (2004).

18. Fuel Cells. *Fuel Cell Technology Office* Available at: https://www.energy.gov/eere/fuelcells/fuel-cells.

19. Vaghari, H., Jafarizadeh-Malmiri, H., Berenjian, A. & Anarjan, N. Recent advances in application of chitosan in fuel cells. *Sustain. Chem. Process.* **1,** 16 (2013).

20. Zakaria, Z., Kamarudin, S. K. & Timmiati, S. N. Membranes for direct ethanol fuel cells: An overview. *Appl. Energy* **163,** 334–342 (2016).

21. Ekdharmasuit, P., Therdthianwong, A. & Therdthianwong, S. The role of an anode microporous layer in direct ethanol fuel cells at different ethanol concentrations. *Int. J. Hydrogen Energy* **39,** 1775–1782 (2014).

22. Baschuk, J. J. & Li, X. Carbon monoxide poisoning of proton exchange membrane fuel cells. *Int. J. Energy Res.* **25,** 695–713 (2001).

23. Fujiwara, N. *et al.* Direct ethanol fuel cells using an anion exchange membrane. *J. Power Sources* **185,** 621–626 (2008).

24. Kavanagh, R., Cao, X. M., Lin, W. F., Hardacre, C. & Hu, P. Origin of low CO2selectivity on platinum in the direct ethanol fuel cell. *Angew. Chemie - Int. Ed.* **51,** 1572–1575 (2012).

25. Suib, S. L. *New and Future Developments in Catalysis: Batteries, Hydrogen Storage and Fuel Cells*. *New and Future Developments in Catalysis: Batteries, Hydrogen Storage and Fuel Cells* (2013). doi:10.1016/C2010-0-68687-1

26. Crabtree, G. Perspective: The energy-storage revolution. *Nature* **526,** S92 (2015).

27. Exploratory Battery Materials R&D. Available at: https://www.energy.gov/eere/vehicles/exploratory-battery-materials-rd.

28. Cell Chemistries - How Batteries Work. Available at: https://www.mpoweruk.com/chemistries.htm.

29. Goodenough, J. B. & Park, K. S. The Li-ion rechargeable battery: A perspective. *J. Am. Chem. Soc.* **135,** 1167–1176 (2013).

30. Yamada, A. *et al.* Olivine-type cathodes: Achievements and problems. *J. Power Sources* **119–121,** 232–238 (2003).

31. Jugović, D. & Uskoković, D. A review of recent developments in the synthesis procedures of lithium iron phosphate powders. *J. Power Sources* **190,** 538–544 (2009).

32. Yuan, L.-X. *et al.* Development and challenges of LiFePO4 cathode material for lithium-ion batteries. *Energy Environ. Sci.* **4,** 269 (2011).

33. Wang, J., Li, L., Wong, C. L. & Madhavi, S. Flexible single-walled carbon nanotube/polycellulose papers for lithium-ion batteries. *Nanotechnology* **23,** 495401 (2012).

34. Chung, S. Y., Bloking, J. T. & Chiang, Y. M. Electronically conductive phospho-olivines as lithium storage electrodes. *Nat. Mater.* **1,** 123–128 (2002).

35. Delmas, C., Maccario, M., Croguennec, L., Le Cras, F. & Weill, F. Lithium deintercalation in LiFePO4nanoparticles via a domino-cascade model. *Nat. Mater.* **7,** 665–671 (2008).

36. Gaberscek, M., Dominko, R., Bele, M., Remskar, M. & Jamnik, J. Mass and

charge transport in hierarchically organized storage materials. Example: Porous active materials with nanocoated walls of pores. *Solid State Ionics* **177,** 3015–3022 (2006).

37. Lung-Hao Hu, B., Wu, F. Y., Lin, C. Te, Khlobystov, A. N. & Li, L. J. Graphene-modified LiFePO4cathode for lithium ion battery beyond theoretical capacity. *Nat. Commun.* **4,** 1687 (2013).

38. Doeff, M. M., Wilcox, J. D., Kostecki, R. & Lau, G. Optimization of carbon coatings on LiFePO4. *J. Power Sources* **163,** 180–184 (2006).

39. Li, J., Armstrong, B. L., Daniel, C., Kiggans, J. & Wood, D. L. Optimization of multicomponent aqueous suspensions of lithium iron phosphate (LiFePO4) nanoparticles and carbon black for lithium-ion battery cathodes. *J. Colloid Interface Sci.* **405,** 118–124 (2013).

40. Li, J., Daniel, C. & Wood, D. Materials processing for lithium-ion batteries. *Journal of Power Sources* **196,** 2452–2460 (2011).

41. Jabbour, L. *et al.* Microfibrillated cellulose-graphite nanocomposites for highly flexible paper-like Li-ion battery electrodes. *J. Mater. Chem.* **20,** 7344–7347 (2010).

42. Li, J., Rulison, C., Kiggans, J., Daniel, C. & Wood, D. L. Superior Performance of LiFePO4 Aqueous Dispersions via Corona Treatment and Surface Energy Optimization. *J. Electrochem. Soc.* **159,** A1152–A1157 (2012).

43. Hong, W. *et al.* Preparation of gold nanoparticle/graphene composites with controlled weight contents and their application in biosensors. *J. Phys. Chem. C*

**114,** 1822–1826 (2010).

44. Li, Y., Tang, L. & Li, J. Preparation and electrochemical performance for methanol oxidation of pt/graphene nanocomposites. *Electrochem. commun.* **11,** 846–849 (2009).

45. Yáñez-Sedeño, P., Pingarrón, J. M., Riu, J. & Rius, F. X. Electrochemical sensing based on carbon nanotubes. *TrAC - Trends Anal. Chem.* **29,** 939–953 (2010).

46. Xu, C., Wang, X., Zhu, J., C, J. P. C. & Asap, A. Graphene # Metal Particle Nanocomposites Graphene-Metal Particle Nanocomposites. *Society* **112,** 19841–19845 (2008).

47. Chen, D., Tang, L. & Li, J. Graphene-based materials in electrochemistry. *Chem. Soc. Rev.* **39,** 3157–3180 (2010).

48. Kaniyoor, A., Baby, T. T., Arockiadoss, T., Rajalakshmi, N. & Ramaprabhu, S. Wrinkled graphenes: A study on the effects of synthesis parameters on exfoliation-reduction of graphite oxide. *J. Phys. Chem. C* **115,** 17660–17669 (2011).

49. Ratinac, K. R., Yang, W., Gooding, J. J., Thordarson, P. & Braet, F. Graphene and related materials in electrochemical sensing. *Electroanalysis* **23,** 803–826 (2011).

50. Peter, John, H. J. T. & Cooper. A study of the nucleation and growth process in the synthesis of colloidal gold. *Discuss. Faraday Soc.* **55,** 55–75 (1951).

51. V. Kumar, L. *et al.* Electro-catalytic activity of multiwall carbon nanotube-metal (Pt or Pd) nanohybrid materials synthesized using microwave-induced reactions and their possible use in fuel cells. *Electrochim. Acta* **83,** 40–46 (2012).

52. HARUTA, M. Gold Rush in the 21st Century. *J. Vac. Soc. Japan* **51,** 719–720

(2008).

53. Bashyam, R. & Zelenay, P. A class of non-precious metal composite catalysts for fuel cells. *Nature* **443,** 63–66 (2006).

54. Pandey, R. K. & Lakshminarayanan, V. Enhanced electrocatalytic activity of pd-dispersed 3,4- polyethylenedioxythiophene film in hydrogen evolution and ethanol electro-oxidation reactions. *J. Phys. Chem. C* **114,** 8507–8514 (2010).

55. Pandey, R. K. & Lakshminarayanan, V. Electro-oxidation of formic acid, methanol, and ethanol on electrodeposited Pd-polyaniline nanofiber films in acidic and alkaline medium. *J. Phys. Chem. C* **113,** 21596–21603 (2009).

56. Nagaraju, D. H. & Lakshminarayanan, V. Electrochemically grown mesoporous gold film as high surface area material for electro-oxidation of alcohol in alkaline medium. *J. Phys. Chem. C* **113,** 14922–14926 (2009).

57. Kwon, Y., Lai, S. C. S., Rodriguez, P. & Koper, M. T. M. Electrocatalytic oxidation of alcohols on gold in alkaline media: Base or gold catalysis? *J. Am. Chem. Soc.* **133,** 6914–6917 (2011).

58. Kaniyoor, A., Baby, T. T. & Ramaprabhu, S. Graphene synthesis via hydrogen induced low temperature exfoliation of graphite oxide. *J. Mater. Chem.* **20,** 8467–8469 (2010).

59. Amendola, V. & Meneghetti, M. Laser ablation synthesis in solution and size manipulation of noble metal nanoparticles. *Phys. Chem. Chem. Phys.* **11,** 3805–3821 (2009).

60. Martins Ferreira, E. H. *et al.* Evolution of the Raman spectra from single-, few-,

and many-layer graphene with increasing disorder. *Phys. Rev. B - Condens. Matter Mater. Phys.* **82,** (2010).

61. Moussa, S., Siamaki, A. R., Gupton, B. F. & El-Shall, M. S. Pd-partially reduced graphene oxide catalysts (Pd/PRGO): Laser synthesis of pd nanoparticles supported on PRGO nanosheets for carboncarbon cross coupling reactions. *ACS Catal.* **2,** 145–154 (2012).

62. Moussa, S., Abdelsayed, V. & Samy El-Shall, M. Laser synthesis of Pt, Pd, CoO and Pd-CoO nanoparticle catalysts supported on graphene. *Chem. Phys. Lett.* **510,** 179–184 (2011).

63. Sylvestre, J. *et al.* Surface Chemistry of Gold Nanoparticles Produced by Laser Ablation in Aqueous MediaSylvestre, J. et al., 2004. Surface Chemistry of Gold Nanoparticles Produced by Laser Ablation in Aqueous Media. The Journal of Physical Chemistry B, 108(43), pp.16864–1686. *J. Phys. Chem. B* **108,** 16864–16869 (2004).

64. Borkowska, Z., Tymosiak-Zielinska, A. & Shul, G. Electrooxidation of methanol on polycrystalline and single crystal gold electrodes. *Electrochim. Acta* **49,** 1209–1220 (2004).

65. Lima, R. B. De & Varela, H. Catalytic Oxidation of Ethanol on Gold Electrode in Alkaline Medium. *Gold Bull.* **41,** 15–22 (2008).

66. Ferrigno, R., Stroock, A. D., Clark, T. D., Mayer, M. & Whitesides, G. M. Membraneless vanadium redox fuel cell using laminar flow. *J. Am. Chem. Soc.* **124,** 12930–12931 (2002).

67. Yoo, E., Okata, T., Akita, T. & Kohyama, M. Enhanced Electrocatalytic Activity of Pt Subnanoclusters on Graphene 2009. *Nano Lett.* **9,** 2255–2259 (2009).

68. O'Mullane, A. P. & Bhargava, S. K. Reduction of Au3+ ions by activated surface atoms of platinum. *Electrochem. commun.* **13,** 852–855 (2011).

69. Eustis, S. & El-Sayed, M. A. Why gold nanoparticles are more precious than pretty gold: Noble metal surface plasmon resonance and its enhancement of the radiative and nonradiative properties of nanocrystals of different shapes. *Chem. Soc. Rev.* **35,** 209–217 (2006).

70. Wen, D. *et al.* Gold Aerogels: Three-Dimensional Assembly of Nanoparticles and Their Use as Electrocatalytic Interfaces. *ACS Nano* **10,** 2559–2567 (2016).

71. Priyadarshini, E. & Pradhan, N. Gold nanoparticles as efficient sensors in colorimetric detection of toxic metal ions: A review. *Sensors Actuators, B Chem.* **238,** 888–902 (2017).

72. Dinesh, B. & Saraswathi, R. Electrochemical synthesis of nanostructured copper-curcumin complex and its electrocatalytic application towards reduction of 4-nitrophenol. *Sensors Actuators, B Chem.* **253,** 502–512 (2017).

73. Barik, A. *et al.* Evaluation of a new copper(II)-curcumin complex as superoxide dismutase mimic and its free radical reactions. *Free Radic. Biol. Med.* **39,** 811–822 (2005).

74. Pandey, R. K. & Lakshminarayanan, V. Ethanol electrocatalysis on gold and conducting polymer nanocomposites: A study of the kinetic parameters. *Appl. Catal. B Environ.* **125,** 271–281 (2012).

75. Peng, C., Jin, J. & Chen, G. Z. A comparative study on electrochemical co-deposition and capacitance of composite films of conducting polymers and carbon nanotubes. *Electrochim. Acta* **53,** 525–537 (2007).

76. Zakil, F. A., Kamarudin, S. K. & Basri, S. Modified Nafion membranes for direct alcohol fuel cells: An overview. *Renew. Sustain. Energy Rev.* **65,** 841–852 (2016).

77. Figueiredo, M. C. *et al.* Carbon-supported shape-controlled Pt nanoparticle electrocatalysts for direct alcohol fuel cells. *Electrochem. commun.* **55,** 47–50 (2015).

78. Rodriguez, P., Kwon, Y. & Koper, M. T. M. The promoting effect of adsorbed carbon monoxide on the oxidation of alcohols on a gold catalyst. *Nat. Chem.* **4,** 177–182 (2012).

79. Reddy, K. R. *et al.* Conducting polymer functionalized multi-walled carbon nanotubes with noble metal nanoparticles: Synthesis, morphological characteristics and electrical properties. *Synth. Met.* **159,** 595–603 (2009).

80. Berzina, T., Pucci, A., Ruggeri, G., Erokhin, V. & Fontana, M. P. Gold nanoparticles-polyaniline composite material: Synthesis, structure and electrical properties. *Synth. Met.* **161,** 1408–1413 (2011).

81. Sih, B. C. & Wolf, M. O. Metal nanoparticle - Conjugated polymer nanocomposites. *Chem. Commun.* 3375–3384 (2005). doi:10.1039/b501448d

82. Bogdanović, U. *et al.* Interfacial Synthesis of Gold-Polyaniline Nanocomposite and Its Electrocatalytic Application. *ACS Appl. Mater. Interfaces* **7,** 28393–28403 (2015).

83. Reetz, M. T. *et al.* Visualization of Surfactants on Nanostructured Palladium Clusters by a Combination of STM and High-Resolution TEM. *Science (80-. ).* **267,** 367 LP-369 (1995).

84. Reetz, M. T. & Helbig, W. Size-Selective Synthesis of Nanostructured Transition Metal Clusters. *J. Am. Chem. Soc.* **116,** 7401–7402 (1994).

85. Yue, G. G. L. *et al.* Combined therapy using bevacizumab and turmeric ethanolic extract (with absorbable curcumin) exhibited beneficial efficacy in colon cancer mice. *Pharmacol. Res.* **111,** 43–57 (2016).

86. Elahi, M. Y., Mousavi, M. F. & Ghasemi, S. Nano-structured Ni(II)-curcumin modified glassy carbon electrode for electrocatalytic oxidation of fructose. *Electrochim. Acta* **54,** 490–498 (2008).

87. Ciszewski, A., Milczarek, G., Lewandowska, B. & Krutowski, K. Managing anticoagulation for valve prosthesis during pregnancy. *ACC Curr. J. Rev.* **4,** 48–49 (1995).

88. Mobin, S. M., Sanghavi, B. J., Srivastava, A. K., Mathur, P. & Lahiri, G. K. Biomimetic Sensor for Certain Phenols Employing a Copper ( II ) Complex. *Anal. Chem.* **82,** 5983–5992 (2010).

89. Trasatti, S. & Petrii, O. A. Real Surface Area Measurements. *Pure Appl. Chem.* **63,** 711–734 (1991).

90. Sukeri, A., Saravia, L. P. H. & Bertotti, M. A facile electrochemical approach to fabricate a nanoporous gold film electrode and its electrocatalytic activity towards dissolved oxygen reduction. *Phys. Chem. Chem. Phys.* **17,** 28510–28514 (2015).

91. Brummer, S. B. & Makrides, A. C. Surface Oxidation of Gold Electrodes. *J. Electrochem. Soc.* **111,** 1122–1128 (1964).

92. Tan, Y. H. *et al.* Surface area and pore size characteristics of nanoporous gold subjected to thermal, mechanical, or surface modification studied using gas adsorption isotherms, cyclic voltammetry, thermogravimetric analysis, and scanning electron microscopy. *J. Mater. Chem.* **22,** 6733–6745 (2012).

93. Ghosh, S. *et al.* Facile synthesis of Pd nanostructures in hexagonal mesophases as a promising electrocatalyst for ethanol oxidation. *J. Mater. Chem. A* **3,** 9517–9527 (2015).

94. Ksar, F. *et al.* Palladium nanowires synthesized in hexagonal mesophases: Application in ethanol electrooxidation. *Chem. Mater.* **21,** 1612–1617 (2009).

95. V. Kumar, L. *et al.* Electro-catalytic activity of multiwall carbon nanotube-metal (Pt or Pd) nanohybrid materials synthesized using microwave-induced reactions and their possible use in fuel cells. *Electrochim. Acta* **83,** 40–46 (2012).

96. Methanol, E. *et al.* Electrocatalytic Methanol Oxidation of Pt 0.5 Ru 0.5 -. 6337–6345 (2008).

97. Omar, N. *et al.* Rechargeable energy storage systems for plug-in hybrid electric vehicles-assessment of electrical characteristics. *Energies* **5,** 2952–2988 (2012).

98. Dimesso, L. *et al.* Developments in nanostructured LiMPO4 (M = Fe, Co, Ni, Mn) composites based on three dimensional carbon architecture. *Chem. Soc. Rev.* **41,** 5068–5080 (2012).

99. Croguennec, L. & Palacin, M. R. Recent achievements on inorganic electrode

materials for lithium-ion batteries. *J. Am. Chem. Soc.* **137,** 3140–3156 (2015).

100. Zhang, W.-J. Structure and performance of LiFePO4 cathode materials: A review. *J. Power Sources* **196,** 2962–2970 (2011).

101. Yuan, L. *et al.* Development and challenges of LiFePO4 cathode material for lithium-ion batteries. *Energy Environ. Sci.* **4,** 269 (2011).

102. Chung, D., Elgqvist, E. & Santhanagopalan, S. *Automotive Lithium-ion Cell Manufacturing: Regional Cost Structures and Supply Chain Considerations*. (2016).

103. Cao, W. J. *et al.* The effect of lithium loadings on anode to the voltage drop during charge and discharge of Li-ion capacitors. *J. Power Sources* **280,** 600–605 (2015).

104. Huang, J. Q., Zhai, P. Y., Peng, H. J., Zhu, W. C. & Zhang, Q. Metal/nanocarbon layer current collectors enhanced energy efficiency in lithium-sulfur batteries. *Sci. Bull.* **62,** 1267–1274 (2017).

105. Liu, T. *et al.* Formation of mono/bi-layer iron phosphate and nucleation of LiFePO4 nano-crystals from amorphous 2D sheets in charge/discharge process for cathode in high-performance Li-ion batteries. *Nano Energy* **18,** 187–195 (2015).

106. Lu, J. *et al.* The role of nanotechnology in the development of battery materials for electric vehicles. *Nat. Nanotechnol.* **11,** 1031–1038 (2016).

107. Jiang, J. *et al.* Effect of Graphene Modified Cu Current Collector on the Performance of Li4Ti5O12 Anode for Lithium-Ion Batteries. *ACS Appl. Mater. Interfaces* **8,** 30926–30932 (2016).

108. Wang, M. *et al.* Graphene-Armored Aluminum Foil with Enhanced Anticorrosion

Performance as Current Collectors for Lithium-Ion Battery. *Adv. Mater.* **29,** 1–7 (2017).

109. Wu, H. C., Wu, H. C., Lee, E. & Wu, N. L. High-temperature carbon-coated aluminum current collector for enhanced power performance of LiFePO4 electrode of Li-ion batteries. *Electrochem. commun.* **12,** 488–491 (2010).

110. Kang, S. W. *et al.* Improve the Overall Performances of Lithium Ion Batteries by a Facile Method of Modifying the Surface of Cu Current Collector with Carbon. *Electrochim. Acta* **176,** 604–609 (2015).

111. Nakanishi, S., Suzuki, T., Cui, Q., Akikusa, J. & Nakamura, K. Effect of surface treatment for aluminum foils on discharge properties of lithium-ion battery. *Trans. Nonferrous Met. Soc. China (English Ed.* **24,** 2314–2319 (2014).

112. Li, T. Carbon-coated Aluminum Foil as Current Collector for Improving the Performance of Lithium Sulfur Batteries. *Int. J. Electrochem. Sci.* **12,** 3099–3108 (2017).

113. Wu, H. C., Lee, E., Wu, N. L. & Jow, T. R. Effects of current collectors on power performance of Li 4Ti 5O 12 anode for Li-ion battery. *J. Power Sources* **197,** 301–304 (2012).

114. Wang, K. *et al.* Super-aligned carbon nanotube films as current collectors for lightweight and flexible lithium ion batteries. *Adv. Funct. Mater.* **23,** 846–853 (2013).

115. Hu, L. *et al.* Highly conductive paper for energy-storage devices. *Proc. Natl. Acad. Sci.* **106,** 21490–21494 (2009).

116. Lakshman Kumar, V. *et al.* Gold decorated graphene by laser ablation for efficient electrocatalytic oxidation of methanol and ethanol. *Electroanalysis* **26,** 1850–1857 (2014).

117. Arcila-Velez, M. R. *et al.* Roll-to-roll synthesis of vertically aligned carbon nanotube electrodes for electrical double layer capacitors. *Nano Energy* **8,** 9–16 (2014).

118. Karakaya, M. *et al.* Roll-to-roll production of spray coated N-doped carbon nanotube electrodes for supercapacitors. *Appl. Phys. Lett.* **105,** (2014).

119. Wang, B., Al Abdulla, W., Wang, D. & Zhao, X. S. A three-dimensional porous LiFePO4 cathode material modified with a nitrogen-doped graphene aerogel for high-power lithium ion batteries. *Energy Environ. Sci.* **8,** 869–875 (2015).

120. Zhang, K. *et al.* Conformal Coating Strategy Comprising N-doped Carbon and Conventional Graphene for Achieving Ultrahigh Power and Cyclability of LiFePO4. *Nano Lett.* **15,** 6756–6763 (2015).

121. Myung, S.-T. *et al.* Nickel-rich Layered Cathode Materials for Automotive Lithium-ion Batteries: Achievements and Perspectives. *ACS Energy Lett.* acsenergylett.6b00594 (2016). doi:10.1021/acsenergylett.6b00594

122. Li, J., Armstrong, B. L., Kiggans, J., Daniel, C. & Wood, D. L. Lithium Ion Cell Performance Enhancement Using Aqueous LiFePO4 Cathode Dispersions and Polyethyleneimine Dispersant. *J. Electrochem. Soc.* **160,** A201–A206 (2012).

123. Lee, J.-H., Paik, U., Hackley, V. a. & Choi, Y.-M. Effect of Carboxymethyl Cellulose on Aqueous Processing of Natural Graphite Negative Electrodes and

their Electrochemical Performance for Lithium Batteries. *J. Electrochem. Soc.* **152,** A1763 (2005).

124. Park, O. K. *et al.* Who will drive electric vehicles, olivine or spinel? *Energy Environ. Sci.* **4,** 1621 (2011).

125. Perre, E. *et al.* Direct electrodeposition of aluminium nano-rods. *Electrochem. commun.* **10,** 1467–1470 (2008).

126. Lecoeur, C., Tarascon, J.-M. & Guery, C. Al Current Collectors for Li-Ion Batteries Made via an Oxidation Process in Ionic Liquids. *Electrochem. Solid-State Lett.* **14,** A6 (2011).

127. Swain, P., Viji, M., Mocherla, P. S. V. & Sudakar, C. Carbon coating on the current collector and LiFePO4 nanoparticles – Influence of sp2 and sp3-like disordered carbon on the electrochemical properties. *J. Power Sources* **293,** 613–625 (2015).

128. Wu, Y., Keil, P., Schuster, S. F. & Jossen, A. Impact of Temperature and Discharge Rate on the Aging of a. *J. Electrochem. Soc.* **164,** 1438–1445 (2017).

129. Gomez, J., Nelson, R., Kalu, E. E., Weatherspoon, M. H. & Zheng, J. P. Equivalent circuit model parameters of a high-power Li-ion battery: Thermal and state of charge effects. *J. Power Sources* **196,** 4826–4831 (2011).

130. Liu, M. . *et al.* Mild solution synthesis of graphene loaded with LiFePO4-C nanoplatelets for high performance lithium ion batteries. *New J. Chem.* **39,** 1094–1100 (2015).

131. Arcila-Velez, M. R. *et al.* Roll-to-roll synthesis of vertically aligned carbon

nanotube electrodes for electrical double layer capacitors. *Nano Energy* **8,** 9–16 (2014).

132. Hu, L. & Cui, Y. Energy and environmental nanotechnology in conductive paper and textiles. *Energy Environ. Sci.* **5,** 6423 (2012).

133. Wang, J. *et al.* Rod-coating: Towards large-area fabrication of uniform reduced graphene oxide films for flexible touch screens. *Adv. Mater.* **24,** 2874–2878 (2012).

134. Song, K., Ganguly, I., Eastin, I. & Dichiara, A. B. Lignin-modified carbon nanotube/graphene hybrid coating as efficient flame retardant. *Int. J. Mol. Sci.* **18,** (2017).

135. Hu, L., Wu, H., La Mantia, F., Yang, Y. & Cui, Y. Thin, flexible secondary Li-ion paper batteries. *ACS Nano* **4,** 5843–5848 (2010).

136. Cheng, Q. *et al.* Folding paper-based lithium-ion batteries for higher areal energy densities. *Nano Lett.* **13,** 4969–4974 (2013).

137. Pushparaj, V. L. *et al.* Flexible energy storage devices based on nanocomposite paper. *Proc. Natl. Acad. Sci. U. S. A.* **104,** 13574–7 (2007).

138. Scrosati, B. Paper powers battery breakthrough Nanosynthesis by candlelight. *Nat. Nanotechnol.* **2,** 598–599 (2007).

139. Nyholm, L., Nyström, G., Mihranyan, A. & Strømme, M. Toward flexible polymer and paper-based energy storage devices. *Adv. Mater.* **23,** 3751–3769 (2011).

140. Zhou, G., Li, F. & Cheng, H. M. Progress in flexible lithium batteries and future prospects. *Energy Environ. Sci.* **7,** 1307–1338 (2014).

141. Sun, X. *et al.* Carbon Nanotube Paper as Anode for Flexible Lithium-Ion Battery. *Nano* **11,** 1650120 (2016).

142. Du, X., Zhang, Z., Liu, W. & Deng, Y. Nanocellulose-based conductive materials and their emerging applications in energy devices - A review. *Nano Energy* **35,** 299–320 (2017).

143. Leijonmarck, S., Cornell, A., Lindbergh, G. & Wågberg, L. Flexible nano-paper-based positive electrodes for Li-ion batteries-Preparation process and properties. *Nano Energy* **2,** 794–800 (2013).

144. Wang, C., Li, D., Too, C. O. & Wallace, G. G. Electrochemical properties of graphene paper electrodes used in lithium batteries. *Chem. Mater.* **21,** 2604–2606 (2009).

145. Lu, H., Behm, M., Leijonmarck, S., Lindbergh, G. & Cornell, A. Flexible Paper Electrodes for Li-Ion Batteries Using Low Amount of TEMPO-Oxidized Cellulose Nanofibrils as Binder. *ACS Appl. Mater. Interfaces* **8,** 18097–18106 (2016).

146. Kang, Y. R., Li, Y. L., Hou, F., Wen, Y. Y. & Su, D. Fabrication of electric papers of graphene nanosheet shelled cellulose fibres by dispersion and infiltration as flexible electrodes for energy storage. *Nanoscale* **4,** 3248–3253 (2012).

147. Pang, Z. *et al.* Fabrication and application of carbon nanotubes/cellulose composite paper. *Vacuum* **122,** 135–142 (2015).

148. Sharifi, F., Ghobadian, S., Cavalcanti, F. R. & Hashemi, N. Paper-based devices for energy applications. *Renew. Sustain. Energy Rev.* **52,** 1453–1472 (2015).

149. Kaur, A. P., Elliott, C. F., Ergun, S. & Odom, S. A. Overcharge Performance of

3,7-Bis(trifluoromethyl)- *N* -ethylphenothiazine at High Concentration in Lithium-Ion Batteries. *J. Electrochem. Soc.* **163,** A1–A7 (2016).